NANOMATERIALS

# Stabilizing in-transition phases of superlattices through shape control of silver nanocrystals

Yasutaka Nagaoka[1], Timothy C. Moore[2], Arseniy Epishin[3], Zhenyang Liu[1], Tong Cai[1], Na Jin[1], Ken Seungmin Hong[1], Peter Saghy[1], Ankai Wang[4], Yuzi Liu[5], Sooyeon Hwang[6], Yusong Bai[1], Shengli Zou[4], Ruipeng Li[7], Stephanie Reich[3], Sharon C. Glotzer[2,8]*, Ou Chen[1]*

In nanoscale assemblies, observations of structures in the transition pathways between high-symmetry lattices are rare because of the inherent instability of the intermediate phases. We report that silver nanocrystals with shapes similar to truncated octahedra (mecons) self-assemble into superlattices that are stable and resemble a previously unobserved phase that bridges face-centered and body-centered cubic structures along the Nishiyama-Wassermann martensitic pathway. These superlattices exhibited high structural purity and stability and created a robust and tunable dissymmetric phase landscape. Notably, light-matter coupling emerged in these silver nanocrystal superlattices through plasmon-photon hybridization at the quantum level.

Exploring newly identified phases of matter offers profound opportunities to transform how materials function and organize, opening pathways to a wide spectrum of technological applications (*1*–*8*). Among these, intermediate states during solid-phase transitions offer a rich library of structures that bridge well-defined phases (*8*–*13*). Although the initial and final states of such transitions are often well characterized and thermodynamically stable (*14*–*17*), the intermediate phases corresponding to configurations that arise during the transformation remain largely unexplored (*18*). These transient states, however, are of critical importance: They govern the kinetics, pathways, and energy landscapes of phase transformations and may host emergent structural or functional motifs absent from either parent phase (*6*, *19*–*26*).

In nanoscale assemblies, rare observations of in-transition structures have only been made along the Bain transformation pathway through martensitic transformation—a diffusionless phase transition between high-symmetry structures (*11*, *27*–*29*)—using advanced in situ time-resolved characterization techniques (*9*, *10*, *30*). However, despite their critical role, no such in-transition phase has ever been stabilized as a persistent structure under ambient conditions. Their inherently dynamic and short-lived nature presents major challenges for structural and property characterization, thereby limiting our ability to fully unravel the functionality and complexity of solid-state phase behavior (*14*–*18*). Unlocking access to these hidden intermediate states would mark a paradigm shift in the study of phase transitions, offering transformative opportunities to manipulate transformation pathways and to discover entirely new classes of materials with tailored functionalities (*31*–*36*).

[1]Department of Chemistry, Brown University, Providence, RI, USA. [2]Department of Chemical Engineering, University of Michigan, Ann Arbor, MI, USA. [3]Department of Physics, Freie Universität Berlin, Berlin, Germany. [4]Department of Chemistry, University of Central Florida, Orlando, FL, USA. [5]Center for Nanoscale Materials, Argonne National Laboratory, Lemont, IL, USA. [6]Center for Functional Nanomaterials, Brookhaven National Laboratory, Upton, NY, USA. [7]National Synchrotron Light Source II, Brookhaven National Laboratory, Upton, NY, USA. [8]Biointerfaces Institute, University of Michigan, Ann Arbor, MI, USA. *Corresponding author. Email: sglotzer@umich.edu (S.C.G.); ouchen@brown.edu (O.C.)

We report the formation of stable silver nanocrystal (Ag-NC) superlattices (SLs) that resemble the in-transition phase of martensitic transformation under ambient conditions that was achieved through the controlled assembly of shape-engineered Ag-NCs. By fine tuning the Ag-NC shape from a sphere to a mecon (also known as a truncated octahedron) (*37*), we observed a gradual SL evolution from a face-centered cubic (FCC) to a body-centered cubic (BCC) lattice. The Ag-NCs with intermediate shapes form stable dissymmetric SLs that resemble transient in-transition structures along the Nishiyama-Wassermann (N-W) martensitic transformation pathway (*27*). Computer simulations reveal the critical role of both particle shape and soft ligands in stabilizing these dissymmetric SL structures. Furthermore, all the SL films obtained from 10-nm-ish Ag-NCs (FCC, dissymmetric, and BCC SLs) exhibit quantum-level plasmon-photon hybridization within the deep-strong light-matter coupling regime, that is, coupling strength exceeding unity. This discovery provides a window into phase transformation mechanisms and introduces a versatile platform for designing materials with programmable structural complexity and functionality.

## Spherical and mecon Ag-NC SLs

Uniform spherical and mecon-shaped Ag-NCs, with nearly identical inorganic core volumes (~520 $nm^3$, equivalent to a 10.0-nm-diameter sphere), were synthesized through a newly developed thermal decomposition method (Fig. 1, A to F; methods; fig. S1; and tables S1 and S2). These NCs were functionalized with oleic acid and oleylamine molecules, endowing them with colloidal dispersibility in nonpolar solvents such as hexanes. High-crystalline Ag-FCC atomic domains of the obtained Ag-NCs were confirmed by high-resolution transmission electron microscopy (HRTEM) images, corresponding fast-Fourier transform (FFT) patterns, and powder x-ray diffraction measurements (Fig. 1, B and E; fig. S2; and table S3). While spherical Ag-NCs did not exhibit clearly defined facets (Fig. 1G), mecon Ag-NCs had six $\{100\}_{Ag\text{-}FCC}$ square and eight $\{111\}_{Ag\text{-}FCC}$ hexagon exposed facets (Fig. 1I and supplementary text 1). In addition, spherical Ag-NCs exhibited an absorption peak located at 3.05 eV (406 nm) (Fig. 1C), whereas mecon Ag-NCs had a main absorption feature at 2.91 eV (426 nm), along with a shoulder peak at ~3.43 eV (~362 nm) (Fig. 1F). These absorption features arose from localized surface plasmon resonances, which are collective excitations of the free electrons in the Ag-NCs (*38*, *39*).

Hexane suspensions of these Ag-NCs (at a concentration of ~10 mg/ml) were used for SL formation through a slow solvent evaporation process (methods). Synchrotron-based small-angle x-ray scattering (SAXS) measurements revealed that the spherical Ag-NCs were assembled into an FCC structure ($a_{SL\text{-}FCC}$ = 17.75 nm), whereas the mecon Ag-NCs formed a BCC SL ($a_{SL\text{-}BCC}$ = 14.12 nm), resembling the three-dimensional honeycomb structure (Fig. 1, H, J, K, and L; figs. S3 and S4; and tables S4 and S5). TEM images of the obtained FCC and BCC SLs were consistent with the assigned structures viewed from the $[111]_{SL\text{-}FCC}$ and $[110]_{SL\text{-}BCC}$ projections, respectively (Fig. 1, K and L, middle insets). Selected-area wide-angle electron diffraction (WAED) measurements confirmed the atomic orientation alignments across all constituent Ag-NCs in the SLs (Fig. 1, K and L, right insets, and fig. S5). In the FCC SLs, a sixfold symmetric WAED pattern was observed when viewed along the $[111]_{SL\text{-}FCC}$ projection (Fig. 1K, right and middle insets, and fig. S5).

Detailed analysis based on simulated WAED patterns suggested that the spherical Ag-NC orientations were aligned such that the $[110]_{Ag\text{-}FCC}$ projections appear in the $(111)_{SL\text{-}FCC}$ plane, with three distinct in-plane rotational orders exhibiting a regulated angle offset of 120° (Fig. 1H and fig. S5). In contrast, a single crystal–like spotted WAED pattern, identical to the $[110]_{Ag\text{-}FCC}$ diffraction pattern of Ag-NCs, was obtained for the BCC SLs when viewed along the $[110]_{SL\text{-}BCC}$ projection (Fig. 1L, right inset, and fig. S5). This result indicated that in the BCC SL, the crystal lattice axis of Ag-NCs and the SL axis shared the same coordinate directions (i.e., $x$, $y$, and $z$ axes) (Fig. 1J and fig. S5), where maximized $\{111\}_{Ag\text{-}FCC}$-to-$\{111\}_{Ag\text{-}FCC}$ facet alignments are exhibited (supplementary text 1).

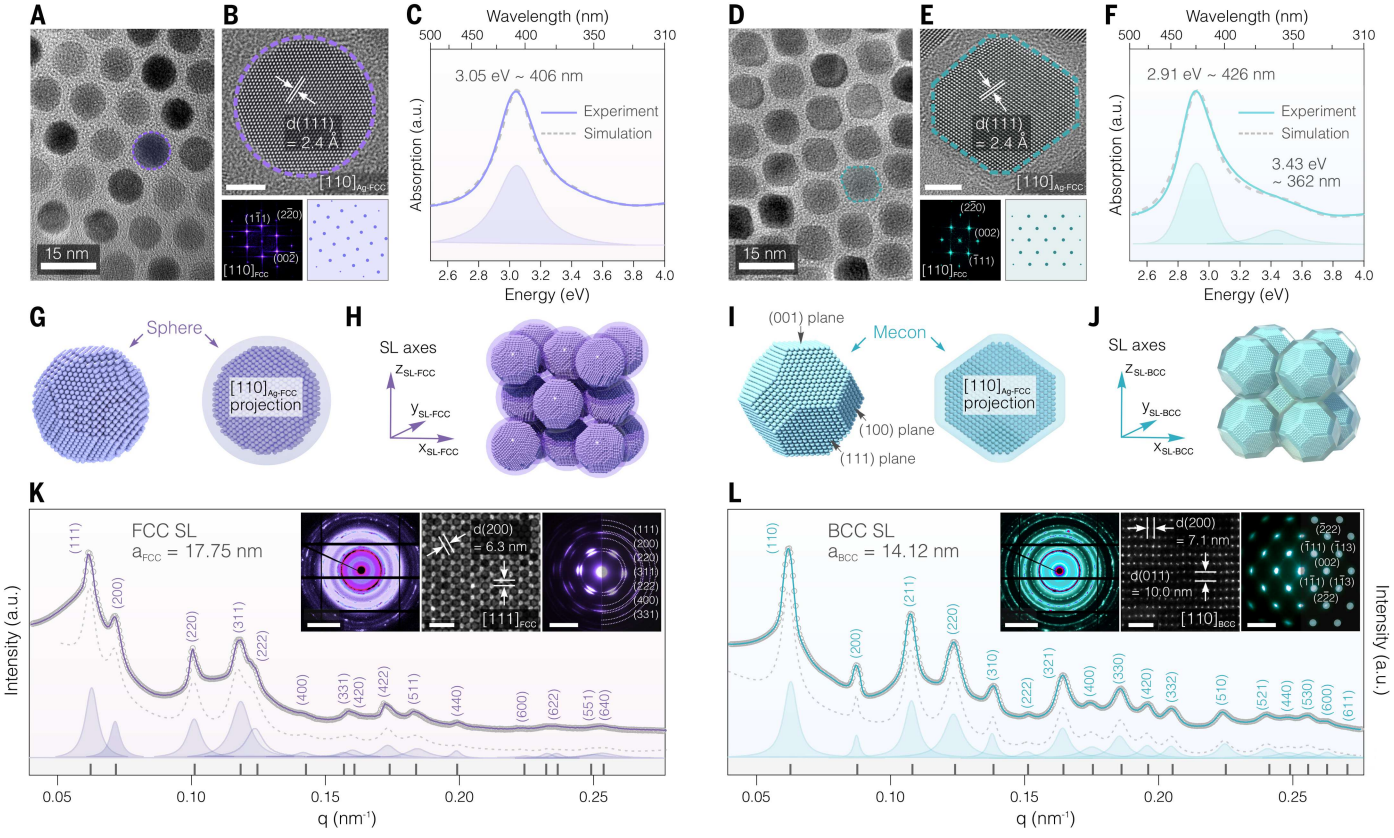


**Fig. 1. Spherical and mecon Ag-NCs and their SLs.** (**A** to **C**) Spherical Ag-NCs and (**D** to **F**) mecon Ag-NCs: low-magnification TEM images [(A) and (D)], HRTEM images (scale bar, 3 nm) [(B) and (E), top], the corresponding FFT patterns [(B) and (E), bottom left], simulated FFT patterns [(B) and (E), bottom right], and absorption spectra from experiments [(C) and (F), solid lines] and simulations [(C) and (F), dashed lines]. In (C), the presented peaks were used for fitting the experimental absorption spectra. a.u., arbitrary units. For presentation purposes, the TEM image in (E) was cropped, and the empty lower-left background region was digitally extended using matching background texture; no experimental features or data were modified. (**G** to **J**) Atomic models of an individual spherical Ag-NC (G), an FCC SL unit cell from spherical Ag-NCs (H), an individual mecon Ag-NC (I), and a BCC SL unit cell from mecon Ag-NCs (J). (**K** and **L**) One-dimensional (1D) SAXS spectra of an FCC SL from spherical Ag-NCs (K) and a BCC SL from mecon Ag-NCs (L). Open circles, solid lines, dashed lines, peaks, and bars in the panels represent integrated data points from the 2D SAXS patterns, 1D SAXS spectra, fitted SAXS spectra, constituent peaks for the fitting, and standard peak positions of the assigned structures, respectively. Insets: 2D SAXS patterns (scale bar, 0.5 $nm^{-1}$) (left), TEM images of the SLs (scale bar, 30 nm) (middle), and selected-area WAED patterns (scale bar, 3 $nm^{-1}$) (right). In the right inset panel of (K), the indices from top to bottom are assigned to the patterns corresponding to the inner to outer positions, respectively.

## Phase-intermediate SLs from truncated-mecon Ag-NCs

Next, we synthesized Ag-NCs with an intermediate shape between a mecon and a sphere (fig. S6 and supplementary text 2). To quantify the shapes, we defined a sphericity parameter, λ, where λ = 0 represents a perfect mecon and λ = 1 corresponds to a perfect sphere (supplementary text 2). TEM measurements confirmed excellent size and shape uniformities of the synthesized Ag-NCs with a λ of 0.62 (fig. S6), which were used to produce powder Ag-NC SLs. Synchrotron-based SAXS measurements revealed an intricate pattern, characterized by >30 well-resolved scattering peaks within the scattering vector **q** in the range from 0.05 to 0.30 $Å^{-1}$ (corresponding to a lattice spacing $d$ of 12.56 to 2.09 nm; Fig. 2A, fig. S7, and table S6).

This SAXS pattern could not be attributed to any common SL structures assembled in single-component NC systems, such as FCC, BCC, hexagonal close-packed (HCP), or any combination of these phases (fig. S8). Therefore, we examined phase-intermediate structures that arise during four common martensitic transformation pathways: Bain, Pitsch, N-W, and Kurdjumov-Sachs pathways (supplementary text 3) (*27*, *28*, *36*). Through structural analyses based on both real- and reciprocal-space results, we identified that the Ag-NC SLs had a phase-intermediate structure along the N-W martensitic transformation pathway (Fig. 2, A and D; figs. S7 to S15; and tables S6 and S7). N-W phase-intermediate unit cells are described using a base-centered monoclinic Bravais lattice (Fig. 2A, right inset, and supplementary text 3). In the N-W pathway, the crystallographic relationship with the reference FCC and BCC structures presents the $(001)_{SL\text{-}N\text{-}W}$ as the shared lattice plane with the $(111)_{SL\text{-}FCC}$ and $(011)_{SL\text{-}BCC}$ planes, and the shared directions of $[1\bar{1}0]_{SL\text{-}FCC}//[1\bar{1}0]_{SL\text{-}N\text{-}W}//[100]_{SL\text{-}BCC}$ and $[\bar{1}12]_{SL\text{-}FCC}//[\bar{1}00]_{SL\text{-}N\text{-}W}//[0\bar{1}1]_{SL\text{-}BCC}$ (Fig. 2B) (*27*, *28*, *36*). By descending the high symmetry ($O_h$ point group) of FCC or BCC structures to the lower symmetry ($C_{2/m}$ point group) of a N-W phase-intermediate structure, additional SAXS peaks emerge by gradually dissolving the peak degeneracy of the reference FCC or BCC lattices (Fig. 2C, fig. S11, table S7, and movie S1). Through fitting the SAXS pattern using the N-W unit cell, the lattice constants were determined to be $a$ = 19.58 nm, $b$ = 12.13 nm, $c$ = 12.13 nm, α = 90°, β = 128.6°, and γ = 90° (Fig. 2A, fig. S5, table S6, and Methods). This N-W phase-intermediate lattice comprises a 33.8% BCC (i.e., 66.2% FCC) structural contribution, defined as a phase-intermediate structural parameter ϒ = 33.8% (see supplementary text 3). The shared plane in the N-W phase-intermediate unit cell with ϒ = 33.8%, $(001)_{SL\text{-}N\text{-}W}$, exhibited a 4.5% expansion along the $[1\bar{1}0]_{SL\text{-}FCC}$ and 2.1% contraction along the $[\bar{1}12]_{SL\text{-}FCC}$ compared with the reference FCC phase (Fig. 2B and supplementary

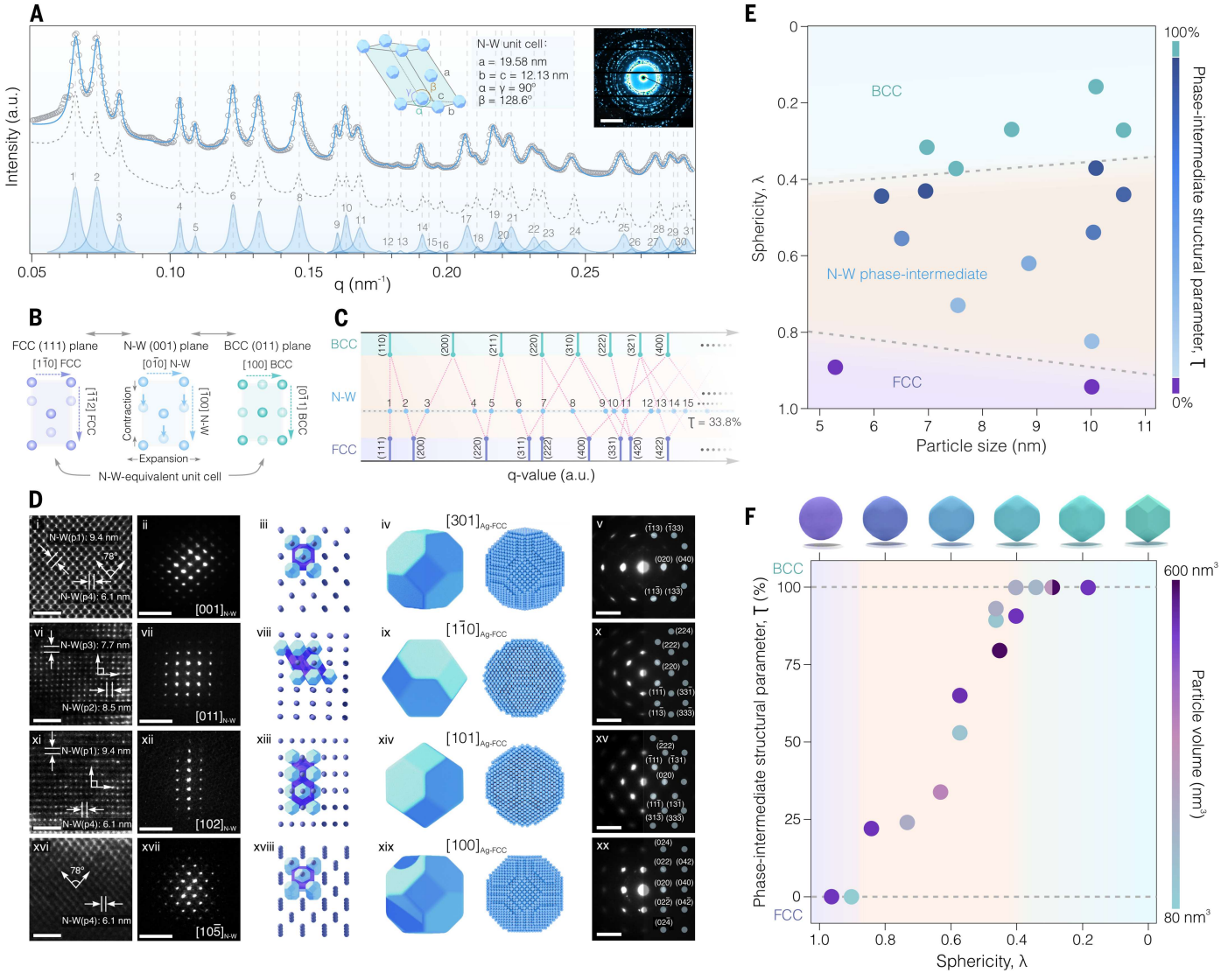


**Fig. 2. Characterizations and phase diagram of N-W phase-intermediate SLs.** (**A**) SAXS spectrum for a N-W phase-intermediate SL with Ƭ of 33.8% from Ag-NCs with λ of 0.62. Open circles, solid line, dashed line, and peaks represent integrated data points of 2D SAXS pattern, fitted SAXS spectrum, and constituent peaks for the fitting, respectively. Insets: N-W phase-intermediate unit cell and the lattice constants for the N-W phase-intermediate SLs with Ƭ of 33.8% (left) and 2D SAXS pattern (right; scale bar, 0.5 nm$^{-1}$). (**B**) Schematics of the shared plane through the N-W (middle) pathway between the reference FCC (left) and BCC (right) structures. The difference in the opacity of the spheres represents that they are located in different layers along the viewing directions. (**C**) Diagram of SAXS-peak evolution from an FCC (bottom) to a BCC (top) through the N-W pathway (middle). The numbers at the intersections along the line positioned at Ƭ of 33.8% (blue dots) correspond to the peak numbers assigned in the SAXS peaks shown in (A). (**D**) Rotational TEM study for the N-W phase-intermediate SL with Ƭ of 33.8%. Leftmost column (i, vi, xi, and xvi): TEM images showing SL fringes (scale bars, 40 nm). The SL fringes labeled as p1 to p4 correspond to SAXS peaks 1 to 4 in (A), respectively. Middle left column (ii, vii, xii, and xvii): the corresponding SAED patterns (scale bars, 0.2 nm$^{-1}$). Middle column (iii, viii, xiii, and xviii): computer models of the N-W SLs. Middle right column (iv, ix, xiv, and xix): computer models of the individual NCs in the SLs. Rightmost column (v, x, xv, and xx): the corresponding WAED patterns (scale bars, 3 nm$^{-1}$). (**E**) Phase diagram, λ versus particle size, plotted from 16 Ag-NC samples forming FCC, BCC, and N-W phase-intermediate SLs with different Ƭ values. (**F**) Phase diagram, Ƭ versus λ, plotted from 16 Ag-NC samples with different particle volumes and shapes (ranging between a sphere and a mecon). The complete dataset used for these diagrams is presented in table S8.

text 3). The obtained N-W phase-intermediate SLs showed high structural purity and remained stable for at least 6 months after formation despite their high structural complexity.

To identify the orientational order of the constituent Ag-NCs (λ = 0.62) within this phase-intermediate SL, we probed the structure from four distinct SL projections: $[001]_{SL-N-W}$, $[011]_{SL-N-W}$, $[102]_{SL-N-W}$, and $[10\bar{5}]_{SL-N-W}$ (Fig. 2D). Correlating the NC and SL orientations, the $[310]_{Ag-FCC}$, $[1\bar{1}0]_{Ag-FCC}$, $[101]_{Ag-FCC}$, and $[100]_{Ag-FCC}$ atomic orientation Ag-NCs were confirmed to align with the $[001]_{SL-N-W}$, $[011]_{SL-N-W}$, $[102]_{SL-N-W}$, and $[10\bar{5}]_{SL-N-W}$ SL projections, respectively (Fig. 2D, iv, ix, xiv, and xix). This orientation alignment was consistent with the assigned SL and atomic models (Fig. 2D and figs. S12 to S15). In the SL model, $\{111\}_{Ag-FCC}$-to-$\{111\}_{Ag-FCC}$ facet registrations between neighboring particles were consistently observed in the shared plane, $(001)_{SL-N-W}$, along the N-W pathway (Fig. 2B supplementary text 3). This retention of inter-$\{111\}_{Ag-FCC}$ facet registry in the shared planes exists in N-W phase-intermediate structures but not in any phase-intermediate configurations along other martensitic transformation pathways (supplementary text 3).

These findings suggest that interfacet interactions among Ag-NCs play a critical role in stabilizing this unusual N-W phase-intermediate SL (*24*, *25*, *40*–*42*).

To further demonstrate the general applicability of capturing N-W phase-intermediate structures, Ag-NCs with various sphericity parameters (λ from 0.11 to 0.95) and particle volumes (ranging from ~85 to 590 $nm^3$; particle size: 5.5 to 10.4 nm) were synthesized (fig. S16 and table S1) and assembled into SLs (Fig. 2, E and F; figs. S17 to S24; and tables S8 to S18). We found that N-W phase-intermediate SLs at different transitioning stages (0% < ϒ < 100%) can be produced from the Ag-NCs with λ between ~0.35 and ~0.85 (Fig. 2, E and F; fig. S17; and table S8). Increasing particle size broadens the stability window of the phase-intermediate SLs compared with smaller counterparts (Fig. 2E). Moreover, the phase-intermediate SL structural parameter, ϒ, shows a strong correlation following a sigmoid curve with the Ag-NC sphericity parameter, λ (Fig. 2F), indicating the phase-intermediate structural control and stabilization through precise engineering of particle shape. These results reveal a phase diagram containing a region where such highly dissymmetric structures can exist with a wide range of structural parameters (meaning that the full range of ϒ is accessible).

## Molecular dynamics simulations and mechanistic study

To investigate the formation mechanisms of the phase-intermediate structures, we developed minimal models of ligand-coated Ag-NCs and performed hard particle Monte Carlo (HPMC) and hard particle molecular dynamics (MD) simulations of the assembly processes (Fig. 3, A to F; figs. S25 to S29; and movies S2 to S8). We initially considered a hard particle model using the stiff interaction potential curve that accounts for the Ag-NC shape ($0 \leq \lambda \leq 1$) and therefore isolates the role of particle shape (Fig. 3A, purple dashed line, and movies S2 to

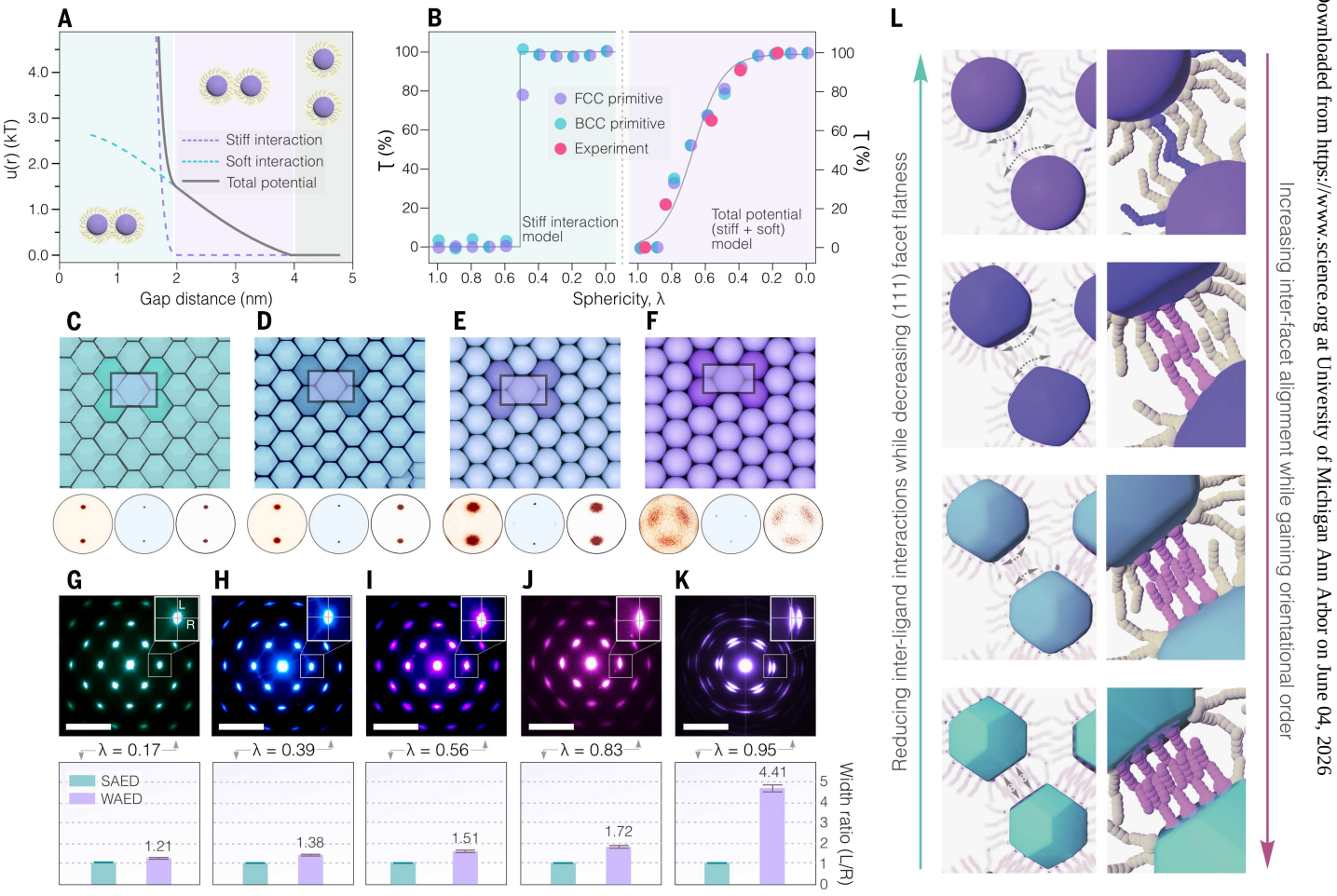


**Fig. 3. Simulations of phase-intermediate SL formation from NCs with varying sphericity parameters.** (**A**) Pair potential curves between NCs used in simulations. Potential curves for the stiff interaction model, the soft interaction model, and the total potential model (stiff and soft interactions combined) are presented with purple dashed, green dashed, and gray solid lines, respectively. See supplementary text 1 for the definition of gap distance. (**B**) Phase diagram, λ versus ϒ, plotted from HPMC simulations using the stiff interaction model (left) and MD simulations using the total potential model (right). Red spheres on the right panel represent experimentally obtained data from Ag-NCs with the same particle volume (~520 $nm^3$) and varying sphericity (λ: 0.17 to 0.95). Purple and cyan spheres represent simulation results starting from FCC and BCC configurations, respectively. (**C** to **F**) Structural analysis for simulated SLs from Ag-NCs with λ of 0.0 (C), 0.4 (D), 0.8 (E), and 1.0 (F): snapshots of the simulated SLs (top), FOODs for $(111)_{Ag\text{-}FCC}$ facets (bottom left), BOODs for eight nearest neighbors (bottom middle), and overlaid presentations of $(111)_{Ag\text{-}FCC}$ FOODs and eight nearest-neighbor BOODs (bottom right). (**G** to **K**) WAED patterns for the experimentally obtained SLs formed by the Ag-NCs (~520 $nm^3$) with λ of 0.17 (G), 0.39 (H), 0.56 (I), 0.83 (J), and 0.95 (K): WAED patterns (scale bars, 3 $nm^{-1}$) (top) and magnified signals with lines showing the longitudinal (L) and radial (R) directions (insets); the ratios of full width at half maximum between peaks integrated along the L and R directions for SAED (green bars) and WAED (purple bars) patterns (bottom). The corresponding SAED patterns used in this analysis are provided in fig. S29. (**L**) Computer models of neighboring NCs in the SLs with FCC (top), phase-intermediate (middle top, middle bottom), and BCC (bottom) structures, highlighting the evolution of orientational order of the constituent NCs and soft ligand–induced facet-to-facet interactions.

S5). However, the observed step function–like, abrupt transition from the BCC to an FCC lattice when $\lambda > 0.5$, which was consistent regardless of the starting structural configuration (Fig. 3B, left), indicated that the systems were unlikely to be kinetically arrested or otherwise trapped out of equilibrium (*43*). This result suggested that the hard particle model alone cannot explain the experimental observations of stabilized phase-intermediate structures (*43*).

Next, we added a soft repulsive interaction model between the particles to account for ligand-ligand interactions that we hypothesized could soften the shape of the Ag-NC core (Fig. 3A, gray solid line). MD simulations using this model (Fig. 3, A and B; figs. S25 to S27; and movies S6 to S8) demonstrated the self-assembly and stabilization of N-W phase-intermediate structures (Fig. 3B, right). The plots of $\lambda$ versus $\Upsilon$ from these simulations exhibited a smooth sigmoidal curve (Fig. 3B, right, blue and green spherical markers). Experimental data of SLs from Ag-NCs of identical particle volume (~520 $nm^3$) but varying shape ($\lambda$: 0.17 to 0.95) aligned well with the sigmoidal curve (Fig. 3B, right, red spherical markers; figs. S3, S4, and S30 to S33; and tables S4, S5, and S19 to S21), demonstrating the strong agreement between experiments and simulation.

Further examination of the simulated SLs from particles with $\lambda$ = 0, 0.4, 0.8, and 1.0 provides greater insights into the orientational ordering of Ag-NCs (Fig. 3, C to F, and fig. S29). Across all tested $\lambda$ values, the bond orientational order diagrams (BOODs), computed for each particle's eight nearest neighbors, perfectly matched the $\{111\}_{Ag\text{-}FCC}$ facet orientational order diagrams (FOODs) (Fig. 3, C to F, bottom right), demonstrating that the $\{111\}_{Ag\text{-}FCC}$ facets remained in contact in all the N-W phase-intermediate structures. Additionally, the FOODs of $\{111\}_{Ag\text{-}FCC}$ and $\{100\}_{Ag\text{-}FCC}$ facets display increasingly smeared signals with increasing $\lambda$ (Fig. 3, C to F, bottom left, and fig. S29), indicating a gradual loss of Ag-NC facet alignment. This gradual decrease of particle orientational order was also confirmed in experiments by closely analyzing the electron diffraction patterns of SLs assembled from Ag-NCs with the same volume of ~520 $nm^3$ and various $\lambda$ values of 0.17, 0.39, 0.56, 0.83, and 0.95 (Fig. 3, G to K, and fig. S30).

Although the SAED signals remained confined and spherical, the spot signals in the WAED patterns became increasingly smeared and elongated with increasing Ag-NC sphericity (Fig. 3, G to K, and fig. S30), which can be quantified by the width ratios of WAED peaks integrated along the longitudinal and radial directions (Fig. 3, G to K, purple bars, bottom, and fig. S34). This result indicates increased particle rotational freedom with increasing Ag-NC sphericity, which is associated with the less sharply faceted (111) planes, and thus weaker aligning torques, and reduced effective interfacet interactions (Fig. 3L and figs. S34 to S36) (*44*). The excellent agreement between simulation results and experimental findings suggested that the N-W pathway was favored by local interactions, particularly through $\{111\}_{Ag\text{-}FCC}$ facets, which remain preserved within the shared $(001)_{SL\text{-}N\text{-}W}$ plane (fig. S36 and supplementary text 3). Moreover, the tunable control over interaction magnitude enabled by shape-directed Ag-NC modifications and soft ligand interactions played a crucial role in stabilization of phase-intermediate SLs along the N-W martensitic pathway.

## Light-matter coupling in SL films

Metallic NC SLs exhibit optical properties that arise from the light-matter coupling of their collective plasmons (*23*, *26*, *32*, *33*, *45*–*49*). The interaction between plasmons localized on different NCs generates collective excitations that hybridize with photons into plasmon polaritons, as previously demonstrated for spherical gold NC SLs (*33*). Because Ag-NCs are among the most plasmonic-responsive particles (*38*, *39*), we measured optical responses of Ag-NC SLs with different numbers of NC layers in both transmission and reflection modes (Fig. 4, A to D, and figs. S37 to S41). For all three SL architectures—FCC SLs from spherical Ag-NCs, phase-intermediate SLs from Ag-NCs with $\lambda$ = 0.56, and BCC SLs from mecon Ag-NCs—the transmission and reflection features shifted continuously toward lower energy, and new peaks emerged upon increasing the number of Ag-NC SL layers from one to six (Fig. 4, E to G, and figs. S39 and S40). Numerical simulations of the optical spectra with a finite-difference time-domain software package reproduced the experimental spectra with excellent agreement (fig. S39). In the simulated 24-layer slabs, strong minima in reflectance below 2 eV arose from plasmon polariton standing waves across the SL slabs (Fig. 4H). Between 2 and 4 eV, the total transmission dropped to zero (Fig. 4H), consistent with the opening of a polaritonic gap in the electromagnetic spectrum. Such a gap is a hallmark of ultrastrong and deep-strong light-matter coupling, in which the coupling strength becomes comparable to, or exceeds, the bare excitation frequency, invalidating the conventional weak-coupling approximation and leading to nonperturbative light-matter hybridization and a qualitatively modified polaritonic dispersion (*23*, *33*). The Ag-NC SLs with fewer particle layers displayed less pronounced transmission and reflection features (Fig. 4, E to G) because the SL thicknesses (<60 nm) were much less than the polariton wavelength (~150 nm for visible frequencies).

We quantified light-matter coupling in the Ag-NC SLs by extracting the plasmon polariton energies from the simulated spectra and fitting them to a polaritonic Hopfield dispersion to determine the transverse collective plasmon frequency, $\omega_t$, and the vacuum Rabi frequency, $\Omega_R$ (Fig. 4, H and I; see methods) (*33*, *47*). Note that the experimentally determined polariton dispersion points agreed well with the polaritonic Hopfield dispersion fitted to simulations (Fig. 4I). All three SLs exhibit Rabi frequencies of >2 eV (FCC: 2.25 eV; phase-intermediate: 2.49 eV; BCC: 2.43 eV), exceeding their corresponding transverse collective plasmon energies (FCC: 2.16 eV; phase-intermediate: 2.37 eV; BCC: 2.30 eV) (Fig. 4, H and I). The resulting reduced coupling strengths, $\eta = \Omega_R/\omega_t$, thus reached the deep-strong light-matter coupling region ($\eta > 1$) for all three SLs with a gradual and consistent increase from FCC ($\eta$ = 1.04), to phase-intermediate ($\eta$ = 1.05), to BCC ($\eta$ = 1.06) (*33*, *47*).

These results demonstrate how the stable phase-intermediate structure provided an experimentally accessible structural bridge that traces the evolution of optical coupling across the FCC-BCC transformation pathway. The space-filling characteristic of the mecon shape in a BCC structure potentially allows such SLs to surpass the maximum packing fraction of 74% possible with FCC SLs from spheres. Simulations of a tight BCC structure with a packing fraction of 84.5% by reducing interparticle distance reached a decreased transverse collective plasmon frequency of $\omega_t$ =1.54 eV and an increased Rabi frequency of $\Omega_R$ = 2.77 eV (Fig. 4I and fig. S41). As a result, a much higher reduced coupling strength, $\eta$ = 1.80, was obtained, which has never before been reported for particles of such small size.

We can establish a unified design framework for achieving deep-strong coupling in self-assembled plasmonic NC SLs under ambient conditions. (i) Packing fraction: Increasing the packing fraction of inorganic plasmonic cores while minimizing surfactant volume enhances collective coupling, leading to larger coupling constants and stronger polariton states (*50*). This trend is supported by simulations of mecon Ag-NC SLs, where reducing interparticle distance or increasing NC size both resulted in higher coupling strength (fig. S42 and table S22). In contrast, variations in Bravais lattice symmetry, minor distortions, or local disorder play only secondary roles. (ii) Shape engineering: Nonspherical, space-filling geometries, such as mecon-like–shaped NCs, can surpass the 74% packing limit of spheres, thereby further amplifying coupling strength. Simulations of BCC SLs assembled from 59-nm mecon Ag-NCs achieved a high packing fraction of 95.1% and a coupling constant of $\eta$ = 2.59, well exceeding those of FCC SLs composed of spherical Ag-NCs of identical size and interparticle distance (packing fraction of 70.4%, $\eta$ = 1.36; table S22). (iii) Material selection: Materials with higher free-electron densities, such as coinage metals, exhibit stronger plasmonic oscillators and thus larger coupling strength (*23*, *33*, *50*). Consistently, the simulated FCC SLs composed of spherical Ag- and Au-NCs (identical size of 59 nm) both exhibited

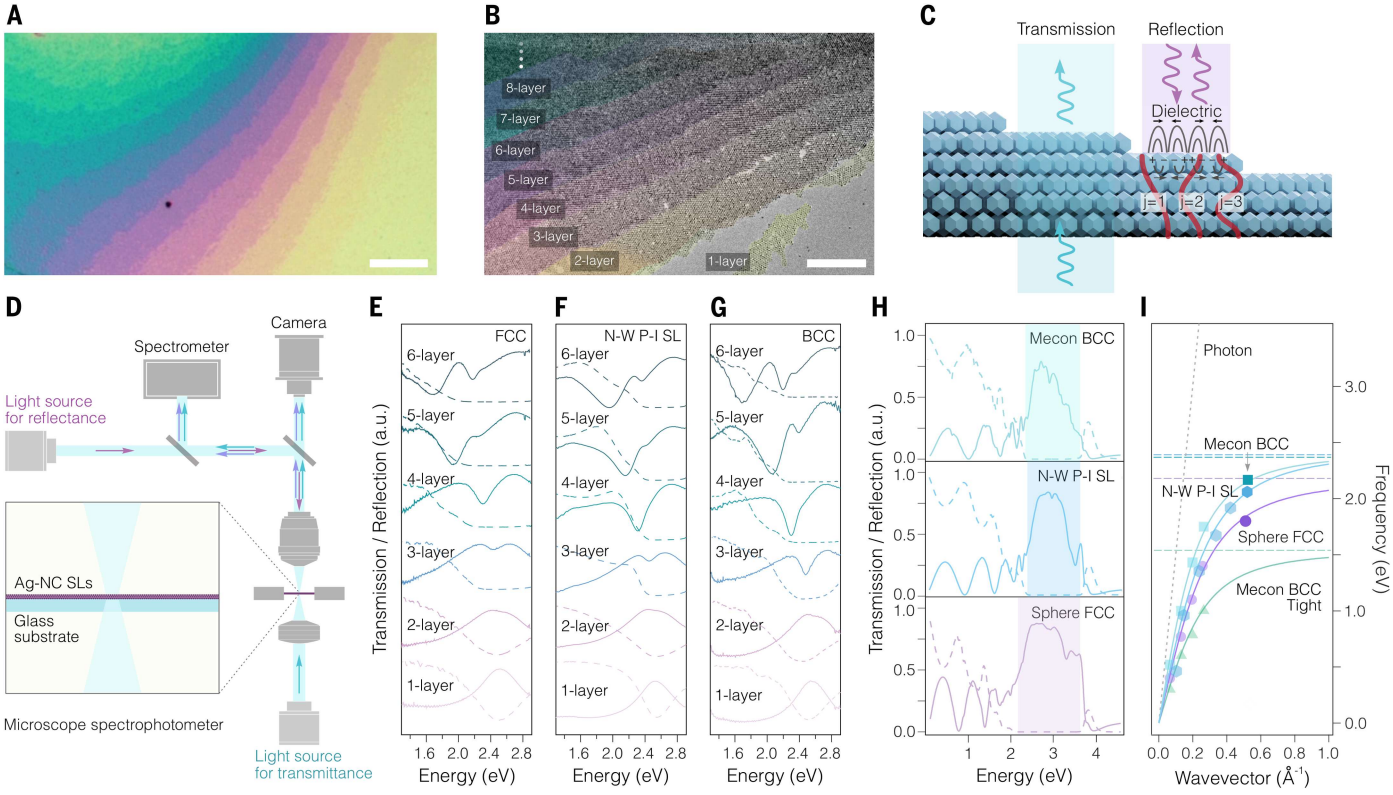


**Fig. 4. Plasmonic properties of Ag-NC SLs.** (**A**) Reflection optical image of BCC SLs from mecon Ag-NCs (scale bar, 40 μm). (**B**) TEM image of BCC SLs from mecon Ag-NC with varying numbers of stacked layers (scale bar, 300 nm). (**C**) Schematic representation of transmission and reflection spectroscopy used in this study, along with the light-matter couplings emerging at the surface of (e.g., surface polariton) and within Ag-NC SLs (e.g., plasmon polariton standing waves). (**D**) Schematic illustration of the optical path applied in the measurements. (**E** to **G**) Experimental transmission (dashed lines) and reflection (solid lines) spectra of one to six layers (E) FCC SLs from spherical Ag-NCs, (F) N-W phase-intermediate (P-I) SLs from Ag-NCs with λ of 0.56, and (G) BCC SLs from mecon Ag-NCs. (**H**) Simulated reflection (solid lines) and transmission (dashed lines) spectra of a BCC SL from mecon Ag-NCs (top), a N-W P-I SL from Ag-NCs with λ of 0.56 (middle), and an FCC SL from spherical Ag-NCs (bottom) with 24 SL layers (1.3 nm gap distance). The color-shaded areas indicate the polaritonic bandgaps that develop for ultrastrong and deep-strong light-matter coupling. The dips in reflectivity within the gap are due to absorption by higher-order plasmonic modes. (**I**) Dispersion of the lower plasmon polaritons for BCC SLs from mecon Ag-NCs (square), N-W P-I SLs from Ag-NCs with λ of 0.56 (hexagon), FCC SLs from spherical Ag-NCs (sphere), and tight BCC SLs from mecon Ag-NCs with a reduced interparticle gap distance (0.5 nm gap distance; triangles). Light-colored symbols are extracted from the simulations, and the dark-colored symbols (square, hexagon, and sphere) are the data points obtained from experimental measurements (BCC SL from spherical Ag-NCs, N-W P-I SL from Ag-NCs with λ of 0.56, and FCC SLs from mecon Ag-NCs, respectively). The solid lines, dashed lines, and dotted gray lines are the fitting lines with a Hopfield Hamiltonian; fitted transverse collective plasmon frequency, $\omega_t$; and free photon dispersion, respectively.

large coupling constants of 1.36 and 1.32, respectively (table S22) (*33*). The slightly higher value of Ag-NCs likely stems from their lower intrinsic losses relative to Au-NCs (*23*, *33*, *50*). Together, these insights establish a unifying design principle: Maximizing free-carrier densities and core packing through shape-engineered architectures provides an effective route to achieving and tuning deep-strong light-matter coupling in self-assembled plasmonic SLs.

## Discussion

Our study demonstrates that mecon-like Ag-NCs can self-assemble into SLs with stable dissymmetric configurations—structures that would typically be transient, if observed at all, along the N-W martensitic pathway. By precisely tailoring Ag-NC shapes, we achieve SLs spanning the entire transformation trajectory from FCC and BCC arrangements. These assemblies define a previously unobserved, symmetry-breaking phase domain, offering a framework for understanding structural phase transitions by stabilizing otherwise elusive intermediate states. By capturing and structurally resolving such phase-intermediate states in a model NC system, our work provides an experimentally tractable analog that can deepen the fundamental understanding of martensitic transformation pathways in metallic systems (*51*). Moreover, all Ag-NC SLs studied exhibited deep-strong light-matter coupling through plasmon polariton hybridization, enabling a unified design principle for unlocking this emergent quantum phenomenon. Together, these findings underline the promise of Ag-NC assemblies for practical applications in photonics, optical metamaterials, and quantum technologies. We envision that this work will inspire new design strategies for accessing diverse phase-intermediate superstructures, assembled from building objects across multiple length scales, paving the way for transformative advancements in materials science and next-generation technologies.

## REFERENCES AND NOTES

1. G. M. Whitesides, B. Grzybowski, *Science* **295**, 2418–2421 (2002).
2. D. Kondepudi, I. Prigogine, *Modern Thermodynamics: From Heat Engines to Dissipative Structures* (Wiley, ed. 2, 2014).
3. M. A. Boles, M. Engel, D. V. Talapin, *Chem. Rev.* **116**, 11220–11289 (2016).
4. S. Lee, T. Vo, S. C. Glotzer, *Nat. Chem.* **15**, 905–912 (2023).
5. B. A. Grzybowski, W. T. Huck, *Nat. Nanotechnol.* **11**, 585–592 (2016).
6. Y. Nagaoka, J. Schneider, H. Zhu, O. Chen, *Matter* **6**, 30–58 (2023).

7. C. L. Bassani *et al.*, *ACS Nano* **18**, 14791–14840 (2024).
8. T. Xiao *et al.*, *Science* **377**, 870–874 (2022).
9. M. C. Weidman, D. M. Smilgies, W. A. Tisdale, *Nat. Mater.* **15**, 775–781 (2016).
10. D. W. Yee, M. S. Lee, J. An, R. J. Macfarlane, *J. Am. Chem. Soc.* **145**, 6051–6056 (2023).
11. D. A. Porter, K. E. Easterling, M. Y. Sherif, *Phase Transformations in Metals and Alloys* (CRC Press, ed. 3, 2009).
12. J. L. Greenfield *et al.*, *Chem. Sci.* **12**, 8589–8602 (2021).
13. S. Y. Schmid *et al.*, *Angew. Chem. Int. Ed.* **62**, e202309725 (2023).
14. A. Parija, G. R. Waetzig, J. L. Andrews, S. Banerjee, *J. Phys. Chem. C* **122**, 25709–25728 (2018).
15. Q. Yun *et al.*, *Chem. Rev.* **123**, 13489–13692 (2023).
16. Y. Han *et al.*, *Chem. Rev.* **123**, 14119–14184 (2023).
17. Y. Zhang *et al.*, *Nat. Mater.* **14**, 840–847 (2015).
18. C. B. Williamson *et al.*, *Science* **363**, 731–735 (2019).
19. Z. Cheng, M. R. Jones, *Nat. Commun.* **13**, 4207 (2022).
20. P. Kumar *et al.*, *Nature* **615**, 418–424 (2023).
21. M. Yankowitz *et al.*, *Science* **363**, 1059–1064 (2019).
22. S. Wan *et al.*, *Science* **387**, 978–984 (2025).
23. A. F. Kockum, A. Miranowicz, S. De Liberato, S. Savasta, F. Nori, *Nat. Rev. Phys.* **1**, 19–40 (2019).
24. Y. Nagaoka *et al.*, *Nature* **561**, 378–382 (2018).
25. Y. Nagaoka, H. Zhu, D. Eggert, O. Chen, *Science* **362**, 1396–1400 (2018).
26. J. Henzie, M. Grünwald, A. Widmer-Cooper, P. L. Geissler, P. Yang, *Nat. Mater.* **11**, 131–137 (2011).
27. Z. Nishiyama, *Martensitic Transformation* (Academic Press, 1978).
28. H. Sowa, *Acta Crystallogr. A Found. Adv.* **73**, 39–45 (2017).
29. L. H. Zhang, M. J. Cheng, X. H. Shi, J. W. Shuai, Z. Z. Zhu, *RSC Adv.* **11**, 3043–3048 (2021).
30. H. Y. Chao *et al.*, *Chem. Rev.* **123**, 8347–8394 (2023).
31. G. Rainò, H. Utzat, M. G. Bawendi, M. V. Kovalenko, *MRS Bull.* **45**, 841–849 (2020).
32. K. Bian *et al.*, *Nat. Commun.* **9**, 2365 (2018).
33. N. S. Mueller *et al.*, *Nature* **583**, 780–784 (2020).
34. M. Cargnello *et al.*, *Nature* **524**, 450–453 (2015).
35. W. Zhou *et al.*, *Science* **383**, 312–319 (2024).
36. H. Pan, J. Dshemuchadse, *Proc. Natl. Acad. Sci. U.S.A.* **122**, e2507403122 (2025).
37. R. B. Fuller, E. J. Applewhite, A. L. Loeb, *Synergetics: Explorations in the Geometry of Thinking* (Macmillan, 1975).
38. B. J. Wiley *et al.*, *J. Phys. Chem. B* **110**, 15666–15675 (2006).
39. S. Peng, J. M. McMahon, G. C. Schatz, S. K. Gray, Y. Sun, *Proc. Natl. Acad. Sci. U.S.A.* **107**, 14530–14534 (2010).
40. Y. Nagaoka *et al.*, *J. Am. Chem. Soc.* **146**, 13093–13104 (2024).
41. Z. Quan, J. Y. Fang, *Nano Today* **5**, 390–411 (2010).
42. J. Gong *et al.*, *Nat. Commun.* **8**, 14038 (2017).
43. C. X. Du, G. van Anders, R. S. Newman, S. C. Glotzer, *Proc. Natl. Acad. Sci. U.S.A.* **114**, E3892–E3899 (2017).
44. G. van Anders, N. K. Ahmed, R. Smith, M. Engel, S. C. Glotzer, *ACS Nano* **8**, 931–940 (2014).
45. M. Herran *et al.*, *Nat. Catal.* **6**, 1205–1214 (2023).
46. Z. Zhu *et al.*, *Angew. Chem. Int. Ed.* **50**, 1593–1596 (2011).
47. E. B. Barros, B. G. Vieira, N. S. Mueller, S. Reich, *Phys. Rev. B* **104**, 035403 (2021).
48. T. Paul, A. M. Green, D. J. Milliron, T. M. Truskett, *ACS Photonics* **12**, 5682–5696 (2025).
49. S. De Liberato, *Nat. Commun.* **8**, 1465 (2017).
50. F. Schulz *et al.*, *Nat. Commun.* **11**, 3821 (2020).
51. K. Bhattacharya, S. Conti, G. Zanzotto, J. Zimmer, *Nature* **428**, 55–59 (2004).


## ACKNOWLEDGMENTS

This research used the Electron Microscopy Facility at the Center for Functional Nanomaterials, CMS, and FIS beamlines of the National Synchrotron Light Source II, a US Department of Energy (DOE), Office of Science User Facility, operated for the DOE, Office of Science, by the Brookhaven National Laboratory under contract DE-SC0012704. This work used the Delta system at the National Center for Supercomputing Applications (award OAC 2005572, allocation DMR 140129) from the Advanced Cyberinfrastructure Coordination Ecosystem: Services & Support (ACCESS) program, which is supported by National Science Foundation (NSF) grants 2138259, 2138286, 2138307, 2137603, and 2138296. **Funding:** This work was supported by NSF grants DMR-1943930 and CHE-2203700 and the Camille and Henry Dreyfus Foundation through the Camille Dreyfus Teacher-Scholar Awards Program (O.C.); DOE, Office of Science, grant DE-SC0012704 (Brookhaven National Laboratory); NSF grant EAR—2223273 and DOE-NNSA cooperative agreement DE-NA-0003975 (Argonne); NSF grants CBET-2230729 and CBET-2230891 (S.Z.); European Research Council grant CoG DarkSERS, 772108, and the German Science Foundation grant DFG 504656879 (S.R.); a Vannevar Bush Faculty Fellowship through the Department of the Navy, Office of Naval Research, N00014-22-1-2821 and NSF cooperative agreement 2243104 [Center for Complex Particle Systems (COMPASS) Science and Technology Center] (S.C.G.). **Author contributions:** Conceptualization: Y.N., O.C.; Methodology: Y.N., T.C.M., A.E., Z.L., A.W., S.Z., S.R., S.C.G., O.C.; Investigation: Y.N., T.C.M., A.E., Z.L., T.C., N.J., K.S.H., P.S., A.W., Y.L., S.H., Y.B., S.Z., R.L.; Visualization: Y.N., T.C.M., S.C.G., O.C.; Funding acquisition: Y.L., Y.B., S.Z., S.R., S.C.G., O.C.; Supervision: S.R., S.C.G., O.C.; Writing – original draft: Y.N., O.C.; Writing – review & editing: Y.N., T.C.M., A.E., Z.L., T.C., N.J., K.S.H., P.S., A.W., Y.L., S.H., Y.B., S.Z., R.L., S.R., S.C.G., O.C. **Competing interests:** The authors declare that they have no competing interests. **Data, code, and materials availability:** All data are available in the main text or the supplementary materials. 

## SUPPLEMENTARY MATERIALS

science.org/doi/10.1126/science.ady6472
Materials and Methods; Supplementary Text; Figs. S1 to S42; Tables S1 to S22; References (*52*–*66*); Movies S1 to S8

Submitted 29 April 2025; accepted 8 April 2026

10.1126/science.ady6472

# Stabilizing in-transition phases of superlattices through shape control of silver nanocrystals

Yasutaka Nagaoka, Timothy C. Moore, Arseniy Epishin, Zhenyang Liu, Tong Cai, Na Jin, Ken Seungmin Hong, Peter Saghy, Ankai Wang, Yuzi Liu, Sooyeon Hwang, Yusong Bai, Shengli Zou, Ruipeng Li, Stephanie Reich, Sharon C. Glotzer, and Ou Chen

*Science* **392** (6801), . DOI: 10.1126/science.ady6472

**Editor's summary**

Phase transitions between ordered lattices often pass through short-lived intermediate structures that are difficult to capture and study. Through the self-assembly of silver nanocrystals with shapes ranging from spheres to truncated octahedra, Nagaoka *et al*. observed a structural evolution from face-centered cubic to body-centered cubic superlattices. Nanocrystals with intermediate shapes formed a stable, dissymmetric superlattice corresponding to an otherwise transient structure along the Nishiyama-Wasserman martensitic pathway. —Jack Huang

Science
AAAS

# Supplementary Materials for

## Stabilizing in-transition phases of superlattices through shape control of silver nanocrystals

Yasutaka Nagaoka *et al*.

Corresponding authors: Sharon C. Glotzer, sglotzer@umich.edu; Ou Chen, ouchen@brown.edu

*Science* **392**, 951 (2026)
DOI: 10.1126/science.ady6472

**The PDF file includes:**



**Other Supplementary Material for this manuscript includes the following:**

## Materials and Methods

### Materials

Silver acetate (Ag-acetate, 99.99% trace metal basis), copper (II) acetate ($Cu(acetate)_2$, 97%), oleic acid (OAcid, technical grade 90 %), oleylamine (OAm, technical grade 70 %), diphenyl ether (DPE, for synthesis), hydrochloride acid (HCl, 37%, ACS reagent), 4-*tert*-butyltoluene (95%), toluene (certified ACS), hexanes (certified ACS), acetone (certified ACS), and dimethylformamide (DMF, certified ACS) were purchased from Aldrich.

### Methods

Synthesis of Ag-NCs

Ag-NCs were synthesized using a heating-up method via a decomposition reaction. Typically, 334 mg (2 mmol) of Ag-acetate, 1.8 mg (0.01 mmol) of $Cu(acetate)_2$, 1 μL of HCl, and 14 mL of a mixture of OAcid, OAm, and DPE (Table S1) were loaded into a 100-mL flask. The solution was degassed under vacuum for 5 minutes at room temperature, then heated to 45 °C for 10 minutes, followed by heating to 80 °C for 20 minutes. Under a nitrogen blanket, the solution was further heated to a designated temperature (between 130 °C and 180 °C), which was typically reached within 5–10 min without overshooting (i.e., 10 °C/min). The reaction solution was then maintained for 5–20 minutes (Table S1). After the reaction was completed, the flask was swiftly cooled to room temperature using an ice-water bath (i.e., 30 °C/min). Hexane was added to the crude reaction mixture until no flocculation was observed, after which acetone was added until light-brown flocculation appeared. The product was isolated by centrifugation (8000 rpm for 5 min), and the resulting Ag-NCs were stored in hexane.

Annealing experiments for Ag-NCs from mecons to spheres

For Ag-NCs with identical volumes but different sphericity values, we conducted annealing experiments. Initially, mecon Ag-NCs were synthesized. After purification and collection, 15 mg of the Ag-NCs were redispersed in a mixture of 8 mL of 4-tert-butyltoluene and 2 mL of OAm in a flask. Following three cycles of freeze-pump-thaw degassing, the solution was heated to 160 °C (Table S2). The reaction was monitored by measuring the absorption peak of aliquots. To collect the samples, the reaction flask was rapidly cooled to room temperature using an ice-water bath. The product was collected via centrifugation, followed by precipitation with acetone. The resulting Ag-NCs were stored in hexane, and TEM measurements were carried out to confirm the sphericity values of the products.

Detailed synthetic protocols for spherical, mecon-shaped, and intermediate-shaped ($\lambda = 0.62$) Ag-NCs used in Figures 1 and 2 (see also Tables S1 and S2).

Synthesis of mecon-shaped Ag-NCs: 333 mg of Ag-acetate, 1.9 mg $Cu(acetate)_2$, 1 μL of HCl, 1 mL of OAcid, 1 mL of OAm, and 12 mL of DPE were loaded into a 100-mL flask. The solution was degassed under vacuum for 5 minutes at room temperature, then heated to 45 °C for 10 minutes, followed by heating to 80 °C for 20 minutes. Under a nitrogen blanket, the solution was quickly heated to 180 °C (ca., 10 °C/min) and maintained for 5 minutes. After the reaction was

completed, the flask was swiftly cooled to room temperature using an ice-water bath. The product was collected via centrifugation following precipitation with acetone, and the resulting Ag-NCs were stored in hexane.

Synthesis of spherical Ag-NCs: The synthesized mecon Ag-NCs described above were used as the initial materials and transformed into spherical Ag-NCs through annealing process. Specifically, 15 mg of the mecon-shaped Ag-NCs were redispersed in a mixture of 8 mL of 4-tert-butyltoluene and 2 mL of OAm in a flask. Following three cycles of freeze-pump-thaw degassing using liquid nitrogen, the solution was heated to 200 °C and kept for 5 min. To collect the samples, the reaction flask was rapidly cooled to room temperature using an ice-water bath. The product was collected via centrifugation, followed by precipitation with acetone.

Synthesis of intermediate-shaped Ag-NCs with $\lambda = 0.62$: 334 mg of Ag-acetate, 1.9 mg $Cu(acetate)_2$, 1 µL of HCl, 2 mL of OAcid, 2 mL of OAm, and 10 mL of DPE were loaded into a 100-mL flask. The solution was degassed under vacuum for 5 minutes at room temperature, then heated to 45 °C for 10 minutes, followed by heating to 80 °C for 20 minutes. With an identical volume with different sphericity values, we conducted annealing experiments. Under a nitrogen blanket, the solution was further heated to 150 °C (ca., 10 °C/min) and maintained for 5 minutes. After the reaction was completed, the flask was swiftly cooled to room temperature using an ice-water bath. The product was collected via centrifugation following precipitation with acetone, and the resulting Ag-NCs were stored in hexane.

## Preparation of Ag-NC SLs

All Ag-NC SLs presented in this study were prepared via a slow solvent evaporation process. Specifically, 4 mL of Ag-NC solution in hexane (10 mg/mL) was placed in a capped vial and allowed to dry over 3-6 weeks. This slow evaporation process is critical for obtaining structurally rigid SLs with sharp and well-defined SAXS peaks. The film samples for TEM and optical measurements were prepared using a liquid-air interface method. A 0.1-mL hexane solution of Ag-NCs (1 mg/mL) was placed on a pool of dimethylformamide in a 20-mL glass vial. Typically, evaporation took around 10 minutes, during which the Ag-NC SL films formed on the liquid substrate. The floating Ag-NC SLs were collected onto a desired substrate (e.g., TEM grid, glass substrate) for further measurements.

## Instruments and software

TEM and selected-area ED measurements were performed on a JEOL-2100F microscope, operated at 200 kV. For SAED and WAED measurements, camera lengths of 200 cm and 12 cm were used, respectively. Scanning electron microscopy measurements were performed on a LEO-1530, operated at 5 kV. High-angle annular dark-field scanning transmission electron microscopy (HAADF-STEM) images were acquired with a Hitachi HD 2700C dedicated STEM, equipped with a probe Cs corrector, and operated at 200 kV. HAADF-TEM was performed on an FEI Talos F200X TEM/STEM, also operating at 200 kV. Powder X-ray diffraction patterns were obtained on a Bruker D8 Discovery 2D X-ray Diffractometer, equipped with a Vantec 500 2D area detector and operating with Cu Kα ($\lambda = 1.541$ Å) radiation. Absorption spectra were measured using an Agilent Technologies Cary 5000 UV-Vis-NIR Spectrophotometer. Optical microscopic images, including bright-field, dark-field, and reflection modes, were acquired with the 508 PV

Microscope Spectrophotometer (CRAIC Technologies) and Nikon Eclipse LV150N (Nikon). The reflectance and transmission spectra were collected from a selected area of 5 μm × 5 μm. Computer models were constructed using Autodesk 3ds Max (Autodesk).

Synchrotron-based SAXS measurements

Synchrotron-based transmission SAXS measurements were conducted at the Complex Materials Scattering beamline at the National Synchrotron Light Source II at Brookhaven National Laboratory. At the National Synchrotron Light Source II, the X-ray beam (with an energy of 13.5 keV and a beam size of 0.2 × 0.2 mm) was directed to the sample, and the scattering signal was collected by a Pilatus 2M detector. A mixture of cerium oxide powders was used to calibrate the sample-to-detector distances and the detector settings parameters. This protocol generated 2D SAXS patterns. 1D SAXS plots of scattering vector (q) vs. signal intensity in log10 scale were generated by circularly integrating the 2D SAXS patterns from the beam center.

Determinations of Ƭ values and lattice constants for phase-intermediate NC SLs

The lattice constants for N-W phase-intermediate SLs were determined through the least-square method by minimizing the difference between experimental and calculated values in SAXS peak positions. Given Ƭ and *ucc* (unit cell constant, which is applied to normalize *a*, *b*, *c* unit cell parameters) for a N-W SL, the lattice constants, *a*, *b*, *c*, α, β, and γ are expressed as below:

$$
\begin{aligned}
a/ucc &= 1.73205 - Ƭ \times 0.09906 \\
b/ucc &= 1.00000 + Ƭ \times 0.15470 \\
c/ucc &= 1.00000 + Ƭ \times 0.15470 \\
\alpha &= 90^{o} \\
\beta &= 125.265^{o} + Ƭ \times 9.735^{o} \\
\gamma &= 90^{o}
\end{aligned}
\qquad \text{(Eq. 1)}
$$

The detailed structures and geometrical characteristics for N-W phase-intermediate unit cell are described in Supplementary Text 3. Using these lattice constants, d-spacings(*hkl*) can be calculated using Eq. 2:

$$\frac{1}{d^2(hkl)} = \frac{1}{V^2}(S_{11}h^2 + S_{22}k^2 + S_{33}l^2 + 2S_{12}hk + 2S_{23}kl + 2S_{13}hl) \qquad \text{(Eq. 2)}$$

Where the coefficients are defined as:

$$S_{11} = b^2c^2\sin^2\alpha$$

$$S_{22} = a^2c^2\sin^2\beta$$
$$S_{33} = a^2b^2\sin^2\gamma$$
$$S_{12} = abc^2(\cos\alpha\cos\beta - \cos\gamma)$$
$$S_{23} = a^2bc(\cos\beta\cos\gamma - \cos\alpha)$$
$$S_{13} = ab^2c(\cos\gamma\cos\alpha - \cos\beta)$$
$$V = abc\sqrt{1 - \cos^2\alpha - \cos^2\beta - \cos^2\gamma + 2\cos\alpha\cos\beta\cos\gamma}$$

Using the experimentally determined d-spacing values from SAXS peaks, *ucc* and Ţ are treated as variables and optimized by minimizing the discrepancy between calculated and measured d-spacing values.

Calculation of simulated SAXS spectra of NC SLs

The simulated SAXS spectra, *I(q),* were calculated using the form factors of the building block Ag-NCs, *P(q),* and the structural factors of the SLs, *S(q)*, as shown in Eq. 3:(*52-54*)

$$I(q) = P(q)S(q) + BL(q) \quad \text{(Eq. 3)}$$

where *BL(q)* is the baseline. We calculated *P(q) S(q),* and *BL(q)* using the equations below within the relevant q-range, then convoluted at each q-point. The convolution of *P(q)* and *S(q)* was done using Microsoft Excel.

*Baseline calculation*

A linear function on a logarithmic scale was used to represent the baseline, expressed as Eq. 4:

$$log_{10}BL(q) = a + b \cdot q \quad \text{(Eq. 4)}$$

where *a* and *b* are the y-axis intercept and slope, respectively. These values were selected to match the simulated spectra with the experimentally obtained data.

*Form factor calculation*

The form factors were calculated using Eq. 5 and 6, with the parameters (average diameter and standard deviation) obtained from TEM measurements.

$$P(q) = \left( \left( \frac{3}{(q \cdot d(r \cdot \sigma))^3} \right) (\sin(q \cdot d(r \cdot \sigma)) - q \cdot d(r \cdot \sigma) \cos(q \cdot d(r \cdot \sigma))) \right)^2 \quad \text{(Eq. 5)}$$

$$d(r \cdot \sigma) = r \times \frac{1}{\sigma\sqrt{2\pi}} e^{-\frac{1}{2}\left(\frac{q-r}{\sigma}\right)^2} \quad \text{(Eq. 6)}$$

where *d*, *r*, and *σ* represent the size distribution, the average radius, and the standard deviation of the building blocks, respectively.

*Structural factor calculation*

The structure factors for the SLs were obtained from the powder diffraction function in *CrystalMaker* using the assigned lattice constants.

We determined the lattice constants for the NC SLs used in this study using the least-squares methods. For FCC and BCC SLs, we used lattice constant, *a*, as a variable, while *ucc* and ζ are treated as variables for phase-intermediate SLs (see the details in *Determinations of ζ values and lattice constants for* phase-intermediate *NC SLs*). Starting with estimated initial values for these variables, the sum of squares of the differences between calculated and measured d-spacing values was minimized through global optimization. Typically, more than 10 peaks were used to perform the least-squares fitting and determine the lattice constants.

Upon assignments of lattice constants**,** the structural factors were determined using the powder diffraction function in *CrystalMaker* (CrystalMaker Software Limited). A Lorentzian function was employed for the peak profile, with the peak width adjusted to match the experimental data.

Discrete dipole approximation (DDA) for absorption spectra simulations for Ag-NCs

In DDA, the target particle is discretized into *N* polarizable cubes. (*55*) The optical properties of the particle are modeled by calculating the coupling among these *N* polarizable cubes and the incident light. The particle's shape is determined by the arrangement of these cubes, and its size can be adjusted by varying the number and dimensions of the cubes. In our simulations, the grid length of each cube was set to 0.125 nm.

Ag-NCs were modeled with three layers. The inner core was represented by bulk Ag, with its dielectric constant obtained from Johnson et al.'s work. (*56*) Preceding the ligand layer, a thin layer with a modified dielectric constant, resulting from the interaction between the ligand and Ag atom, was introduced with a thickness of 0.25 nm. The dielectric constant of this layer was obtained from a report by Peng et al. (*39*) Finally, an outer layer consisting of a 1 nm thick ligand with a refractive index of 1.46 was applied to the surface.

In our simulations, we initially constructed a perfect mecon with these three layers similar to the model shown in Fig. 1i. To increase the sphericity in the particle, we applied a cutting radius to remove the prominent corners of the mecon for those outside of the defined radius. We gradually

rounded the mecon by reducing the cutting radius from 5.5 nm to 5.0 nm, until the structure was truncated to a sphere. This process was repeated for the two outer layers, while their thicknesses remained constant at 0.25 nm and 1 nm, respectively. Throughout the rounding process, the volume of the particle was kept constant.

SL formation simulations

We simulated two distinct models of ligand-grafted Ag-NC to separately probe the effects of the Ag-NC shape and ligand–ligand repulsion on the formation and stability of the phase-intermediate structures. To examine the effects of particle shape, we considered a stiff interaction model where the particles interact solely through volume exclusion and whose assembly and phase behavior were therefore completely determined by the shape of the particles. To examine the effects of ligand-induced interparticle repulsion, we considered a hard-core plus soft interaction model, i.e., total potential model, where a soft repulsive region was added to the interparticle pair potential. Particles in both models were characterized by the sphericity, λ, which determines the set of points $\vec{r}^{(\lambda)}$ that define the particle shape.

The set of points $\vec{r}^{(0)}$ was constructed by first placing a point on each vertex and two points equally spaced along each edge of a mecon. Next, the hexagonal facets were filled in with a hexagonal grid of points, and the square facets were filled in with a square grid. $\vec{r}^{(1)}$ was constructed by "puffing out the facets" of the mecon; mathematically, by radially scaling $\vec{r}^{(0)}$ by $r_c/|r_0|$, where $r_c$ is the circumsphere radius of the mecon and $|r_0|$ is the length of the vectors in $\vec{r}^{(0)}$. $\vec{r}^{(\lambda)}$ was then the linear interpolation of $\vec{r}^{(0)}$ and $\vec{r}^{(1)}$. These points defined the vertices of the hard polyhedra in the hard particle model and served as the interaction centers in the soft interaction model (see below for model-specific details). Supplementary Text 2 shows a set of points with their convex hulls for different values of λ. We note that the density of interaction sites on the Ag-NC model is nonuniform (see figure in Supplementary Text 2), even when $\lambda = 1$. Since these points define the interaction sites in the soft interaction model (see below Figure), the total NC–NC interaction is always anisotropic. The density of interaction sites is lower on regions of the particle surface that correspond to the [100] directions of the Ag-FCC lattice, which in our model corresponds to a lower ligand density on the surface. We made this assumption in the absence of any experimental evidence to (in)validate it; however, the accuracy of the model's structural predictions (vide infra — new simulated WAED figure) demonstrates its validity.

All simulations were performed using the HOOMD-blue simulation engine (version 4.8), using HPMC for the stiff interaction model and HPMD for the total potential model. (*57, 58*) We leveraged the signac framework for data management, and managed the computational workflow with row (https://row.readthedocs.io/en/0.4.0/). The freud analysis toolkit was used to analyze the systems. (*59*)

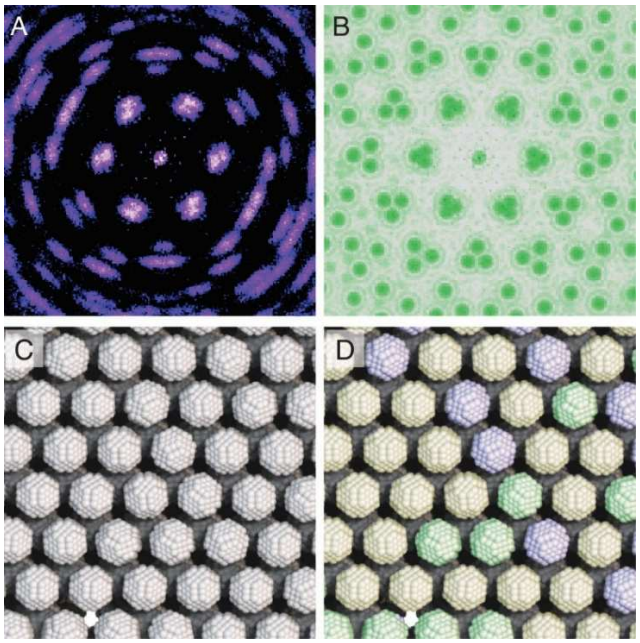


Caption | FCC SLs from spherical Ag-NCs from simulation (**A**) WAED patterns from MD-simulation generated FCC SLs from the $[111]_{\text{FCC-SL}}$ projection, (**B**) theoretical WAED patterns from the computer model, (**C**) snapshot of MD-simulation generated SLs from the $[111]_{\text{FCC-SL}}$ projection, and (**D**) same MD snapshot as (C) with coloring to denote domain orientations, as in Fig. S5 panel (D). The strong agreement between these results and Fig. S5 (A-D)—particularly between panels (A) and Fig. S5 (A)—demonstrates the high fidelity of the simulation in capturing the experimentally observed SL structure and orientation distribution. Note that the particles in (G) and (H) are depicted as discretized polyhedra, but the particles had $\lambda = 1.0$ in the simulation (i.e., sphere-shaped, see Supplementary Text 2).

*Stiff interaction model and simulations*

We investigated the role of shape assembly and stability of phase-intermediate structures by performing HPMC simulations of shapes across the shape family parameterized by λ. Here, the shape is defined as the convex hull of the points $\vec{r}^{(\lambda)}$. We conducted two distinct types of HPMC simulations of the stiff interaction model, differing in whether the particles were initialized in a completely disordered state or in a crystalline configuration. When initialized from BCC and FCC, we placed particles in a simple cubic lattice at 0.4 packing and then simulated at a constant volume for 1,000,000 HPMC steps to randomize their positions and orientations. These systems were then compressed to a packing fraction of 0.5 over 1,000,000 HPMC steps and then slowly compressed to the final packing fractions using an iterative scheme, allowing the simulation box to change shape during compression. In each of the 10 iterations, the system was first compressed to a target packing fraction, followed by 1,500,000 steps of HPMC with box shear and aspect ratio moves to allow the simulation cell to respond to shear and tensile stresses. Once the systems reached the final packing fractions (0.7), we ran for additional 75,000,000 HPMC steps, with the latter 25,000,000 used for structural analysis. All MC moves (particle position, orientation, and box moves) were tuned to achieve ~20% acceptance rate.

*Total potential model and simulations*

In addition to HP simulations, we implemented a model that includes a soft interparticle repulsion to account for ligand-ligand interactions between neighboring Ag-NCs. This model assumes the NCs are in a good solvent for the ligands, leading to steric repulsion between the ligand layers on neighboring particles. This steric repulsion effectively screens the van der Waals (vdW) interactions between the Ag-NC cores for the particles and ligands of interest here, as predicted by an analytical NC–NC interaction model that accounts for core–core vdW and ligand–ligand interactions (*60, 61*). This analytical model predicts a total interaction profile with a maximum attraction of ~1/2 $k_BT$, which we assume is negligible We considered two repulsive length scales in this model: the longer-range, softer repulsion between sites (2 nm < $r$ < 4 nm) represents the penalty associated with ligand layers on neighboring Ag-NCs interdigitating, while the second repulsive length scale ($r$ < 2 nm) represents the stronger, entropic/steric repulsion when compressing Ag-NCs once their ligand layers are fully interdigitated. The softer repulsion was implemented as a Gaussian-like potential:

$$u_{\text{soft}}(r_{ij}) = \varepsilon_G \exp\left(-\frac{r_{ij}^2}{2\sigma_G^2}\right) \quad \text{(Eq.7)}$$

where the magnitude $\varepsilon_G$ and characteristic range $\sigma_G$ were set such that $u_{\text{soft}}(2\text{ nm}) = 2\,kT$. We implemented the stronger repulsion as a Weeks–Chandler–Anderson (WCA) potential:

$$u_{\text{stiff}}(r_{ij}) = 4\varepsilon_{\text{WCA}}\left[\left(\frac{\sigma_{\text{WCA}}}{r_{ij}}\right)^{12} - \left(\frac{\sigma_{\text{WCA}}}{r_{ij}}\right)^{6}\right] + \varepsilon_{WCA} \quad \text{(Eq.8)}$$

$$u_{\text{stiff}}(r_{ij}) = \begin{cases} 4\varepsilon_{\text{WCA}}\left[\left(\frac{\sigma_{\text{WCA}}}{r_{ij}}\right)^{12} - \left(\frac{\sigma_{\text{WCA}}}{r_{ij}}\right)^{6}\right] + \varepsilon_{\text{WCA}}, & r_{ij} < 2\text{ nm} \\ 0, & x \geq 2\text{ nm} \end{cases} \quad \text{(Eq.9)}$$

where $\sigma_{\text{WCA}} = 2\ nm\ \times 2^{-\frac{1}{6}}$ such that the minimum of the corresponding Lennard–Jones potential was at 2 nm. The total pairwise inter-Ag-NC interaction was then computed as the sum:

$$u_{NC-NC} = \sum_{i,j} u_{ij,soft}(r_{ij}) + u_{ij,hard}(r_{ij}) \quad \text{(Eq.10)}$$

for all pairs of interaction sites $i$ and $j$ on the two Ag-NCs ($i$ and $j$ on *different* Ag-NCs). These interactions were implemented through rigid body constraints in HOOMD-blue, where the interaction sites constitute the points defining the rigid body. (*62*)

We initialized simulations of the soft interaction model with 1,000 Ag-NCs (393,000 total interaction sites) in simple cubic lattices at ~0.4 packing and then simulated a pressure ramp to mimic the evaporative assembly process. The systems evolved using the symplectic Martyna–Tobias–Klein integrator with a fully anisotropic Langevin piston barostat (i.e., all dimensions of

the simulation box independently coupled to the barostat) to allow for the relaxation of tensile and shear stresses in the simulation box. *(63)* We linearly increased the systems' pressure from 0.01 to 0.1 over the first $1 \times 10^7$ MD steps and collected system snapshots over the next $1 \times 10^7$ MD steps for analysis. For all MD simulations, we used a timestep $\delta t = 0.01\tau$, where $\tau$ is the natural time unit of the simulation, pressure coupling constant $\tau_s = 1000 \cdot \delta t$ and friction constant of the Langevin piston $\gamma = 2/\tau_s$.

*Orientational order diagrams analyses*

We characterized the structure of the systems using the rotationally invariant Steinhardt order parameter of order 10, $\bar{q}'_{10}$, where the bar denotes the neighbor-averaged version and the prime denotes the weighted version. (*64*) Neighbor lists were constructed via a Voronoi decomposition of the particle centroids. Ag-NCs were considered neighbors if their respective Voronoi cells shared a common plane, and the area of the plane was used as the weight for calculating, $\bar{q}'_{10}$. Reported values are the averages over all particles and all simulation frames used for analysis. To quantitatively compare experimental and simulation results, the Steinhardt order parameter values were normalized and converted to ϒ. See Fig. S28.

To further quantify order in the system, we computed two distinct orientational order diagrams. The standard BOODs mapped each particle's nearest neighbor vectors onto the unit sphere, generating a distribution of nearest globally referenced neighbor directions. Additionally, we computed FOODs, constructed similarly to BOODs, except that they used the distribution of facet normal vector directions. The correlation of the system BOOD and FOOD describes the correlation between the lattice vectors of the Ag-NC SL and the lattice planes of the Ag-NCs.

Structural factors were constructed by projecting the particle positions into the viewing plane and taking the FFT of the resulting point pattern. These patterns did not directly contain information related to the shapes of the particles. All analyses were performed using the freud analysis toolkit.(*59*)

Finite-Difference Time-Domain (FDTD) simulations for plasmonics of Ag-NC SLs

To simulate the optical response of Ag-NCs and their SLs, the FDTD method was employed as implemented in Lumerical FDTD Solutions. This method discretizes space and time into cubic cells and solves Maxwell's equations iteratively. (*65*) For the simulations, we used the Ag dielectric function measured by Yang et al. (*66*) and a dielectric constant of 1.4 for the surrounding medium to mimic the ligand molecules. We employed a mesh-override region covering the full structure with a mesh size of 0.05 nm for single particles and 0.1~0.2 nm for the SLs. Slabs of Ag-NC SLs for FDTD simulations were constructed to replicate experimentally-obtained NC SLs (i.e., the SL structures and lattice constants), with some adjustments of the particle size and the gap distance to match optical properties from the experiment and simulation. Specifically, slabs of FCC SLs with a lattice constant 17.75 nm were constructed from spherical Ag-NCs with a diameter d = 11.25 nm. The gap distance was calculated as 1.3 nm. In the simulation box, the $[111]_{SL\text{-}FCC}$ direction was designated as the *z*-axis. Slabs of BCC SLs were constructed using mecon Ag-NCs with an identical volume to that of the spherical Ag-NCs. The lattice constant was set to 14.12 nm, ensuring the same interparticle distance as in the FCC SLs. In the simulation box, the $[110]_{SL\text{-}BCC}$ was designated as the *z*-axis. Electromagnetic simulations for phase-intermediate SLs composed of Ag-

NCs with a sphericity parameter λ = 0.56 were conducted using a simplified structural model, generated by scaling the BCC unit cell to match the relevant size. It should be noted that the actual phase-intermediate SLs are too complicated to reproduce in simulation slab due to their symmetry-breaking, base-centered monoclinic structure. Unlike BCC and FCC SLs whose substrate-parallel planes ($(110)_{SL\text{-}BCC}$ and $(111)_{SL\text{-}FCC}$) correspond to well-defined wavevectors (ΓN and ΓL) in the Brillouin zone, phase-intermediate SLs lack a periodic pathway between common critical points normal to the substrate, preventing direct and precise simulation of the optical properties of the SL along the lattice stacking direction. This approach, while not capturing the full structural complexity of the N-W phase-intermediate SL, reproduced the experimental spectra with excellent agreement. For tight BCC SLs, the gap distance was further reduced to 0.5 nm, increasing the space-filling factor to 84.5%. We reduced the structure to a single unit cell perpendicular to the *z*-axis and applied periodic boundary conditions along the *x*- and *y*-axes. In the simulation box, the slabs were illuminated by broadband plane electromagnetic waves propagating along the *z*-axis direction and polarized along the *x*-axis direction. We confirmed that the polarization direction in the *xy*-plane did not affect the calculated far-field spectra. 2D frequency-domain power monitors were used to record simulated transmission, *T,* and reflection spectra, *R*. The absorption spectra, *A,* were then obtained using the relation $A = 1 - T - R$.

To extract the plasmon-polariton dispersion from the FDTD simulations, the simulated absorption spectra were used to determine the frequency and wavelength of polariton standing waves across a SL slab. The simulation spectra of FCC SLs from spherical Ag-NCs and BCC SLs from mecon Ag-NCs with ~ 48 SL layers were fitted with Lorentzian functions to determine the standing waves frequency. It should be noted that a large number of layers was necessary to collect sufficient data points, as the small NC size resulted in a relatively thin total slab thickness compared to the polariton wavelengths. The plasmon-polariton wavelength was derived from the open slab boundary conditions across the simulated slabs (see Ref. 33 for details). The extracted energies were plotted against the wavevector (Fig. 4H) and were fitted using Hopfield model for the lower polariton to obtain the collective transverse plasmon frequency, $\omega_t$, and the vacuum Rabi frequency, $\Omega_R$. The reduced coupling strength $\eta$ (the strength of light-matter coupling) was assessed with the ratio of the vacuum Rabi frequency and the collective transverse plasmon frequency, i.e., $\Omega_R/\omega_t$.(*33*) Additionally, FCC and BCC SLs of the intermediate rounded mecons were simulated; however, little difference was observed when compared to the ideal spherical and mecon structures.

**Supplementary Text 1: Geometrical characteristics of mecons, spheres, and their SLs**

This section discusses the geometrical characteristics of mecons, spheres, and their superstructures including the gap distances within the SLs, the projected area corresponding to TEM images, NC volume, and NC density within the SLs.

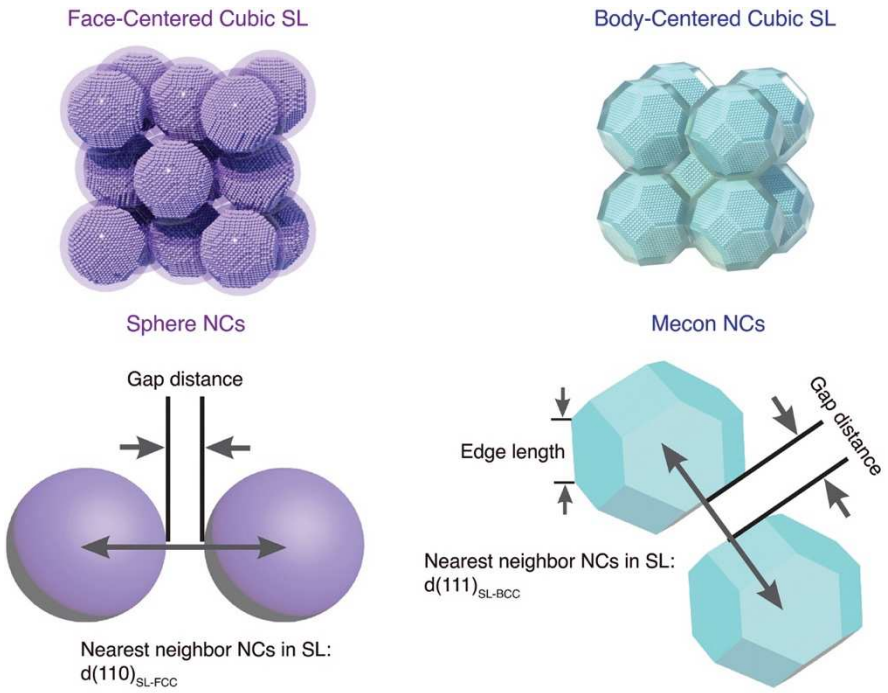


Caption | Computer models of FCC SL, BCC SL, and two nearest neighbor NCs

Spheres and FCC SLs

Volume of a spherical object can be calculated as:

$$\mathbf{V_{sphere}} = 4/3\ \pi \times (\mathbf{D_{sphere}}/2)^3$$

where $\mathbf{V_{sphere}}$ and $\mathbf{D_{sphere}}$ are the volume and diameter of a sphere, respectively.

For spheres, the gap distance is defined as the point-to-point distance between two nearest neighbor particles, as illustrated above. In FCC SLs, the nearest neighbor distance (i.e., the center-to-center distance) is $d(110)_{SL\text{-}FCC}$, thus the gap distance can be calculated as:

$$\textbf{Gap distance} = \mathbf{d(110)_{SL\text{-}FCC}} - \mathbf{D_{sphere}}$$

The projection of a sphere, as appeared in TEM images, is presented as a circle, with an area given by:

$$\textbf{Area of projected sphere} = \pi \times (\mathbf{D_{sphere}}/2)^2$$

*Example: 10.0 nm sphere in an FCC SL with the lattice constant ($a_{SL\text{-}FCC}$) of 17.75 nm*

**Volume of the sphere ($V_{sphere}$):**

$$\mathbf{V_{sphere}} = 4/3\ \pi \times (10.0\ /2)^3 = \mathbf{523.5\ nm^3}$$

**Gap distance**:

The center-to-center distance between the nearest neighbors in the FCC SL is:

$$\mathbf{d(110)_{SL-FCC}} = \boldsymbol{a}_{\mathbf{SL\text{-}FCC}} \times \sqrt{2}\ /\ 2 = 12.55\ \text{nm}$$

The gap distance is then:

Gap distance: 12.55 nm - 10.0 nm = **2.55 nm**

**NC density:**

The NC density in the SL is calculated using:

Volume of NC core × Number of NCs per SL unit cell / Volume of SL unit cell.

This results in an NC density of **35.4%**.

**Projected area calculation:**

With a diameter of 10.0nm,

**Area of projected sphere** = $\pi \times (10/2)^2 = \mathbf{78.54nm^2}$

<u>Mecons and BCC SLs</u>

The volume of a mecon is given by:

$$\mathbf{V_{mecon}} = 8\sqrt{2} \times \mathbf{edge\ length}^3$$

where $\mathbf{V_{mecon}}$ is the volume of a mecon. A perfect mecon has a uniform edge length.

For mecon-shaped NCs forming a BCC SLs, the gap distance is determined by the plane-to-plane separation as illustrated in the figure shown in page 11. We used the Wigner-Seitz (WS) cell to calculate the gap distance in the BCC SL. Because a mecon can serve as the WS cell of a BCC, the gap distance is expressed as:

**Gap distance**
= $\mathbf{d(111)_{SL\text{-}BCC}}$ - width of mecon in d(111) direction
= $\mathbf{d(111)_{SL\text{-}BCC}}$ (1 - $\mathbf{V^{1/3}}_{\mathbf{WS\text{-}BCC}}$ / $\mathbf{V^{1/3}}_{\mathbf{mecon}}$)

where $\mathbf{V_{WS\text{-}BCC}}$ is the volume of the WS cell for the BCC SLs. It is noted that $\mathbf{d(111)_{SL\text{-}BCC}}$ is the nearest neighbor distance in BCC SLs.

Each BCC unit cell contains two mecon-WS cells, thus $V_{WS\text{-}BCC}$ can be calculated as:

**Unit cell volume of a BCC SL** = $\mathbf{V_{WS\text{-}BCC}} \times 2$

Following these calculations, the gap distance between neighboring mecons can be precisely obtained.

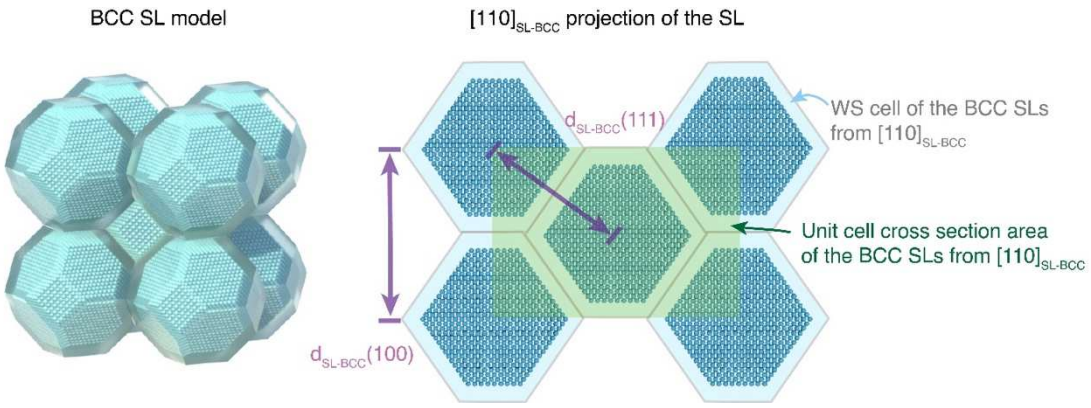


Caption | BCC SLs from mecons and the cross-section for the $(110)_{SL\text{-}BCC}$ plane

**Projected area of the mecon**: Calculating the projected area of a mecon needs careful considerations due to the anisotropic geometric characteristic of the mecon shape. For example, the projected area along the $[110]_{Ag\text{-}FCC}$ projection of a mecon can be calculated based on the following equations. Since the $[110]_{Ag\text{-}FCC}$ projection aligns with the $[110]_{SL\text{-}BCC}$ direction, the projection of WS cell in the BCC lattice along the $[110]_{SL\text{-}BCC}$ direction can be expressed as tiling of elongated hexagons as presented above. The projected area of the BCC SLs from $[110]_{SL\text{-}BCC}$ direction, $\mathbf{A_{WS\text{-}BCC[110]}}$, contains two elongated hexagons (purple box area in the above right panel), thus the area can be calculated by:

$$\mathbf{A_{WS\text{-}BCC[110]}} = \mathbf{d(100)_{SL\text{-}BCC}} \times 2\ \mathbf{d(110)_{SL\text{-}BCC}}\ \mathbf{/2}$$

A projected area of a mecon from $[110]_{Ag\text{-}FCC}$ projection, $\mathbf{A_{Ag\text{-}mecon[110]}}$, can be calculated from $\mathbf{A_{WS\text{-}BCC[110]}}$, $\mathbf{V_{WS\text{-}BCC}}$ and $\mathbf{V_{mecon}}$ using the equation below:

$$\mathbf{V^{1/3}}_{\mathbf{WS\text{-}BCC}} / \mathbf{V^{1/3}}_{\mathbf{mecon}} = \mathbf{A^{1/2}}_{\mathbf{WS\text{-}BCC[110]}} / \mathbf{A^{1/2}}_{\mathbf{Ag\text{-}mecon[110]}}$$

*Example: Mecons with an edge length of 3.59 nm in a BCC SL with a lattice constant ($a_{BCC}$) of 14.12 nm*

**Volume of the mecon**:

$$\mathbf{V_{mecon}} = 8\sqrt{2} \times (3.59\ \text{nm})^3 = \mathbf{523.5\ nm^3}$$

**Gap distance**:

$$= d(111)_{SL\text{-}BCC} \times (1 - V^{1/3}{}_{WS\text{-}BCC} / V^{1/3}{}_{mecon})$$
$$= 12.23\ \text{nm} \times (1 - (1416.3/523.5)^{1/3})$$
$$\mathbf{= 3.45\ nm}$$

Following the same procedure, the gap distance along $[100]_{SL\text{-}BCC}$ direction can be calculated to be 3.99 nm.

**NC density:**

$\mathbf{V_{mecon}} \times 2$ / Volume of SL unit cell.

This results in an NC density of **37.2%**.

**Projected area calculation of a mecon from $[110]_{Ag\text{-}FCC}$, $A_{Ag\text{-}mecon[110]}$:**

$$\mathbf{A_{WS\text{-}BCC[110]}} = \mathbf{d(100)_{SL\text{-}BCC}} \times 2\ \mathbf{d(110)_{SL\text{-}BCC}}\ \mathbf{/2}$$
$$= 14.12 \times 9.99$$
$$= 140.98\ \text{nm}^2$$

Thus,

$$\mathbf{A_{Ag\text{-}mecon[110]}} = (\mathbf{A^{1/2}_{WS\text{-}BCC[110]}} \times \mathbf{V^{1/3}}_{\mathbf{mecon}} / \mathbf{V^{1/3}}_{\mathbf{WS\text{-}BCC}})^2$$
$$= (140.98^{1/2} \times 523.5^{1/3} / 1416.3^{1/3})^2$$
$$= 72.91\ \text{nm}^2$$

Takeaways

In this section, we compared a mecon and a sphere with an identical volume (523.5 nm³) and evaluated their self-assembled SLs using parameters obtained from experiments. This resulted in comparable NC densities between the FCC and BCC SLs (35.4% vs. 37.2%). However, the projected areas of the mecon and sphere differed notably (78.54 nm² vs. 72.91 nm²). Moreover, while the gap distance values are different (2.55 nm vs. 3.45 nm), it is particularly important to note that the gap distance needs to be defined specifically for each structure. This distinction highlights the need for careful consideration when comparing structural parameters derived from experimental results.

**Supplementary Text 2: Sphericity of Ag-NCs**

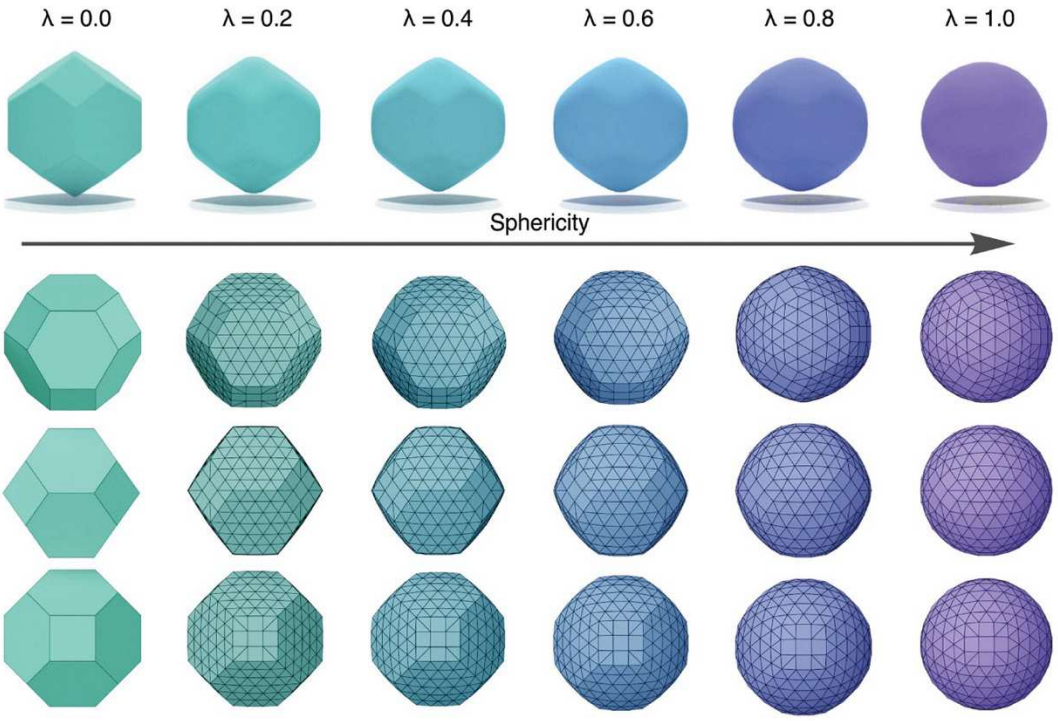


Caption ı Models of a perfect mecon, intermediate shapes with different sphericity values, and a perfect sphere

To characterize the shape of the Ag-NCs used in this study, we defined a sphericity parameter, **λ**, based on the distance from the center to the mesh points of the surface, $r_{i,\lambda}$. Here, $r_{i,\lambda}$ represents the position of the mesh point **i** for a given **λ**, where **λ** = 0 is a perfect mecon, and **λ** = 1 is a perfect sphere. Given **R** as the circumradius of these objects (i.e., radius of a reference sphere) and $\mathbf{r_{i,0}}$ as the positions of the mesh points of the reference mecon, shapes with $0 < \lambda < 1$ can be defined through linear interpolation between the sphere and the mecon, expressed as:

$$\mathbf{r_{i,\lambda}} = (1 - \boldsymbol{\lambda}) \times \mathbf{r_{i,0}} + \boldsymbol{\lambda}\mathbf{R}$$

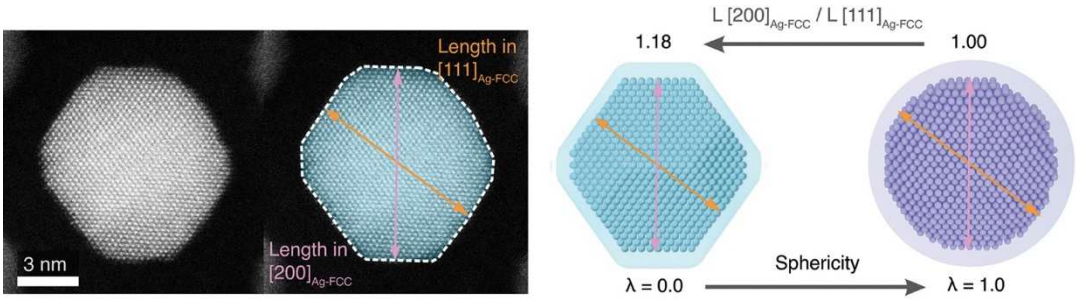


Caption ı HR-TEM images of Ag-NCs and the sphericity value

In the experiments, sphericity was defined based on the anisotropic characteristics of the mecon shape, as observed from the $[110]_{Ag\text{-}FCC}$ direction. Specifically, we analyzed HR-TEM images of Ag-NCs in the $[110]_{Ag\text{-}FCC}$ projection, measuring the lengths along the $[111]_{Ag\text{-}FCC}$ and $[200]_{Ag\text{-}FCC}$ directions, i.e., $L[111)_{Ag\text{-}FCC}$ and $L[200]_{Ag\text{-}FCC}$. The sphericity parameter was quantified using the length ratio, $L[200]_{Ag\text{-}FCC}$ / $L[111]_{Ag\text{-}FCC}$. For a perfect sphere ($\boldsymbol{\lambda} = 1$) and a perfect mecon ($\boldsymbol{\lambda} = 0$), the ratios of $L[200]_{Ag\text{-}FCC}$ / $L[111]_{Ag\text{-}FCC}$ take values of 1.00 and 1.18, respectively. For intermediate shapes, $0 < \boldsymbol{\lambda} < 1$, we applied linear interpolation between these two values, then obtained the value of $\boldsymbol{\lambda}$. To ensure statistical robustness, at least 25 images were analyzed for each sample of interest. We confirmed that the $\boldsymbol{\lambda}$ values determined from this experimental approach closely matched those derived from the computationally-parameterized models as the ones shown in the previous page, with deviations within a 5.0% error range. This consistency allowed for a direct comparison between the computational models and the experimentally observed samples in our study.

**Supplementary Text 3: Four martensitic transformation pathways**

In this section, four major martensitic pathways between a BCC and an FCC, i.e. Bain, Pitsch, Kurdjumov-Sachs (K-S), and Nishiyama-Wassermann (N-W) transformation pathways are explained in detail. Specifically, we list shared planes and directions through each pathway, graphical explanations of each pathway, and NC SL models delineating the martensitic transformation.

Shared planes and directions

**Bain:** Shared planes: $(001)_{FCC}$ // $(001)_{BCC}$ , $(110)_{FCC}$ // $(010)_{BCC}$ , $(1\bar{1}0)_{FCC}$ // $(100)_{BCC}$
Shared directions: $[110]_{FCC}$ // $[100]_{BCC}$

**Pitsch:** Shared planes: $(\bar{1}0\bar{1})_{FCC}$ // $(\bar{1}\bar{1}\bar{2})_{BCC}$ , $(100)_{FCC}$ // $(1\bar{1}0)_{BCC}$
Shared directions: $[010]_{FCC}$ // $[\bar{1}\bar{1}0]_{BCC}$, $[10\bar{1}]_{FCC}$ // $[1\bar{1}\bar{1}]_{BCC}$, $[001]_{FCC}$ // $[001]_{BCC}$

**K-S:** Shared planes: $(111)_{FCC}$ // $(110)_{BCC}$
Shared directions: $[\bar{1}10]_{FCC}$ // $[\bar{1}11]_{BCC}$

**N-W:** Shared planes: $(111)_{FCC}$ // $(011)_{BCC}$
Shared directions: $[1\bar{1}0]_{FCC}$ // $[100]_{BCC}$, $[\bar{1}\bar{1}2]_{FCC}$ // $[0\bar{1}1]_{BCC}$

Graphical explanations of Bain, Pitsch, N-W, and K-S transformations

(i) Bain transformation

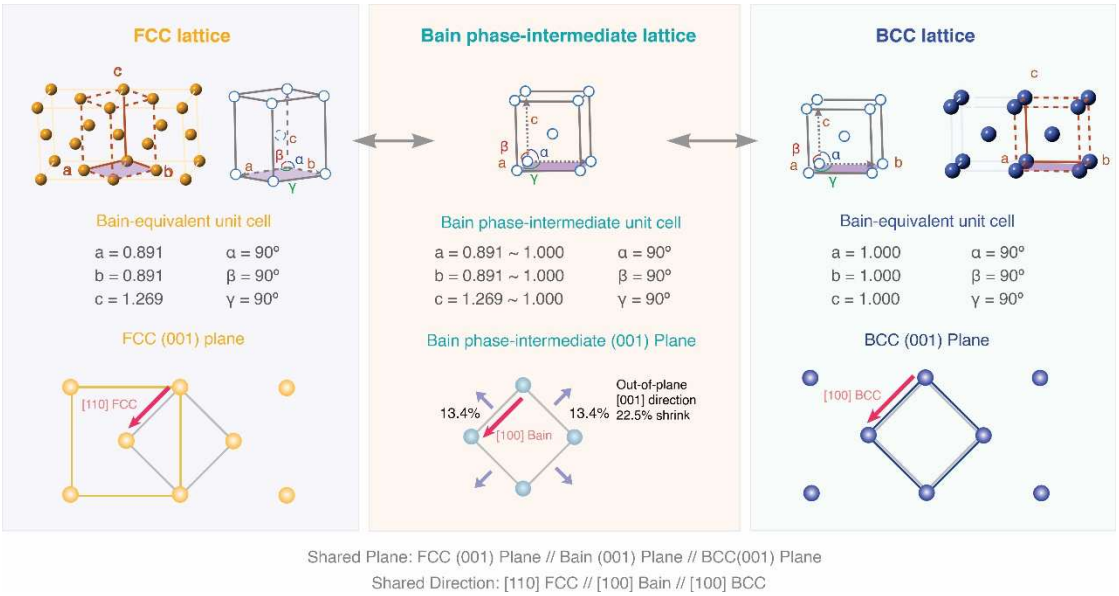


Caption ı Schematics of the Bain transformation pathway

The schematics describe the Bain transformation pathway from an FCC (left, yellow model), to a phase-intermediate (center, pale blue model), to a BCC (right, blue model) structure. The representative shared planes along the Bain transformation pathway are $(001)_{FCC}$ // $(001)_{BCC}$, illustrated with purple planes in the top models. The representative shared directions are $[110]_{FCC}$ // $[100]_{BCC}$, highlighted with red arrows in the bottom models.

The Bain phase-intermediate unit cell can be represented by a body-centered tetragonal structure. Using the unit cell, the lattice constants presented in the top right panel result in equivalent structures to an FCC and a BCC. Given $\mathbf{\tau}$ and ***ucc*** (unit cell constant, which is applied to normalize ***a***, ***b***, ***c*** unit cell parameters) values, the lattice constants, ***a***, ***b***, ***c***, $\alpha$, $\beta$, and $\gamma$ are expressed as follows:

$\boldsymbol{a}/\boldsymbol{ucc} = 0.890897 + \mathbf{\tau} \times 0.109103$
$\boldsymbol{b}/\boldsymbol{ucc} = 0.890897 + \mathbf{\tau} \times 0.109103$
$\boldsymbol{c}/\boldsymbol{ucc} = 1.259921 - \mathbf{\tau} \times 0.259921$
$\alpha = 90^{o}$
$\beta = 90^{o}$
$\gamma = 90^{o}$
Position: (0, 0, 0), (0.5, 0.5, 0.5)

(ii) Pitsch transformation

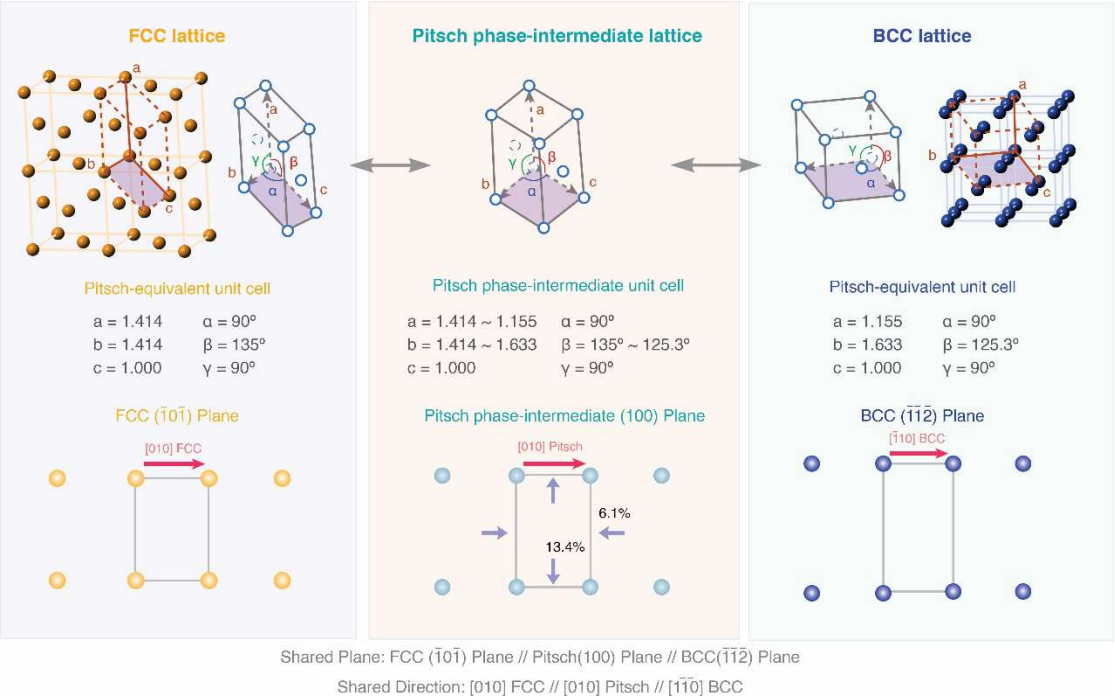


Caption | Schematics of the Pitsch transformation pathway

The schematics describe the Pitsch transformation pathway from an FCC (left, yellow models), to a phase-intermediate (center, pale blue models), to a BCC (right, blue models) structure. The representative shared planes along the Pitsch transformation pathway are $(\bar{1}0\bar{1})_{FCC}$ // $(\bar{1}\bar{1}2)_{BCC}$, illustrated with purple planes in the top models. The representative shared directions are $[010]_{FCC}$ // $[\bar{1}\bar{1}0]_{BCC}$, highlighted with red arrows in the bottom models.
The Pitsch phase-intermediate unit cell can be represented by a base-centered monoclinic structure. Using the unit cell, the lattice constants presented in the top left and right give equivalent structures to an FCC and a BCC, respectively. Given $\tau$ and ***ucc*** values, the lattice constants, ***a***, ***b***, ***c***, $\alpha$, $\beta$, and $\gamma$ are expressed as follows:

$$\boldsymbol{a}/\boldsymbol{ucc} = 1.41421 - \tau \times 0.25951$$
$$\boldsymbol{b}/\boldsymbol{ucc} = 1.41421 + \tau \times 0.21878$$
$$\boldsymbol{c}/\boldsymbol{ucc} = 1.00000$$
$$\alpha = 90^{\circ}$$
$$\beta = 135^{\circ} - \tau \times 9.736^{\circ}$$
$$\gamma = 90^{\circ}$$

Position: (0, 0, 0), (0.5, 0.5, 0)

(iii) Kurdjumov-Sachs (K-S) transformation

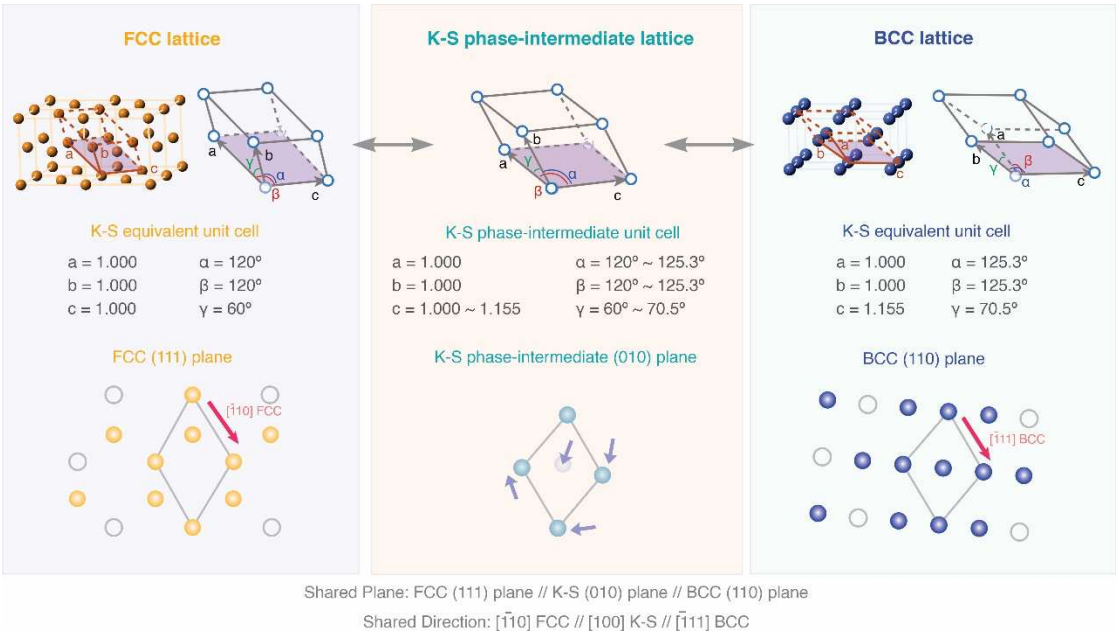


Caption | Schematics of the Kurdjumov-Sachs transformation pathway

The schematics describe the K-S transformation pathway from an FCC (left, yellow models), to a phase-intermediate (center, pale blue models), to a BCC (right, blue models) structure. The representative shared planes along the K-S transformation pathway are $(111)_{FCC}$ // $(110)_{BCC}$, illustrated with purple planes in the top models. The representative shared directions are $[\bar{1}10]_{FCC}$ // $[\bar{1}11]_{BCC}$, highlighted with red arrows in the bottom models.
The K-S phase-intermediate unit cell can be represented by a triclinic structure. Using the unit cell, the lattice constants presented in the top left and right give equivalent structures to an FCC and a BCC, respectively. Given $\mathbf{T}$ and ***ucc*** values, the lattice constants, ***a***, ***b***, ***c***, $\alpha$, $\beta$, and $\gamma$ are expressed as follows:

$\boldsymbol{a}/\boldsymbol{ucc} = 1.00000$
$\boldsymbol{b}/\boldsymbol{ucc} = 1.00000$
$\boldsymbol{c}/\boldsymbol{ucc} = 1.00000 + \mathbf{T} \times 0.1547$
$\alpha = 120^{o} + \mathbf{T} \times 5.264^{o}$
$\beta = 120^{o} + \mathbf{T} \times 5.264^{o}$
$\gamma = 60^{o} + \mathbf{T} \times 10.529^{o}$
Position: (0, 0, 0)

(iv) Nishiyama-Wassermann (N-W) transformation

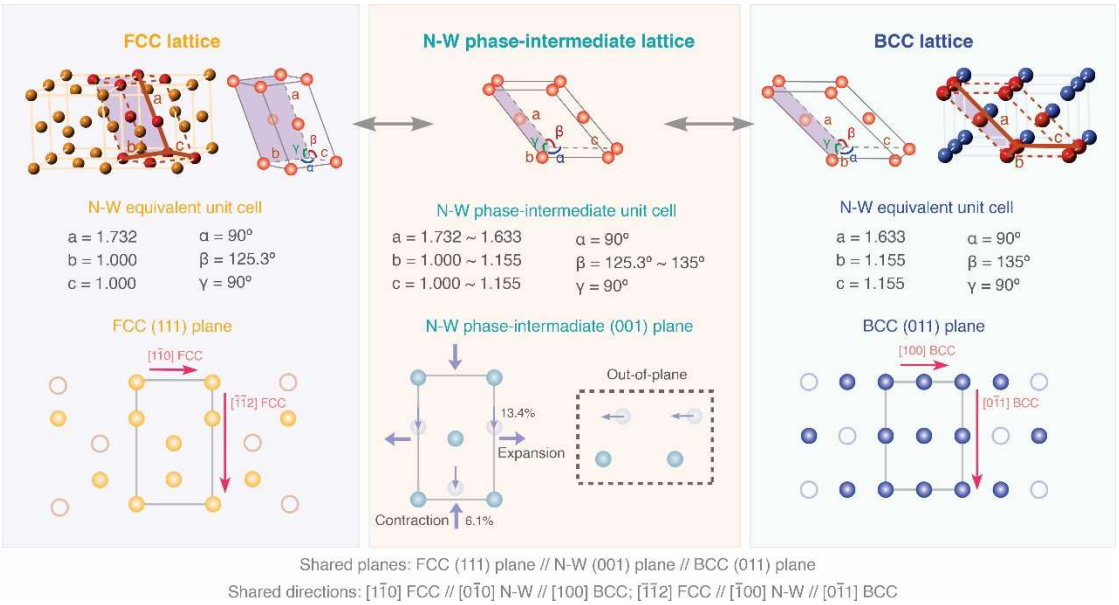


Caption ı Schematics of the Nishiyama-Wassermann transformation pathway

The schematics describe the N-W transformation pathway from an FCC (left, yellow models), to a phase-intermediate (center, pale blue models), to a BCC (right, blue models) structure. The representative shared planes along the N-W transformation pathway are $(111)_{FCC}$ // $(011)_{BCC}$, illustrated with purple planes in the top models. The representative shared directions are $[1\bar{1}0]_{FCC}$ // $[100]_{BCC}$ and $[\bar{1}\bar{1}2]_{FCC}$ // $[0\bar{1}1]_{BCC}$, highlighted with red arrows in the bottom models.
The N-W phase-intermediate unit cell can be represented by a base-centered monoclinic structure. Using the unit cell, the lattice constants presented in the top left and right give equivalent structures to an FCC and a BCC, respectively. Given $\mathbf{T}$ and ***ucc***, the lattice constants, ***a, b, c***, **α, β,** and **γ** are expressed as follows:

$\boldsymbol{a}/\boldsymbol{ucc} = 1.73205 - \mathbf{T} \times 0.09906$
$\boldsymbol{b}/\boldsymbol{ucc} = 1.00000 + \mathbf{T} \times 0.15470$
$\boldsymbol{c}/\boldsymbol{ucc} = 1.00000 + \mathbf{T} \times 0.15470$
$\boldsymbol{\alpha} = 90^{\circ}$
$\boldsymbol{\beta} = 125.265^{\circ} + \mathbf{T} \times 9.735^{\circ}$
$\boldsymbol{\gamma} = 90^{\circ}$
Position: (0, 0, 0), (0.5, 0.5, 0)

NC movements in the shared planes during the martensitic transformation

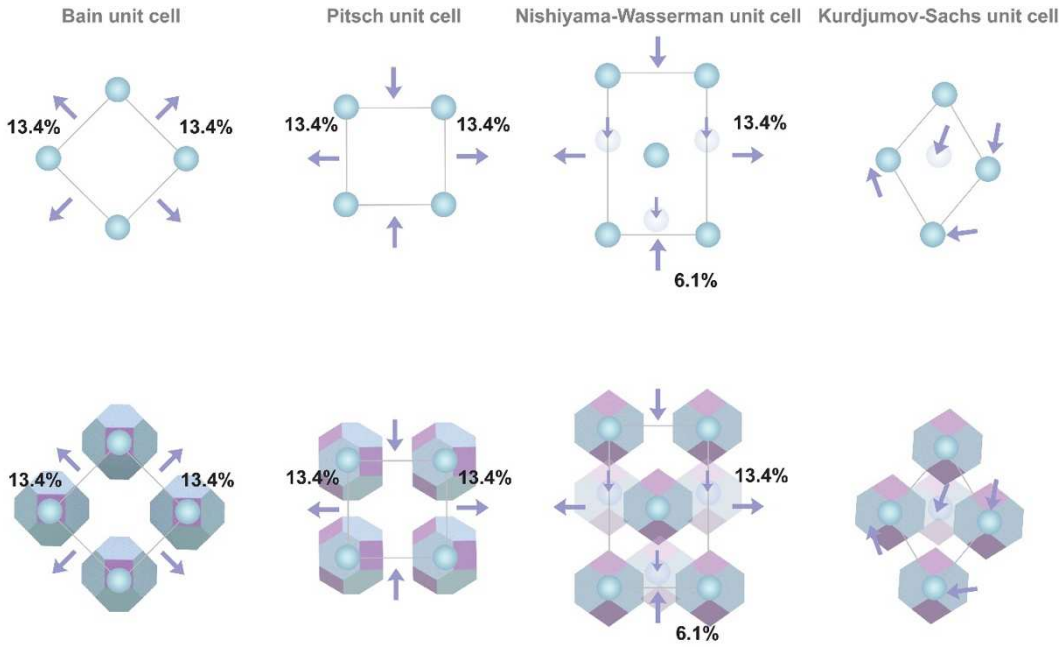


Caption | NCs in the shared planes during the martensitic transformation

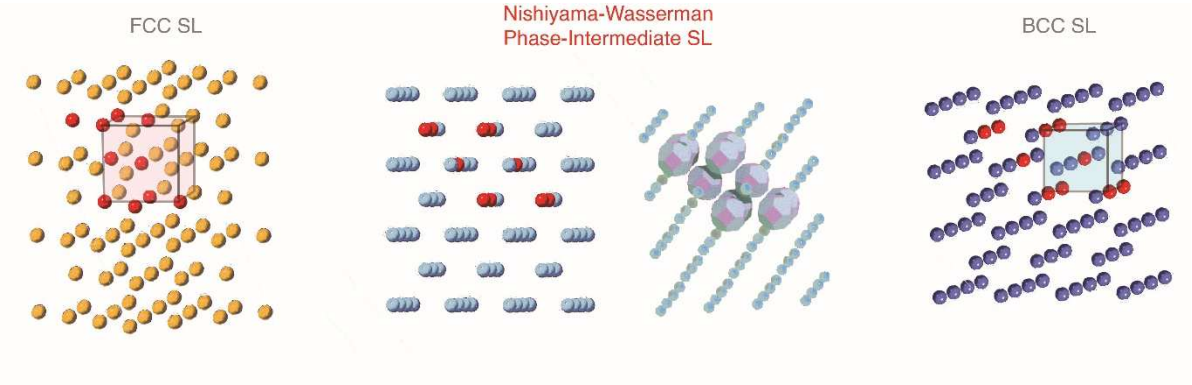


Caption | Nishiyama-Wassermann transformation pathway in expanded cells

Here, we extended the N-W transformation pathway beyond a single unit cell to describe the process in expanded cells. In the models, the 10 red balls represent those forming a N-W unit cell, while the blue balls represent atoms beyond that unit cell.

## Supplementary Figures and Tables

## Table S1 | Synthetic parameters of Ag-NCs used in this study.

| Silver NC Sample ID* | Mecon Ag [a] | Ag with λ = 0.62 [b] | Ag-III | Ag-IV | Ag-V | Ag-VI |
|---|---|---|---|---|---|---|
| **Size**** | 10.2 nm | 8.9 nm | 6.3 nm | 10.4 nm | 7.4 nm | 8.4 nm |
| **Sphericity (λ)** | 0.17 | 0.62 | 0.46 | 0.44 | 0.39 | 0.28 |
| **Ag-acetate** | 333 mg | 333 mg | 331 mg | 331 mg | 1656 mg | 331 mg |
| **$Cu(acetate)_2$** | 1.9 mg | 2.5 mg | 2.4 mg | 2.4 mg | 14 mg | 2.4 mg |
| **HCl** | 1 μL | 15 μL | 1 μL | 1 μL | 50 μL | 1 μL |
| **OAcid** | 1 mL | 2 mL | 2.5 mL | 1 mL | 10 mL | 1.5 mL |
| **OAm** | 1 mL | 2 mL | 2.5 mL | 1 mL | 10 mL | 1.5 mL |
| **DPE** | 12 mL | 10 mL | 9 mL | 12 mL | 50 mL | 11 mL |
| **Reaction Condition** | 180 ºC-5 min | 150 ºC-5 min | 180 ºC-5 min | 160 ºC-10 min | 150 ºC-5 min | 180 ºC-5 min |

| Silver NC Sample ID* | Ag-VII | Ag-VIII | Ag-IX | Ag-X | Ag-XI | Ag-XII |
|---|---|---|---|---|---|---|
| **Size**** | 5.5 nm | 10.4 nm | 7.1 nm | 7.5 nm | 7.6 nm | 6.4 nm |
| **Sphericity (λ)** | 0.89 | 0.28 | 0.33 | 0.45 | 0.72 | 0.56 |
| **Ag-acetate** | 331 mg | 331 mg | 331 mg | 666 mg | 331 mg | 331 mg |
| **$Cu(acetate)_2$** | 2.4 mg | 2.4 mg | 2.4 mg | 5.0 mg | 2.4 mg | 2.4 mg |
| **HCl** | 0.5 μL | 0.1 μL | 0.1 μL | 10 μL | 1 μL | 0.5 μL |
| **OAcid** | 7 mL | 1 mL | 2 mL | 5 mL | 1.5 mL | 2 mL |
| **OAm** | 7 mL | 1 mL | 2 mL | 5 mL | 1.5 mL | 2 mL |
| **DPE** | 0 mL | 12 mL | 10 mL | 18 mL | 11 mL | 10 mL |
| **Reaction Condition** | 160ºC-10min | 180ºC-5min | 185ºC-5min | 180 ºC-5 min | 180 ºC-5 min | 160 ºC-10 min |

[a] This sample was used for BCC SLs presented in Fig.1. [b] This sample was used for SLs presented in Fig. 2. * All NCs were used for SLs presented in Fig. 3E, F, and Table S8. ** The presented size is the average of measured length along [002] direction of the relevant sample.

## Table S2 | Results of annealing experiments.

| Ag NC Sample ID* | Mecon Ag NCs[a] | Ag-Annealed 1 | Ag-Annealed 2 | Ag-Annealed 3 | Spherical Ag NCs[b] |
|---|---|---|---|---|---|
| **Size**** | 10.2 nm | 10.1 nm | 10.0 nm | 10.0 nm | 10.0 nm |
| **Sphericity (λ)** | 0.17 | 0.39 | 0.56 | 0.83 | 0.95 |

[a] This sample was used for BCC SLs presented in Fig. 1. [b] This sample was used for FCC SLs presented in Fig. 1. * All NCs were used for SLs presented in Fig. 3, and Fig. S30. ** The presented size is the average of measured length along [002] direction of the relevant sample.

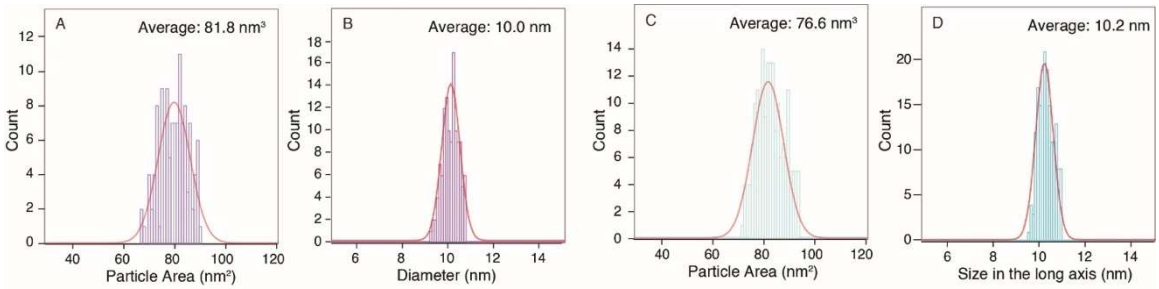


**Fig. S1. Analysis of TEM images of spherical and mecon Ag-NCs.** (**A**) Histogram of areas of the spherical Ag-NCs in the TEM image. (**B**) Histogram of the diameter of the spherical Ag-NCs. (**C**) Histogram of areas of the mecon Ag-NCs. (**D**) Histogram of the size in the long axis (i.e., $[002]_{Ag\text{-}FCC}$ direction) of the mecon Ag-NCs. The analyzed TEM images are shown in **main Fig. 1A, B, D, and E.** For detailed calculation and discussion on comparisons between spheres and mecons in TEM images, please see Supplementary Text 1.

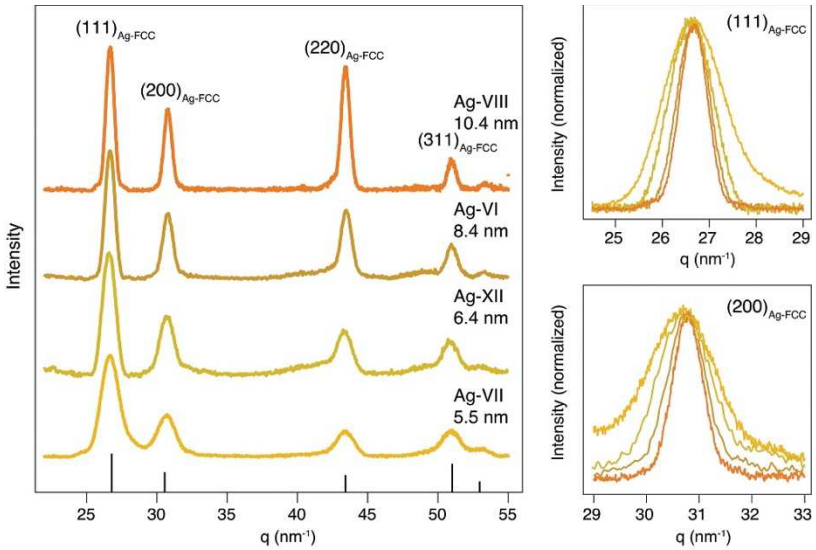


**Fig. S2. Powder XRD spectra of Ag-NCs.** XRD spectra of Ag-VII, Ag-XII, Ag-VI and Ag-VIII (left), and normalized and magnified peaks in the range of 25-29 $nm^{-1}$ (right top) and 29-33 $nm^{-1}$ (right bottom). The bars are the standard peak positions of the Ag-FCC atomic structure. Peak narrowing was observed with increase of the NC size. This trend follows the well-known Scherrer equation relationship, indicating the high crystallinity of the Ag-NCs used in this study.

**Table S3. Results of the XRD (Ag-VIII) shown in Fig. S2.**

| Peak number | 1 | 2 | 3 | 4 | 5 |
|---|---|---|---|---|---|
| Peak position (q/Å) | 2.662 | 3.074 | 4.336 | 5.088 | 5.333 |
| d-spacing (Å) | 2.360 | 2.044 | 1.449 | 1.235 | 1.178 |
| Peak assignment | Ag-FCC (111) | Ag-FCC (200) | Ag-FCC (220) | Ag-FCC (311) | Ag-FCC (222) |

The assigned unit cell is an FCC with ***a*** = 4.090 Å. The lattice constant, ***a***, is consistent with reported values of Ag crystals (e.g., 4.084Å from 10.1002/anie.201913704).

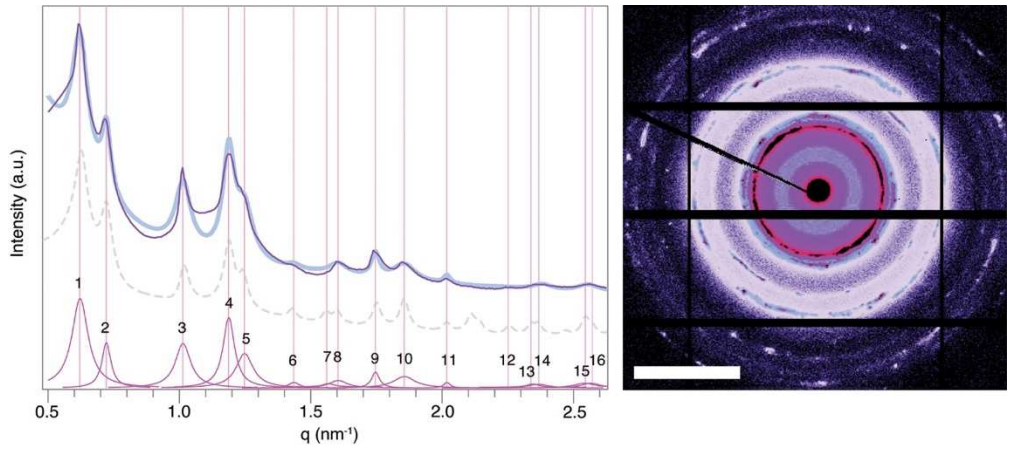


**Fig. S3. SAXS spectrum of FCC SLs from spherical Ag-NCs.** (left) SAXS spectrum of SLs from spherical Ag-NCs. The thick pale blue line, thin purple line, grey dashed line, and purple-red peaks represent the experimentally-obtained SAXS spectrum, the fitted spectrum, the simulated spectrum, and the constituent peaks used for fitting, respectively. (right) 2D SAXS pattern. The scale bar is 0.5 $nm^{-1}$.

**Table S4. Detailed results of SAXS spectrum presented in Fig. S3.**

| Peak number | **1** | **2** | **3** | **4** | **5** | **6** | **7** | **8** | **9** | **10** |
|---|---|---|---|---|---|---|---|---|---|---|
| Peak position (q/Å) | 0.0614 | 0.0711 | 0.0995 | 0.1180 | 0.1233 | 0.1420 | 0.1502 | 0.1550 | 0.1732 | 0.1841 |
| d-spacing (Å) | 102.38 | 88.35 | 63.15 | 53.25 | 50.94 | 44.25 | 41.84 | 40.54 | 36.27 | 34.13 |
| Peak assignment | FCC (111) | FCC (200) | FCC (220) | FCC (311) | FCC (222) | FCC (400) | FCC (330) | FCC (331) | FCC (422) | FCC (511) |
| Peak number | **11** | **12** | **13** | **14** | **15** | **16** | | | | |
| Peak position (q/Å) | 0.1984 | 0.2110 | 0.2239 | 0.2369 | 0.2510 | 0.2535 | | | | |
| d-spacing (Å) | 31.67 | 29.78 | 28.07 | 26.53 | 25.03 | 24.79 | | | | |
| Peak assignment | FCC (440) | FCC (600) | FCC (541) | FCC (622) | FCC (551) | FCC (640) | | | | |

The assigned unit cell is an FCC (Ƭ is 0%) with ***a*** = 17.75 (± 0.10) nm. Volume per one NC in the SL is 1398.1$nm^3$.

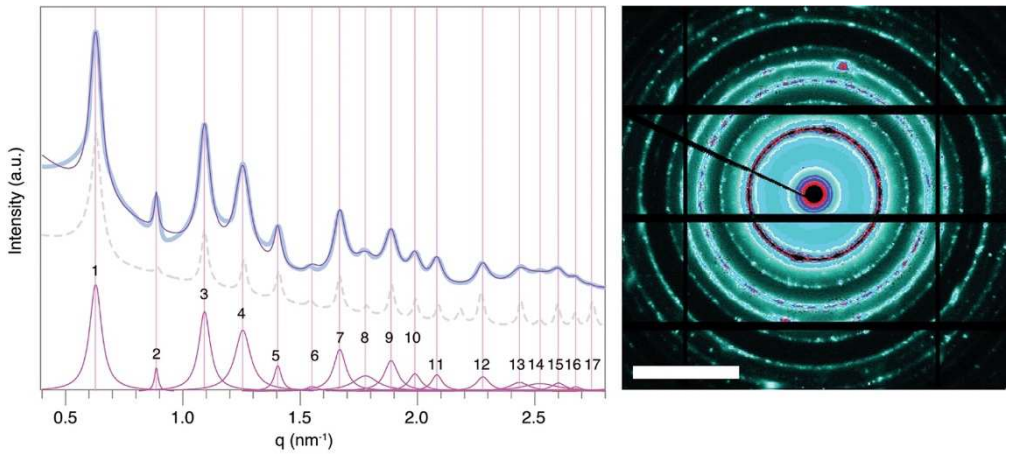


**Fig. S4. SAXS spectrum of BCC SLs from mecon Ag-NCs.** (left) SAXS spectrum of SLs from mecon Ag-NCs. The thick pale blue line, thin purple line, grey dashed line, and purple-red peaks represent the experimentally-obtained SAXS spectrum, the fitted spectrum, the simulated spectrum, and the constituent peaks used for fitting, respectively. (right) 2D SAXS pattern. The scale bar is 0.5 $nm^{-1}$.

**Table S5. Detailed results of SAXS spectrum presented in Fig. S4.**

| Peak number | 1 | 2 | 3 | 4 | 5 | 6 | 7 | 8 | 9 | 10 |
|---|---|---|---|---|---|---|---|---|---|---|
| Peak position (q/Å) | 0.0628 | 0.0886 | 0.1092 | 0.1255 | 0.1404 | 0.1550 | 0.1668 | 0.1778 | 0.1887 | 0.1988 |
| d-spacing (Å) | 100.06 | 70.89 | 57.54 | 50.07 | 44.75 | 40.53 | 37.67 | 35.35 | 33.30 | 31.60 |
| Peak assignment | BCC (110) | BCC (200) | BCC (211) | BCC (220) | BCC (310) | BCC (222) | BCC (321) | BCC (400) | BCC (330) | BCC (420) |
| **Peak number** | **11** | **12** | **13** | **14** | **15** | **16** | **17** | | | |
| Peak position (q/Å) | 0.2082 | 0.2278 | 0.2434 | 0.2522 | 0.2600 | 0.2674 | 0.2734 | | | |
| d-spacing (Å) | 30.18 | 27.58 | 25.81 | 24.91 | 24.17 | 23.50 | 22.98 | | | |
| Peak assignment | BCC (332) | BCC (510) | BCC (521) | BCC (440) | BCC (530) | BCC (600) | BCC (611) | | | |

The assigned unit cell is a BCC (ζ is 100%) with ***a*** = 14.12 (± 0.04) nm. Volume per one NC in the SL is 1416.3 $nm^3$.

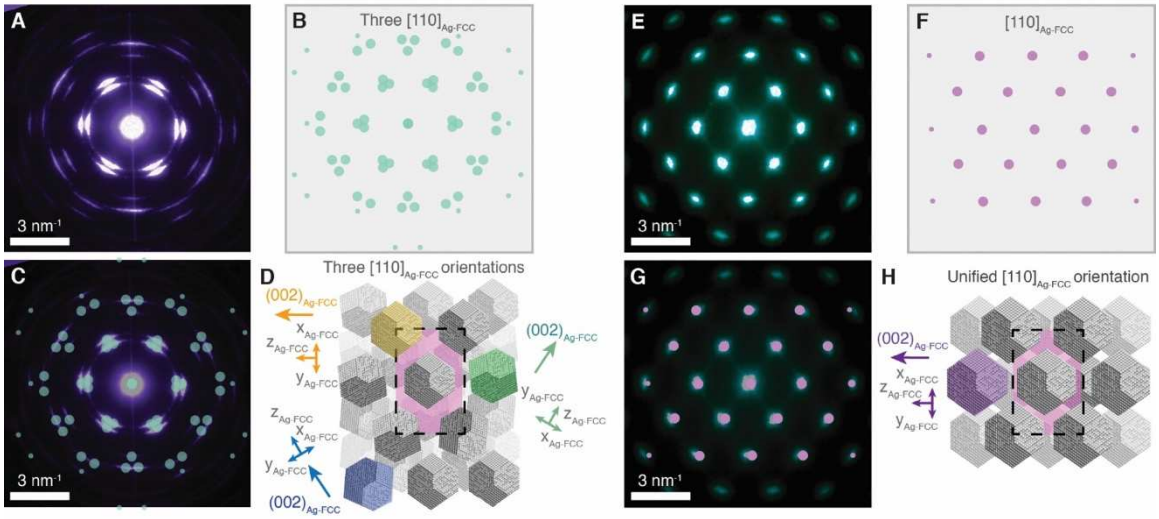


**Fig. S5. Selected-area WAED patterns for FCC SLs from spherical Ag-NCs and BCC SLs from mecon Ag-NCs.** (**A-D**) FCC SLs from spherical Ag-NCs and (**E-H**) BCC SLs from mecon Ag-NCs: experimental selected-area WAED patterns (**A, E**), simulated WAED patterns (**B, F**), overlapped presentation of the simulated and experimental WAED patterns (**C, G**), and computer models of the assigned structures (**D, H**). The simulated WAED pattern presented in panel **B** was synthesized with three sets of FCC patterns from the [110] projections with 0°, 120° and 240° angle offsets. In panel **D**, mecon models were used for presentation purposes to clearly show the facet orientation orders.

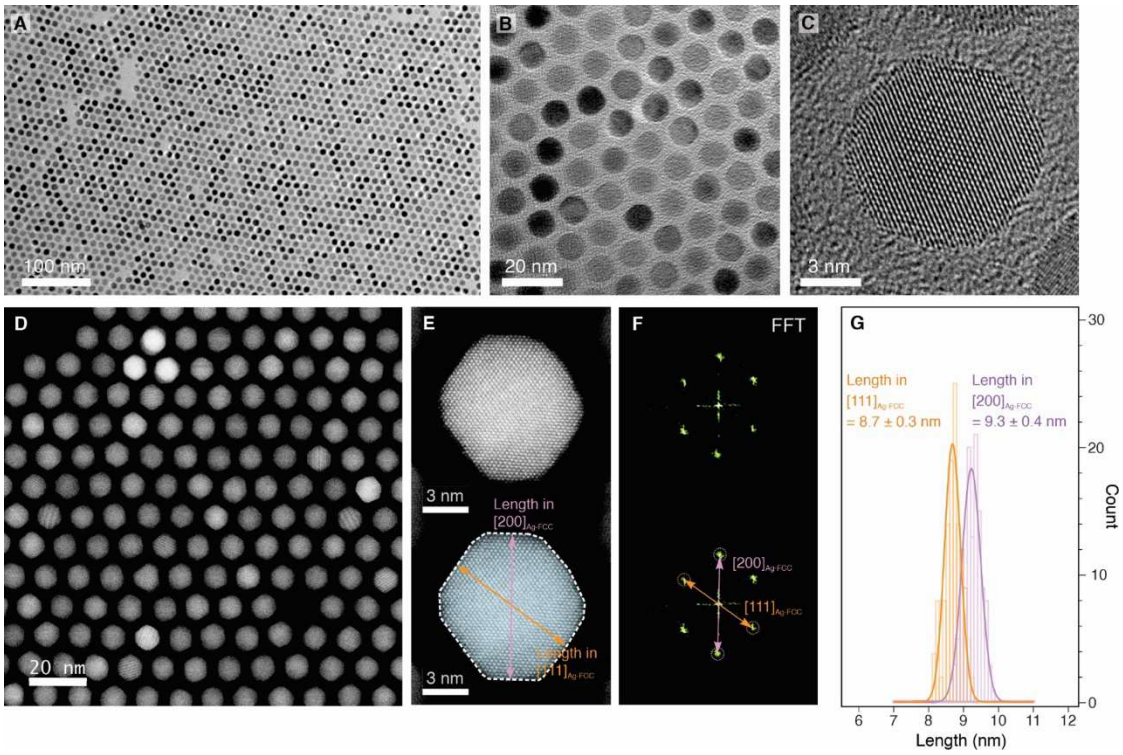


**Fig. S6. Ag-NCs with a λ of 0.62 used for the N-W phase-intermediate SLs presented in Fig. 2**. (**A-C)** TEM images with various magnifications. (**D**) STEM image. (**E)** HR-STEM images of an individual Ag-NC viewed along the $[110]_{Ag\text{-}FCC}$ projection. (**F**) The corresponding FFT patterns of the HR-STEM images. (**G**) Length distribution histograms of Ag-NCs in the $[200]_{Ag\text{-}FCC}$ (pink) and $[111]_{Ag\text{-}FCC}$ (orange) directions.

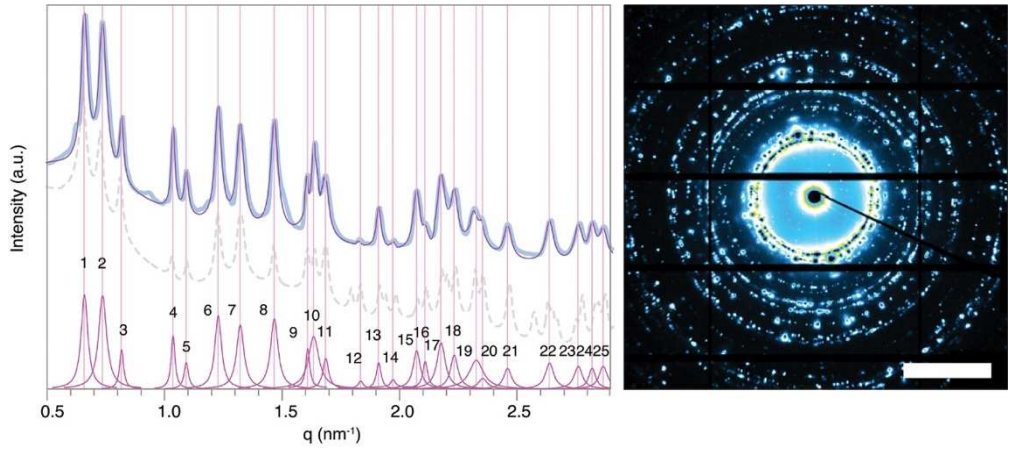


**Fig. S7. SAXS spectrum of SLs from Ag-NCs with λ = 0.62.** (left) SAXS spectrum of the Ag-NC SLs. The thick pale blue line, thin purple line, grey dashed line, and purple-red peaks represent the experimentally-obtained SAXS spectrum, the fitted spectrum, the simulated spectrum, and the constituent peaks used for fitting, respectively.(right) 2D SAXS pattern. The scale bar is 0.5 $nm^{-1}$.

**Table S6. Detailed results of SAXS spectrum presented in Fig. S7.**

| Peak number | **1** | **2** | **3** | **4** | **5** | **6** | **7** | **8** | **9** | **10** |
|---|---|---|---|---|---|---|---|---|---|---|
| Peak position (q/Å) | 0.0665 | 0.0735 | 0.0818 | 0.1035 | 0.1089 | 0.1227 | 0.1320 | 0.1463 | 0.1606 | 0.1636 |
| d-spacing (Å) | 94.44 | 85.49 | 76.80 | 60.72 | 57.70 | 51.22 | 47.59 | 42.94 | 39.12 | 38.42 |
| Peak number | **11** | **12** | **13** | **14** | **15** | **16** | **17** | **18** | **19** | **20** |
| Peak position (q/Å) | 0.1680 | 0.1828 | 0.1911 | 0.1970 | 0.2070 | 0.2108 | 0.2172 | 0.2236 | 0.2315 | 0.2345 |
| d-spacing (Å) | 37.40 | 34.38 | 32.87 | 31.89 | 30.35 | 29.80 | 28.93 | 28.10 | 27.14 | 26.80 |
| Peak number | **21** | **22** | **23** | **24** | **25** | | | | | |
| Peak position (q/Å) | 0.2458 | 0.2640 | 0.2763 | 0.2817 | 0.2871 | | | | | |
| d-spacing (Å) | 25.56 | 23.80 | 22.74 | 22.30 | 21.89 | | | | | |

The assigned unit cell is a base-centered monoclinic with the lattice constants of ***a*** = 19.58 nm, ***b*** = 12.13 nm, ***c*** = 12.13 nm, **α** = 90°, **β** = 128.6° and **γ** = 90°. **ζ** and **ucc** values are 33.8% and 11.53 nm, respectively. Volume per one NC in the SL is 1126.9 $nm^3$.

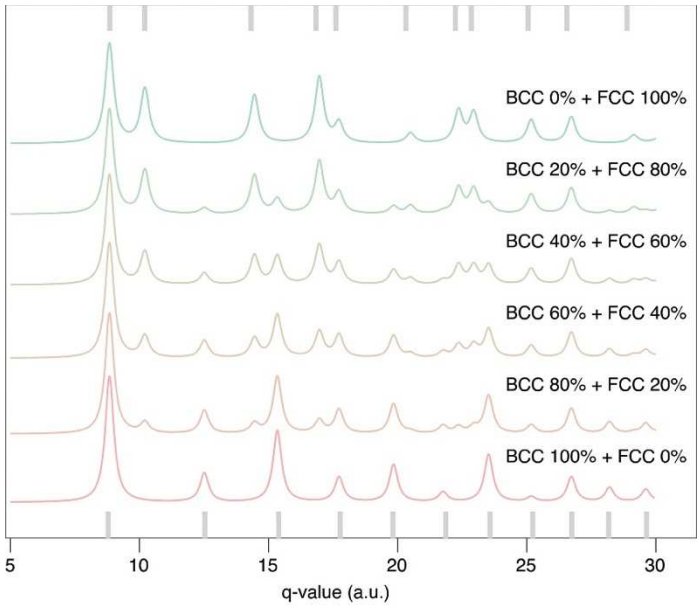


**Fig. S8. Simulated SAXS spectra containing BCC and FCC lattices with different ratios.** The bottom and top bars are the standard peak positions of BCC and FCC lattices, respectively.

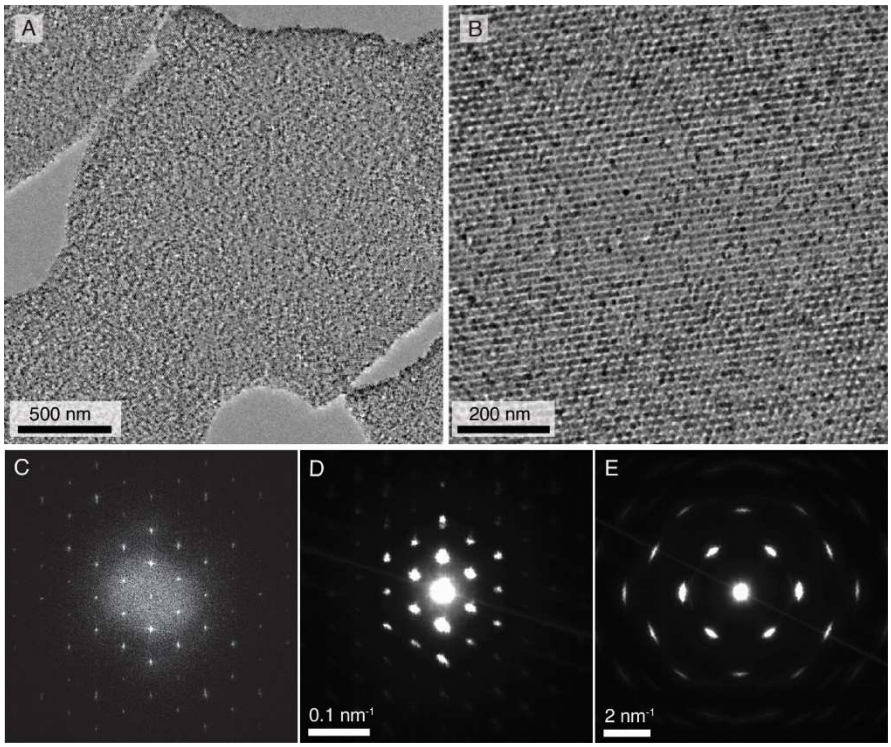


**Fig. S9. TEM measurements of NW phase-intermediate SLs from Ag-NCs with λ = 0.62.** (**A, B**) TEM images, (**C**) FFT pattern from the TEM image in (**B**), (**D**) small-angle and (**E**) wide angle ED patterns.

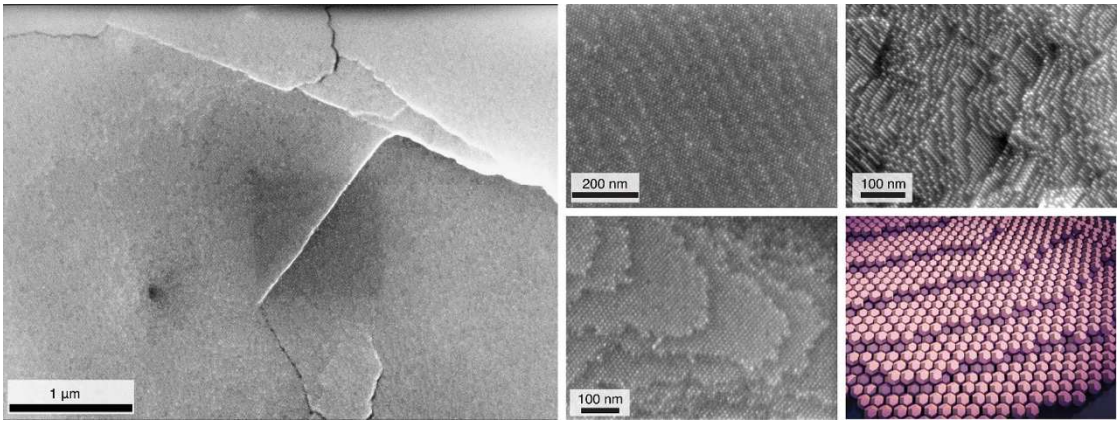


**Fig. S10. SEM images of NW phase-intermediate SLs from Ag-NCs with λ = 0.62 at different magnifications and the corresponding computer model.**

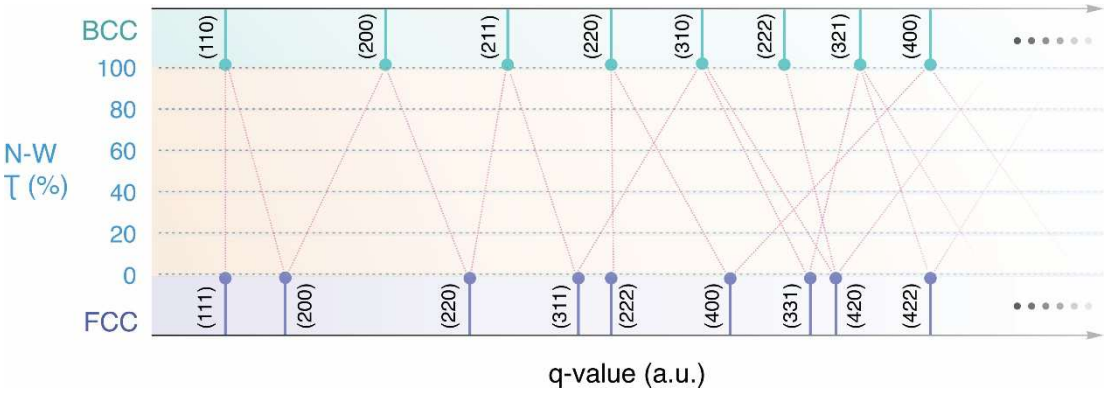


**Fig. S11. SAXS-peak evolution from a BCC (top) to an FCC (bottom) lattice through the N-W transformation pathway.** This figure presents a magnified view of the panel shown in **Fig. 2C** in the main text. Relative peak positions were adjusted to ensure that FCC and BCC SLs exhibit similar NC densities, consistent with our experimental observations. The SAXS evolution results can be analyzed by tracking individual peak movements in Movie S1.

**Table S7. Miller indices correlations of SAXS-peak evolution from an FCC to a BCC through the N-W transformation pathway.**

| **BCC** | (110) | | (200) | | (211) | | (220) | | (310) | | | (222) | | |
|---|---|---|---|---|---|---|---|---|---|---|---|---|---|---|
| **FCC** | (111) | (200) | (220) | (200) | (311) | (220) | (222) | (400) | (331) | (420) | (311) | (420) | | |
| **BCC** | (321) | | | (400) | | | (330) | | | | (420) | | | (332) |
| **FCC** | (422) | (333)<br>(511) | (331) | (440) | (400) | (531) | (333)<br>(511) | (600)<br>(442) | (420) | (600)<br>(442) | (620) | (422) | (620) | (531) |

The SAXS evolution results can be analyzed by tracking individual peak movements in Movie S1. The Miller indices presented in the same row (e.g., FCC (333) and (511)) have the same d-spacing.

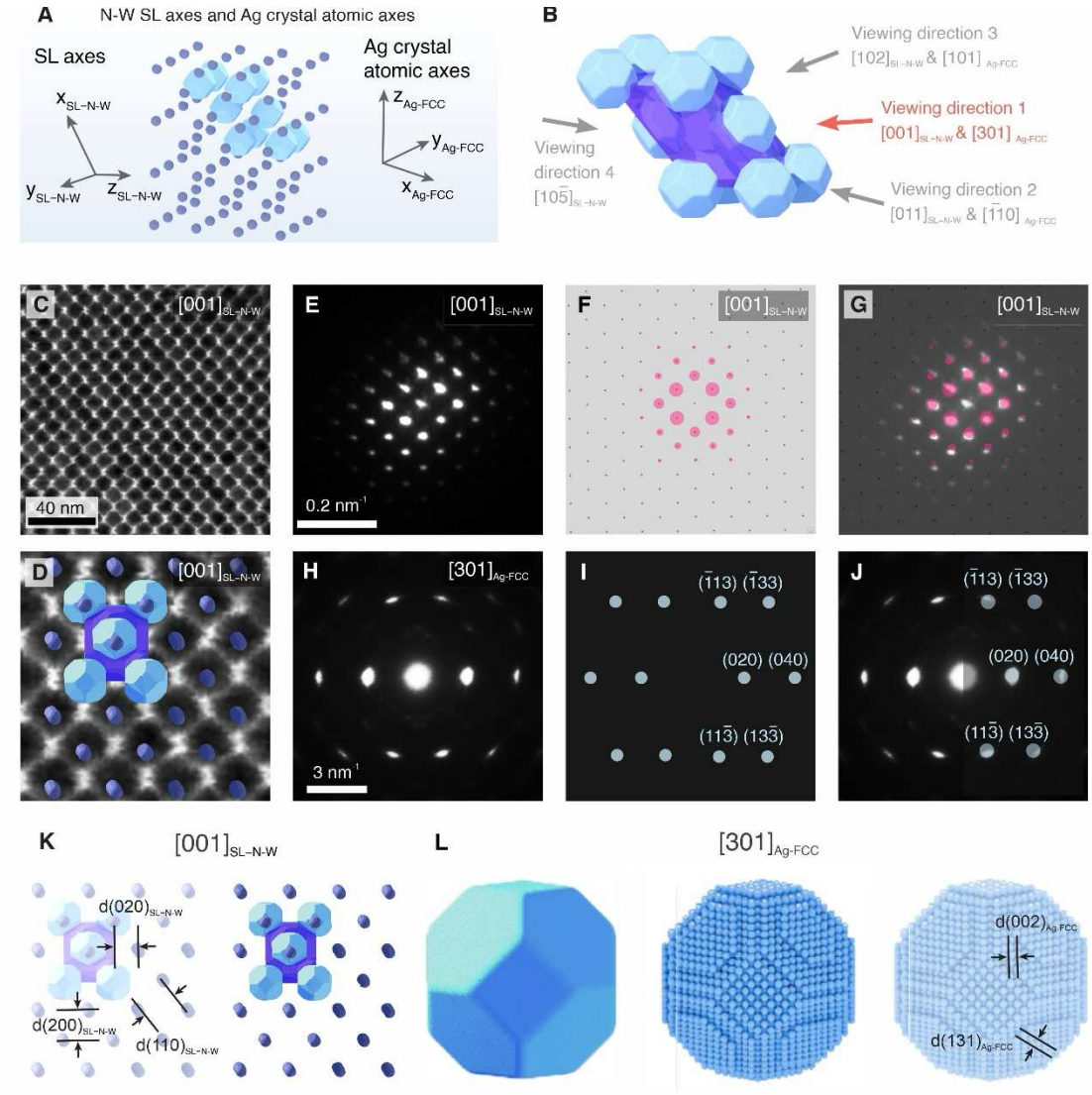


**Fig. S12. Rotational TEM results and analysis along viewing direction 1.** (**A**) N-W phase-intermediate SL model with the SL axis and Ag crystal atomic axis in NCs. (**B**) Schematics of the rotational TEM measurements. (**C-J**) Results from viewing direction 1: TEM image (**C**), overlapped presentation of the magnified TEM image and the assigned models (**D**), experimental selected-area SAED (**E**), simulated SAED (**F**), overlapped presentation of the experimental and simulation SAEDs (**G**), experimental selected-area WAED (**H**), simulated WAED (**I**), and overlapped presentation of experimental and simulated WAEDs (**J**). (**K,L**) Computer models of the SLs (**K**) and atomic models Ag-NCs (**L**) from viewing direction 1.

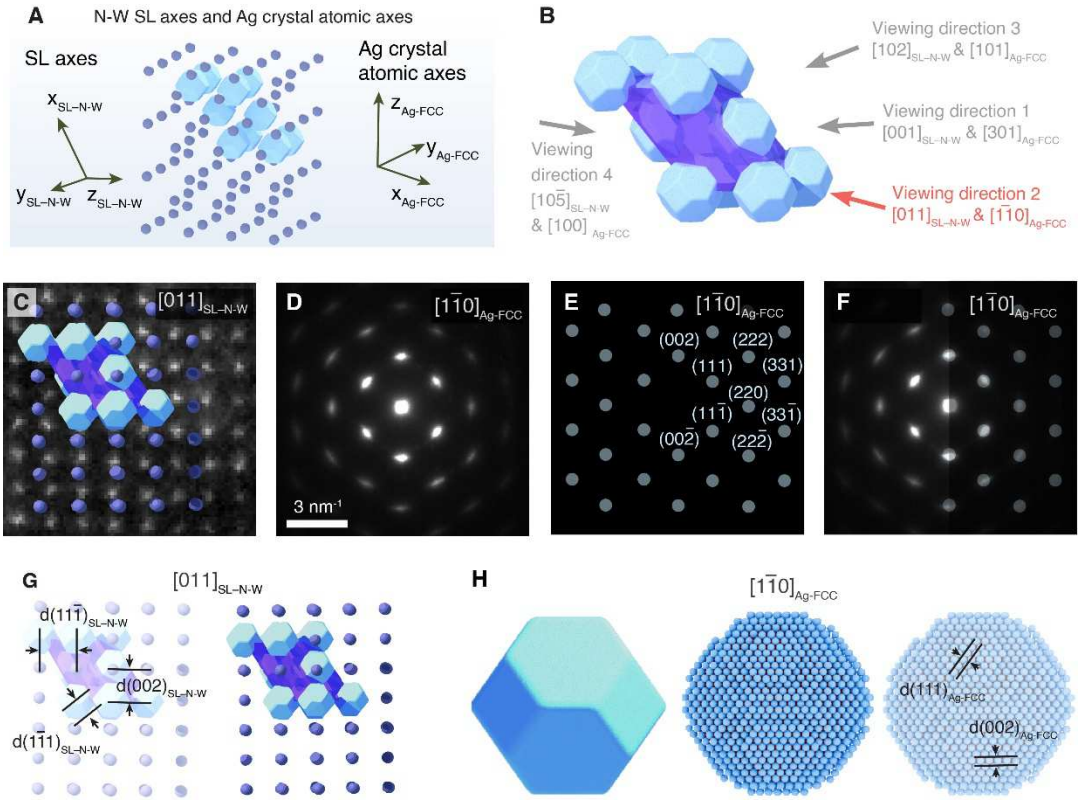


**Fig. S13. Rotational TEM results and analysis along viewing direction 2.** (**A**) N-W phase-intermediate SL model with the SL axes and Ag crystal atomic axes. (**B**) Schematics of the rotational TEM measurement showing different viewing directions. (**C-F**) Results from viewing direction 2: Overlapped presentation of the magnified TEM image and the assigned models (**C**), experimental selected-area WAED (**D**), simulated WAED (**E**), and overlapped presentation of experimental and simulated WAEDs (**F**). (**G, H**) Computer models of the SLs (**G**) and of Ag-NCs (**H**) from viewing direction 2.

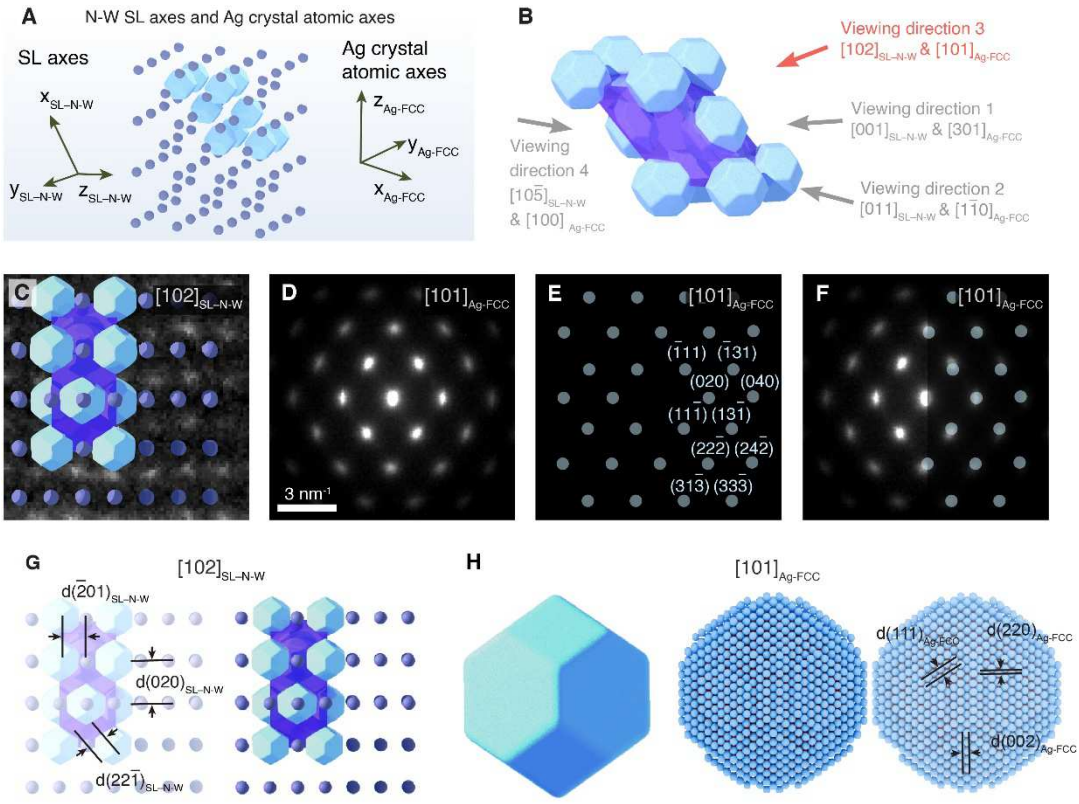


**Fig. S14. Rotational TEM results and analysis along viewing direction 3.** (**A**) N-W phase-intermediate SL model with the SL axes and Ag crystal atomic axes. (**B**) Schematics of the rotational TEM measurement showing different viewing directions. (**C-F**) Results from viewing direction 3: Overlapped presentation of the magnified TEM image and the assigned models (**C**), experimental selected-area WAED (**D**), simulated WAED (**E**), and overlapped presentation of experimental and simulated WAEDs (**F**). (**G, H**) Computer models of the SLs (**G**) and of Ag-NCs (**H**) from viewing direction 3.

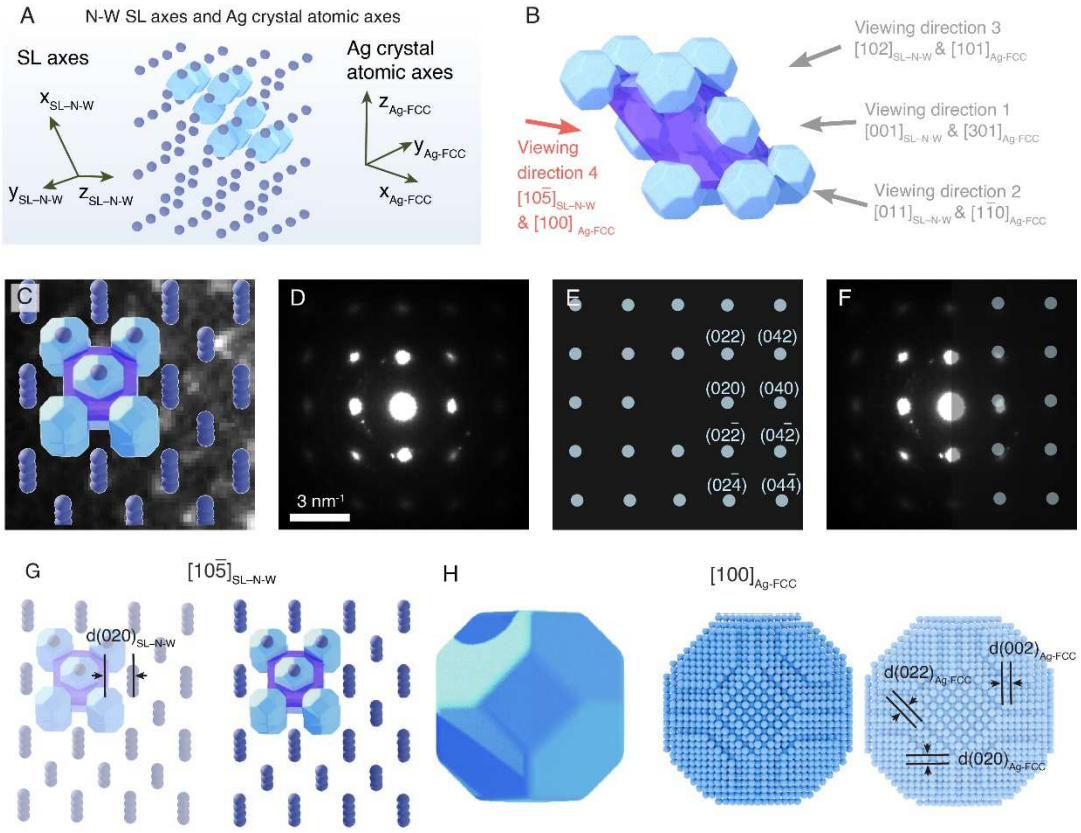


**Fig. S15 | Rotational TEM results and analysis along viewing direction 4.** (**A**) N-W phase-intermediate SL model with the SL axes and Ag crystal atomic axes. (**B**) Schematics of the rotational TEM measurement showing different viewing directions. (**C-F**) Results from viewing direction 4: Overlapped presentation of the magnified TEM image and the assigned models (**C**), experimental selected-area WAED (**D**), simulated WAED (**E**), and overlapped presentation of experimental and simulated WAEDs (**F**). (**G, H**) Computer models of the SLs (**G**) and of Ag-NCs (**H**) from viewing direction 4.

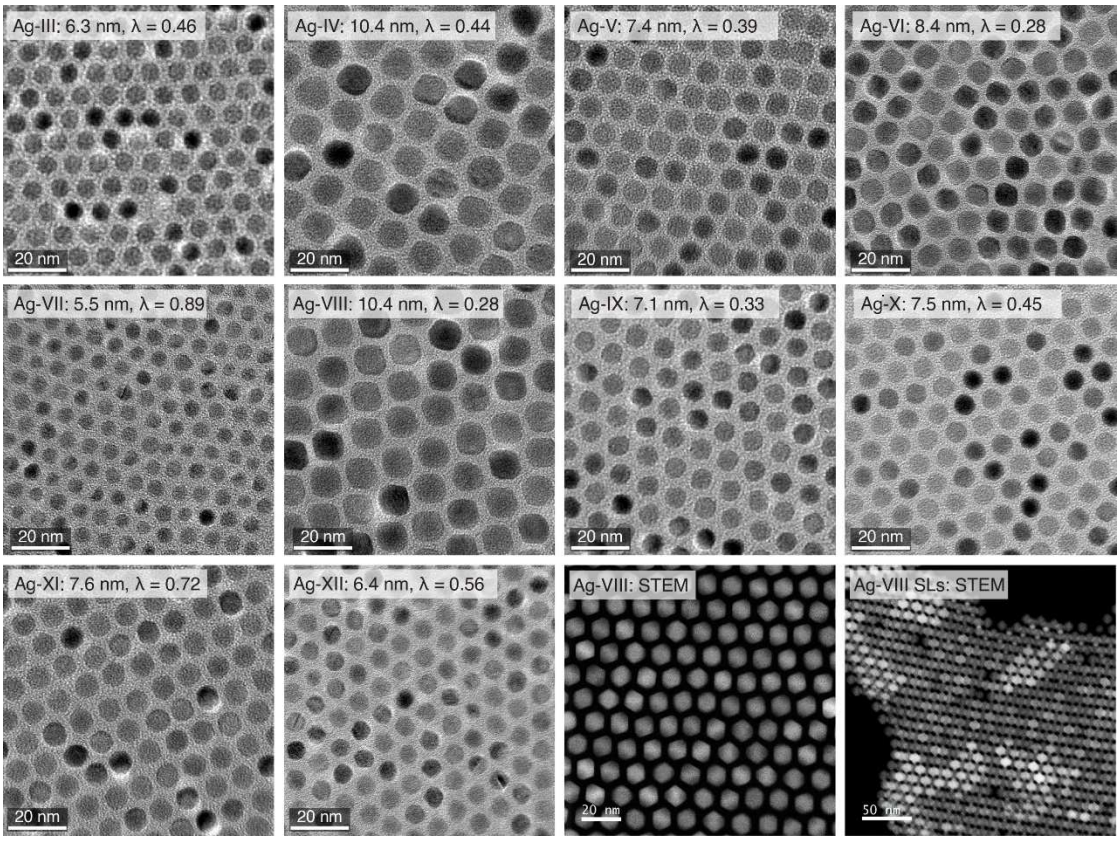


**Fig. S16. TEM images of various Ag-NCs with different sizes and sphericities.** The sample labels correspond to those listed in Table S1.

## Table S8. Detailed results of the SLs from various NCs used for Fig. 2E in the main text.

| Ag-NC Sample ID* | Spherical Ag-NC [a,c] | Mecon Ag-NC [a,c] | Ag with λ = 0.62 [b] | Ag with λ = 0.39 [c] | Ag with λ = 0.56 [c] | Ag with λ = 0.83 [c] | Ag-III | Ag-IV |
|---|---|---|---|---|---|---|---|---|
| **Size[d]** | 10.0 nm | 10.2 nm | 8.9 nm | 10.1 nm | 10.1 nm | 10.0 nm | 6.3 nm | 10.4 nm |
| **λ of Ag NCs** | 0.95 | 0.17 | 0.62 | 0.39 | 0.56 | 0.83 | 0.45 | 0.44 |
| **Ƭ of $SL_{N-W}$** | 0% | 100% | 33.8% | 90.8% | 65.1% | 22.1% | 89.3% | 79.6% |
| **LC[e] length** | **FCC:** 17.75 nm | **BCC:** 14.12 nm | ***a*:** 19.58 nm ***b,c***: 12.13 nm | ***a***: 19.18 nm ***b,c*** :13.32 nm | ***a***: 20.02 nm, ***b,c***: 13.21 nm | ***a***: 21.25 nm, ***b,c***: 12.85 nm | ***a***: 13.87 nm, ***b,c***: 9.60 nm | ***a***: 20.60 nm ***b,c***:14.00 nm |
| **LC[e] angle** | 90° | 90° | **α**, **γ** = 90° **β** = 128.6° | **α**, **γ** = 90° **β** = 134.1° | **α**, **γ** = 90° **β** = 131.6° | **α**, **γ** = 90° **β** = 127.4° | **α**, **γ** = 90° **β** = 134.0° | **α**, **γ** = 90° **β** = 133.0° |

| Ag-NC Sample ID* | Ag-V | Ag-VI | Ag-VII | Ag-VIII | Ag-IX | Ag-X | Ag-XI | Ag-XII |
|---|---|---|---|---|---|---|---|---|
| **Size[d]** | 7.4 nm | 8.4 nm | 5.5 nm | 10.4 nm | 7.1 nm | 7.5 nm | 7.6 nm | 6.4 nm |
| **λ of Ag NCs** | 0.39 | 0.28 | 0.89 | 0.28 | 0.33 | 0.45 | 0.72 | 0.56 |
| **Ƭ of $SL_{N-W}$** | 100% | 100% | 0% | 100% | 100% | 93.1% | 24.0% | 53.0% |
| **LC[a] length** | **BCC:** 10.61 nm | **BCC:** 11.44 nm | **FCC:** 11.22 nm | **BCC:** 14.48 nm | **BCC:** 10.25 nm | ***a*:** 15.39 nm, ***b,c***: 10.74 nm | ***a*:**15.76 nm, ***b,c***: 9.57 nm | ***a***: 14.97 nm, ***b,c***: 9.64 nm |
| **LC[e] angle** | 90° | 90° | 90° | 90° | 90° | **α**, **γ** = 90° **β** = 134.3° | **α**, **γ** = 90° **β** = 127.6° | **α**, **γ** = 90° **β** = 130.4° |

* The details of the Ag-NCs listed in this table are presented in Tables S1, 2. [a] These SLs are presented in Fig. 1. [b] This SL is presented in Fig. 2 [c] These SLs are presented in Fig. 3, and Fig. S30. [d] The presented sizes are the average of measured major diameters of the sample. [e] LC represents lattice constants of the unit cell.

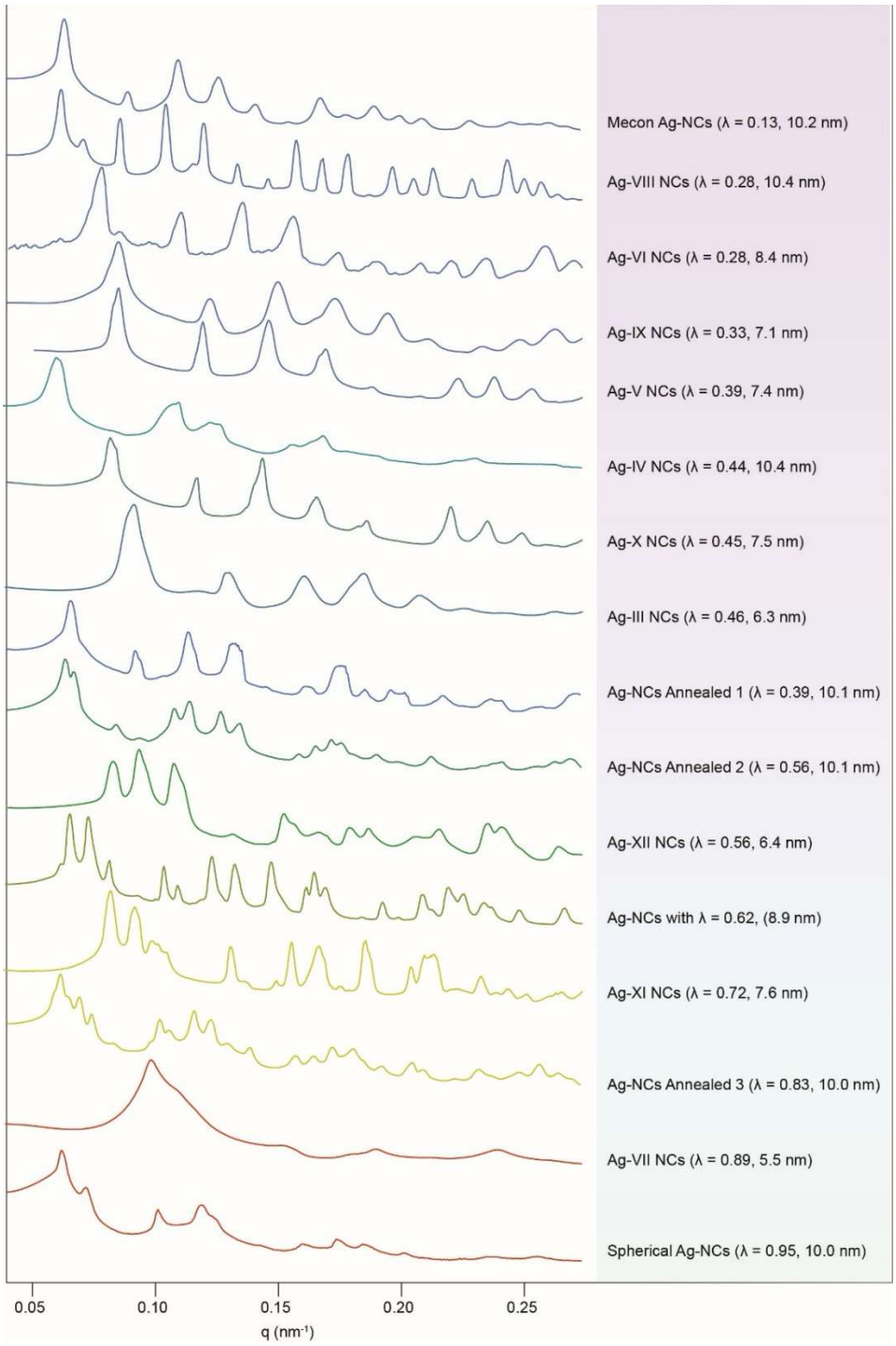


**Fig. S17. SAXS spectra of Ag-NC SLs collected in this study.** The spectra are arranged from top to bottom in the order of increasing sphericity value (λ) of the constituent Ag-NCs. Corresponding tabulated SL parameters are summarized in Table S8.

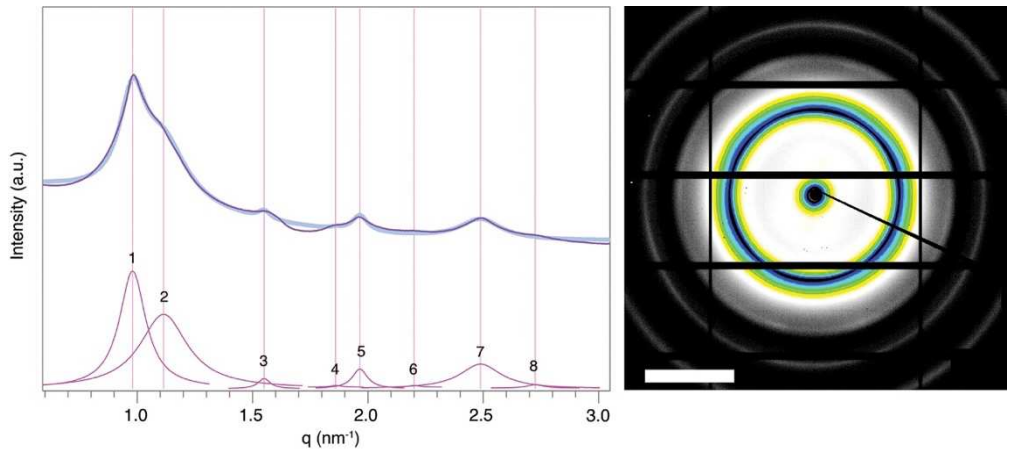


**Fig. S18. SAXS spectrum of FCC SLs from Ag-VII**. (left) The thick blue line, thin purple line, and purple-red peaks represent the experimentally-obtained SAXS spectrum, fitted spectrum, and constituent peaks used for fitting, respectively.(right) 2D SAXS pattern. The scale bar is 0.5 $nm^{-1}$.

**Table S9. Detailed results of SAXS spectrum presented in Fig. S18.**

| Peak number | 1 | 2 | 3 | 4 | 5 | 6 | 7 | 8 |
|---|---|---|---|---|---|---|---|---|
| Peak position (q/Å) | 0.0982 | 0.1106 | 0.1569 | 0.1847 | 0.1963 | 0.2202 | 0.2492 | 0.2739 |
| d-spacing (Å) | 63.96 | 56.79 | 40.05 | 34.02 | 32.01 | 28.54 | 25.21 | 22.94 |
| Peak assignment | FCC (111) | FCC (200) | FCC (220) | FCC (311) | FCC (222) | FCC (400) | FCC (331) | FCC (422) |

The assigned unit cell is an FCC (Ţ = 0%) with ***a*** = 11.22 (± 0.17) nm. Volume per one NC in the SL is 353.2 $nm^3$.

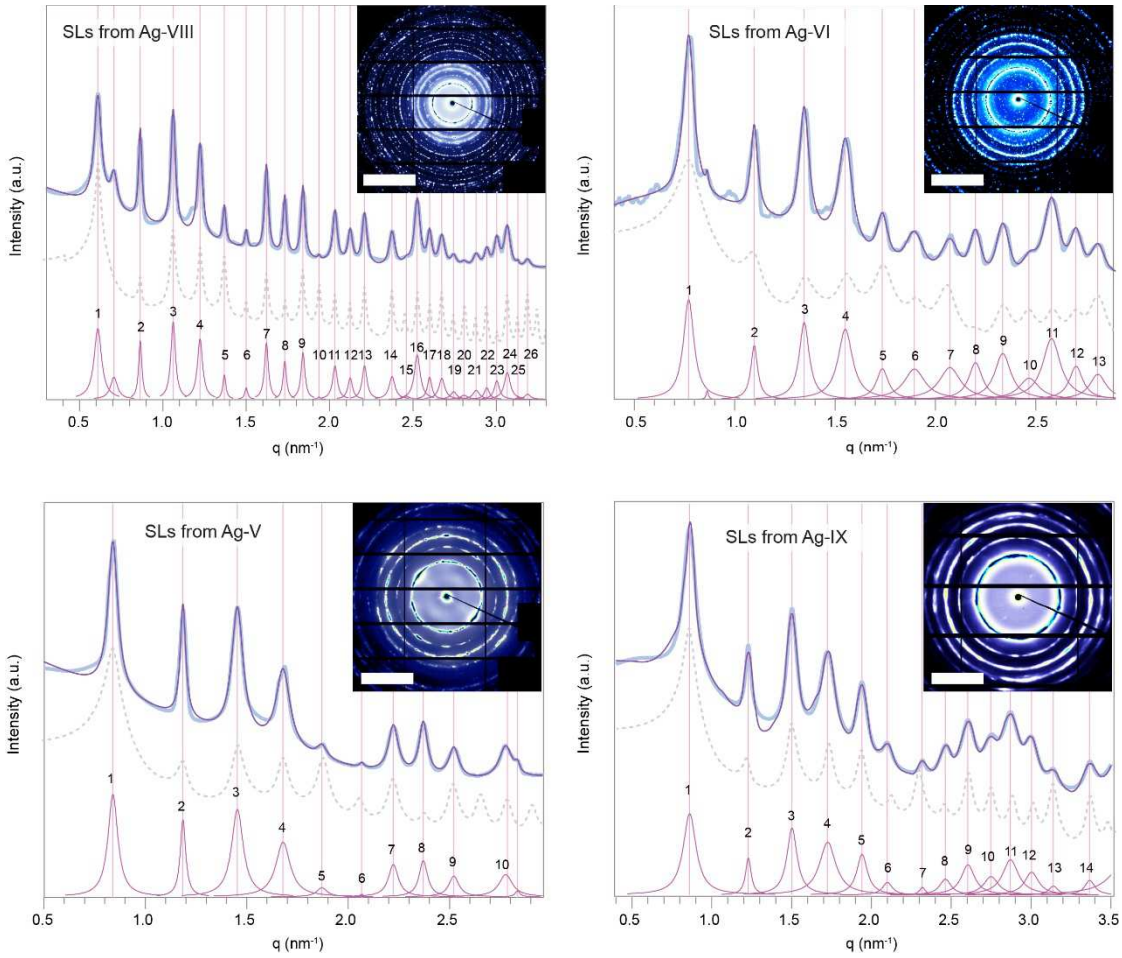


**Fig. S19. SAXS spectra of BCC SLs from Ag-VIII, VI, V, and IX.** The thick blue lines, thin purple lines, grey dashed lines, and purple-red peaks represent the experimentally-obtained SAXS spectra, fitted spectra, simulated spectra, and constituent peaks used for fitting, respectively. (Inset) 2D SAXS patterns. The scale bars are 0.5 $nm^{-1}$.

## Table S10. Detailed results of the SAXS spectrum of Ag-VIII SLs presented in Fig. S19 top left.

| Peak number | 1 | 2 | 3 | 4 | 5 | 6 | 7 | 8 | 9 | 10 |
|---|---|---|---|---|---|---|---|---|---|---|
| Peak position (q/Å) | 0.0611 | 0.0866 | 0.1063 | 0.1224 | 0.1371 | 0.1502 | 0.1624 | 0.1734 | 0.1843 | 0.1939 |
| d-spacing (Å) | 102.84 | 72.59 | 59.09 | 51.31 | 45.83 | 41.83 | 38.69 | 36.24 | 34.09 | 32.40 |
| Peak assignment | BCC (110) | BCC (200) | BCC (211) | BCC (220) | BCC (310) | BCC (222) | BCC (321) | BCC (400) | BCC (330) | BCC (420) |
| **Peak number** | **11** | **12** | **13** | **14** | **15** | **16** | **17** | **18** | **19** | **20** |
| Peak position (q/Å) | 0.2036 | 0.2127 | 0.2213 | 0.2379 | 0.2453 | 0.2530 | 0.2604 | 0.2677 | 0.2749 | 0.2811 |
| d-spacing (Å) | 30.87 | 29.54 | 28.39 | 26.42 | 25.62 | 24.84 | 24.13 | 23.47 | 22.86 | 22.35 |
| Peak assignment | BCC (332) | BCC (422) | BCC (510) | BCC (521) | BCC (440) | BCC (530) | BCC (600) | BCC (611) | BCC (620) | BCC (541) |
| **Peak number** | **21** | **22** | **23** | **24** | **25** | **26** | | | | |
| Peak position (q/Å) | 0.2883 | 0.2948 | 0.3008 | 0.3071 | 0.3133 | 0.3193 | | | | |
| d-spacing (Å) | 21.79 | 21.31 | 20.89 | 20.46 | 20.05 | 19.68 | | | | |
| Peak assignment | BCC (622) | BCC (631) | BCC (444) | BCC (550) | BCC (640) | BCC (552) | | | | |

The assigned unit cell is a BCC ($\tau$ = 100%) with ***a*** = 14.48 (± 0.02) nm. Volume per one NC in the SL is 1518.0 nm$^3$.

## Table S11. Detailed results of the SAXS spectrum of Ag-VI SLs presented in Fig. S19 top right.

| Peak number | 1 | 2 | 3 | 4 | 5 | 6 | 7 | 8 | 9 | 10 |
|---|---|---|---|---|---|---|---|---|---|---|
| Peak position (q/Å) | 0.0770 | 0.1097 | 0.1346 | 0.1550 | 0.1735 | 0.1895 | 0.2071 | 0.2199 | 0.2335 | 0.2466 |
| d-spacing (Å) | 81.58 | 57.30 | 46.69 | 40.53 | 36.22 | 33.16 | 30.33 | 28.57 | 26.91 | 25.48 |
| Peak assignment | BCC (110) | BCC (200) | BCC (211) | BCC (220) | BCC (310) | BCC (222) | BCC (321) | BCC (400) | BCC (330) | BCC (420) |
| **Peak number** | **11** | **12** | **13** | | | | | | | |
| Peak position (q/Å) | 0.2578 | 0.2700 | 0.2809 | | | | | | | |
| d-spacing (Å) | 24.38 | 23.27 | 22.37 | | | | | | | |
| Peak assignment | BCC (332) | BCC (422) | BCC (510) | | | | | | | |

The assigned unit cell is a BCC ($\tau$ = 100%) with ***a*** = 11.44 (± 0.05) nm. Volume per one NC in the SL is 747.8 nm$^3$.

## Table S12. Detailed results of the SAXS spectrum of Ag-V SLs presented in Fig. S19 bottom left.

| Peak number | 1 | 2 | 3 | 4 | 5 | 6 | 7 | 8 | 9 | 10 |
|---|---|---|---|---|---|---|---|---|---|---|
| Peak position (q/Å) | 0.0840 | 0.1185 | 0.1453 | 0.1678 | 0.1870 | 0.2066 | 0.2222 | 0.2370 | 0.2520 | 0.2776 |
| d-spacing (Å) | 74.82 | 53.02 | 43.23 | 37.43 | 33.59 | 30.41 | 28.27 | 26.51 | 24.93 | 22.63 |
| Peak assignment | BCC (110) | BCC (200) | BCC (211) | BCC (220) | BCC (310) | BCC (222) | BCC (321) | BCC (400) | BCC (330) | BCC (420) |

The assigned unit cell is a BCC (ϒ = 100%) with ***a*** = 10.61 (± 0.09) nm. Volume per one NC in the SL is 597.9 nm$^3$.

## Table S13. Detailed results of the SAXS spectrum of Ag-IX SLs presented in Fig. S19 bottom right.

| Peak number | 1 | 2 | 3 | 4 | 5 | 6 | 7 | 8 | 9 | 10 |
|---|---|---|---|---|---|---|---|---|---|---|
| Peak position (q/Å) | 0.0861 | 0.1229 | 0.1502 | 0.1725 | 0.1941 | 0.2100 | 0.2319 | 0.2462 | 0.2604 | 0.2748 |
| d-spacing (Å) | 72.97 | 51.14 | 41.83 | 36.42 | 32.38 | 29.92 | 27.10 | 25.52 | 24.13 | 22.86 |
| Peak assignment | BCC (110) | BCC (200) | BCC (211) | BCC (220) | BCC (310) | BCC (222) | BCC (321) | BCC (400) | BCC (330) | BCC (420) |
| Peak number | 11 | 12 | 13 | 14 | | | | | | |
| Peak position (q/Å) | 0.2870 | 0.3003 | 0.3139 | 0.3366 | | | | | | |
| d-spacing (Å) | 21.89 | 20.93 | 20.02 | 18.66 | | | | | | |
| Peak assignment | BCC (332) | BCC (422) | BCC (510) | BCC (521) | | | | | | |

The assigned unit cell is a BCC (ϒ = 100%) with ***a*** = 10.25 (± 0.05) nm. Volume per one NC in the SL is 538.0 nm$^3$.

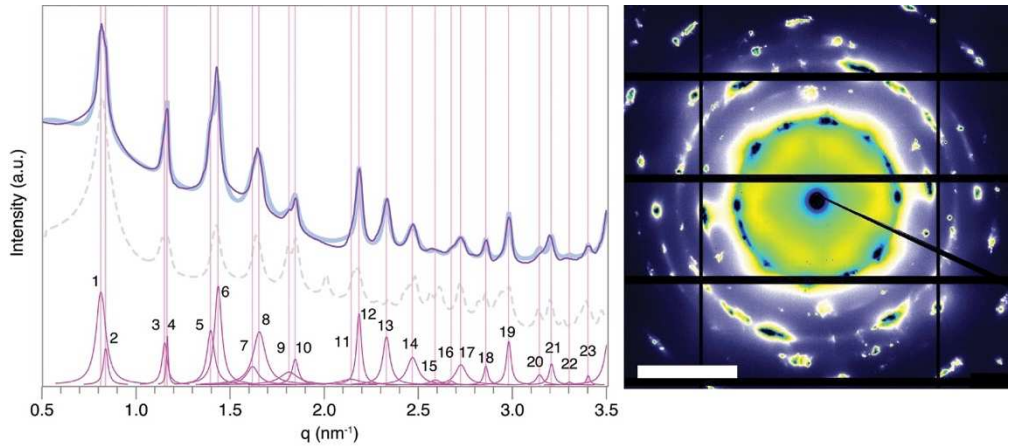


**Fig. S20. SAXS spectrum of Ag-X SLs.** (left) The thick blue line, thin purple line, grey dashed line, and purple-red peaks represent the experimentally-obtained SAXS spectrum, fitted spectrum, simulated spectrum, and constituent peaks used for fitting, respectively. (right) 2D SAXS pattern. The scale bar is 0.5 $nm^{-1}$.

**Table S14. Detailed results of the SAXS spectrum of Ag-X SLs presented in Fig. S20.**

| Peak number | **1** | **2** | **3** | **4** | **5** | **6** | **7** | **8** | **9** | **10** |
|---|---|---|---|---|---|---|---|---|---|---|
| Peak position (q/Å) | 0.0813 | 0.0839 | 0.1152 | 0.1166 | 0.1397 | 0.1436 | 0.1619 | 0.1655 | 0.1813 | 0.1846 |
| d-spacing (Å) | 77.25 | 74.93 | 54.54 | 53.88 | 44.99 | 43.75 | 38.80 | 37.97 | 34.65 | 34.04 |
| Peak number | **11** | **12** | **13** | **14** | **15** | **16** | **17** | **18** | **19** | **20** |
| Peak position (q/Å) | 0.2155 | 0.2185 | 0.2331 | 0.2469 | 0.2591 | 0.2676 | 0.2726 | 0.2859 | 0.2981 | 0.3144 |
| d-spacing (Å) | 29.16 | 28.76 | 26.96 | 25.45 | 24.25 | 23.48 | 23.05 | 21.98 | 21.08 | 19.98 |
| Peak number | **21** | **22** | **23** | | | | | | | |
| Peak position (q/Å) | 0.3208 | 0.3303 | 0.3403 | | | | | | | |
| d-spacing (Å) | 19.59 | 19.02 | 18.47 | | | | | | | |

The assigned unit cell is a base-centered monoclinic with lattice constants of ***a*** = 15.39 nm ***b,c*** = 10.74 nm, **α, γ** = 90°, and **β** = 134.33°. The **ζ** and ***ucc*** values are 93.1% and 9.39 nm, respectively. Volume per one NC in the SL is 634.8 $nm^3$.

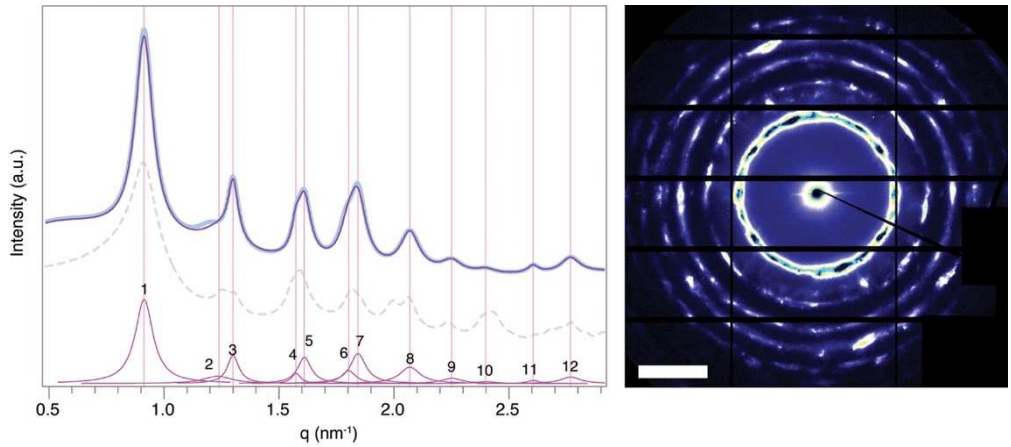


**Fig. S21. SAXS spectrum of Ag-III SLs.** (left) The pale blue line, thin purple line, grey dashed line, and purple-red peaks represent the experimentally-obtained SAXS spectrum, fitted spectrum, simulated spectrum, and constituent peaks used for fitting, respectively. (right) 2D SAXS pattern. The scale bar is 0.5 $nm^{-1}$.

**Table S15. Detailed results of the SAXS spectrum of Ag-III SLs presented in Fig. S21.**

| Peak number | **1** | **2** | **3** | **4** | **5** | **6** | **7** | **8** | **9** | **10** |
|---|---|---|---|---|---|---|---|---|---|---|
| Peak position (q/Å) | 0.0913 | 0.1240 | 0.1301 | 0.1574 | 0.1610 | 0.1800 | 0.1843 | 0.2069 | 0.2251 | 0.2399 |
| d-spacing (Å) | 68.81 | 50.67 | 48.33 | 39.92 | 39.02 | 35.10 | 34.91 | 30.37 | 27.91 | 26.20 |
| Peak number | **11** | **12** | | | | | | | | |
| Peak position (q/Å) | 0.2605 | 0.2768 | | | | | | | | |
| d-spacing (Å) | 24.12 | 22.70 | | | | | | | | |

The assigned unit cell is a base-centered monoclinic with lattice constants of ***a*** = 13.87 nm ***b,c*** = 9.60 nm, **α**, **γ** = 90°, and **β** = 133.96°. The **ζ** and ***ucc*** values are 89.3% and 8.43 nm, respectively. Volume per one NC in the SL is 460.5 $nm^3$.

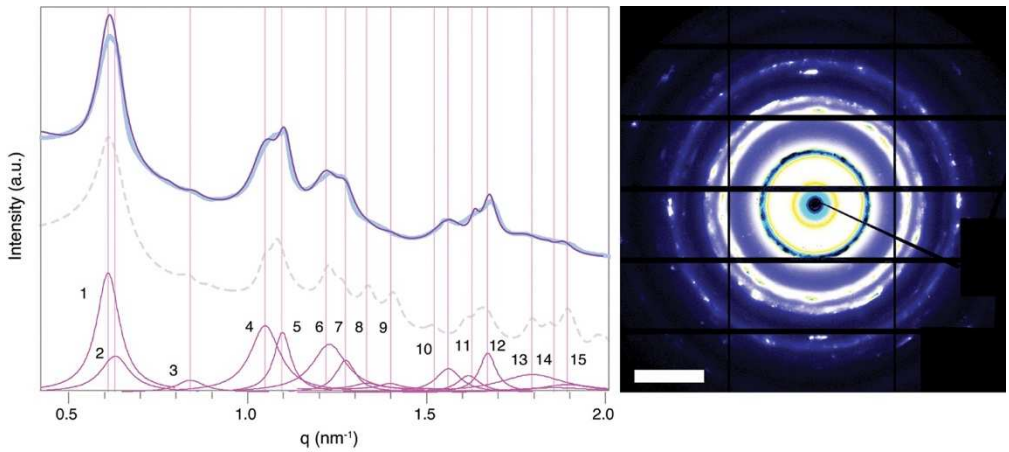


**Fig. S22. SAXS spectrum of Ag-IV SLs.** (left) The pale blue line, thin purple line, grey dashed line, and purple-red peaks represent the experimentally-obtained SAXS spectrum, fitted spectrum, simulated spectrum, and constituent peaks used for fitting, respectively. (right) 2D SAXS pattern. The scale bar is 0.5 $nm^{-1}$.

**Table S16. Detailed results of the SAXS spectrum of Ag-IV SLs presented in Fig. S22.**

| Peak number | 1 | 2 | 3 | 4 | 5 | 6 | 7 | 8 | 9 | 10 |
|---|---|---|---|---|---|---|---|---|---|---|
| Peak position (q/Å) | 0.0610 | 0.0630 | 0.0840 | 0.1050 | 0.1105 | 0.1230 | 0.1276 | 0.1330 | 0.1400 | 0.1525 |
| d-spacing (Å) | 103.00 | 99.73 | 74.80 | 59.84 | 56.86 | 51.08 | 49.24 | 47.24 | 44.88 | 41.20 |
| Peak number | 11 | 12 | 13 | 14 | 15 | | | | | |
| Peak position (q/Å) | 0.1620 | 0.1674 | 0.1798 | 0.1860 | 0.1897 | | | | | |
| d-spacing (Å) | 38.79 | 38.37 | 37.41 | 35.28 | 34.11 | | | | | |

The assigned unit cell is a base-centered monoclinic with lattice constants of ***a*** = 20.60 nm ***b,c*** = 14.00 nm, **α, γ** = 90°, and **β** = 133.01°. The **ζ** and ***ucc*** values are 79.6% and 12.47 nm, respectively. Volume per one NC in the SL is 1475.0 $nm^3$.

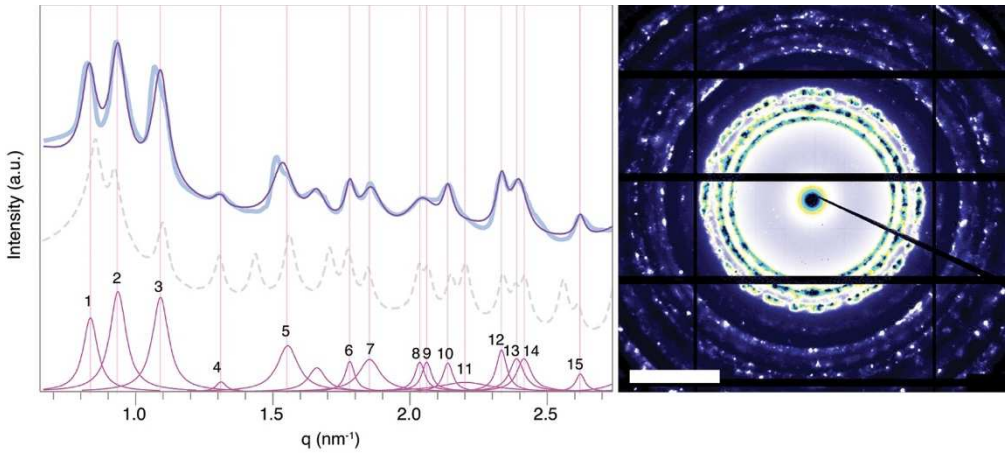


**Fig. S23. SAXS spectrum of Ag-XII SLs.** (left) The thick pale blue line, thin purple line, grey dashed line, and purple-red peaks represent the experimentally-obtained SAXS spectrum, fitted spectrum, simulated spectrum, and constituent peaks used for fitting, respectively. (right) 2D SAXS pattern. The scale bar is 0.5 $nm^{-1}$.

**Table S17. Detailed results of the SAXS spectrum of Ag-XII SLs presented in Fig. S23.**

| Peak number | **1** | **2** | **3** | **4** | **5** | **6** | **7** | **8** | **9** | **10** |
|---|---|---|---|---|---|---|---|---|---|---|
| Peak position (q/Å) | 0.0830 | 0.0935 | 0.1090 | 0.1310 | 0.1535 | 0.1660 | 0.1780 | 0.2033 | 0.2055 | 0.2138 |
| d-spacing (Å) | 75.70 | 67.20 | 57.64 | 47.96 | 40.93 | 37.85 | 35.30 | 30.91 | 30.58 | 29.39 |
| Peak number | **11** | **12** | **13** | **14** | **15** | | | | | |
| Peak position (q/Å) | 0.2200 | 0.2333 | 0.2377 | 0.2410 | 0.2620 | | | | | |
| d-spacing (Å) | 28.56 | 26.93 | 26.43 | 26.07 | 23.98 | | | | | |

The assigned unit cell is a base-centered monoclinic with lattice constants of ***a*** = 14.97 nm ***b,c*** = 9.64 nm, **α, γ** = 90°, and **β** = 130.42°. The **ϒ** and ***ucc*** values are 53.0% and 8.91 nm, respectively. Volume per one NC in the SL is 529.4 $nm^3$.

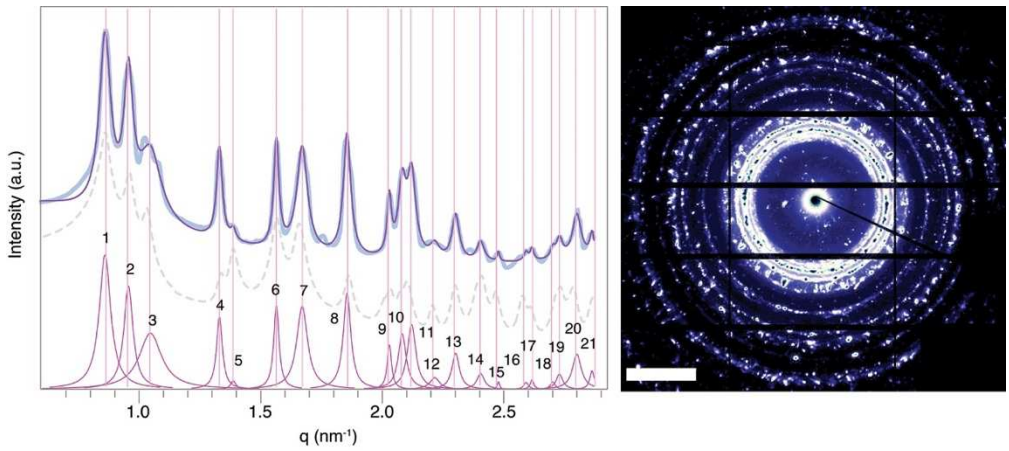


**Fig. S24. SAXS spectrum of Ag-XI SLs.** (left) The thick blue line, thin purple line, grey dashed line, and purple-red peaks represent the experimentally-obtained SAXS spectrum, fitted spectrum, simulated spectrum, and constituent peaks used for fitting, respectively. (right) 2D SAXS pattern. The scale bar is 0.5 $nm^{-1}$.

**Table S18. Detailed results of the SAXS spectrum of Ag-XI SLs presented in Fig. S24.**

| Peak number | **1** | **2** | **3** | **4** | **5** | **6** | **7** | **8** | **9** | **10** |
|---|---|---|---|---|---|---|---|---|---|---|
| Peak position (q/Å) | 0.0825 | 0.0925 | 0.1018 | 0.1310 | 0.1369 | 0.1551 | 0.1661 | 0.1851 | 0.2030 | 0.2084 |
| d-spacing (Å) | 76.11 | 67.95 | 61.74 | 47.95 | 45.90 | 40.50 | 37.83 | 33.95 | 30.95 | 30.14 |
| Peak number | **11** | **12** | **13** | **14** | **15** | **16** | **17** | **18** | **19** | **20** |
| Peak position (q/Å) | 0.2124 | 0.2222 | 0.2311 | 0.2417 | 0.2492 | 0.2609 | 0.2634 | 0.2722 | 0.2750 | 0.2824 |
| d-spacing (Å) | 29.58 | 28.27 | 27.19 | 26.00 | 25.21 | 24.08 | 23.85 | 23.08 | 22.84 | 22.25 |
| Peak number | **21** | | | | | | | | | |
| Peak position (q/Å) | 0.2888 | | | | | | | | | |
| d-spacing (Å) | 21.75 | | | | | | | | | |

The assigned unit cell is a base-centered monoclinic with lattice constants of ***a*** = 15.76 nm ***b,c*** = 9.57 nm, **α**, **γ** = 90°, and **β** = 127.60°. The **ϒ** and ***ucc*** values are 24.0% and 15.76 nm, respectively. Volume per one NC in the SL is 571.2 $nm^3$.

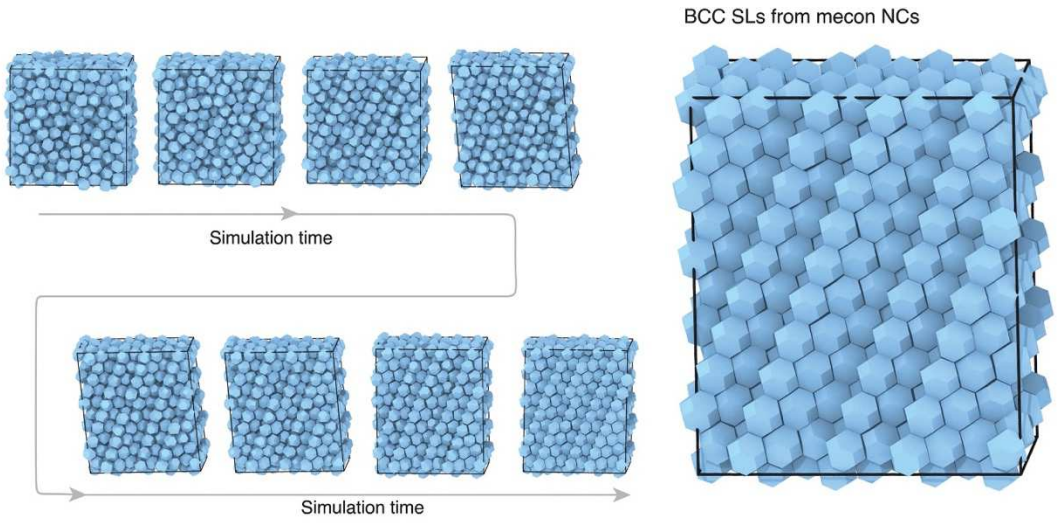


**Fig. S25. Snapshots of Movie S6.** MD Simulation trajectory for λ = 0.0 (mecon) with the total (stiff + soft) pair potential model is presented.

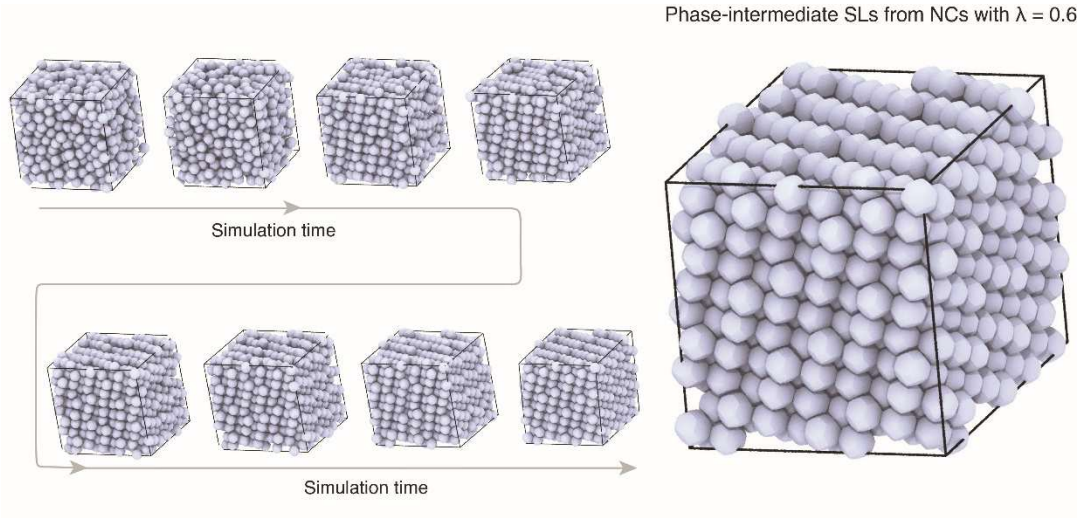


**Fig. S26. Snapshots of Movie S7.** MD Simulation trajectory for λ = 0.6 (intermediate shape) with the total (stiff + soft) pair potential model is presented.

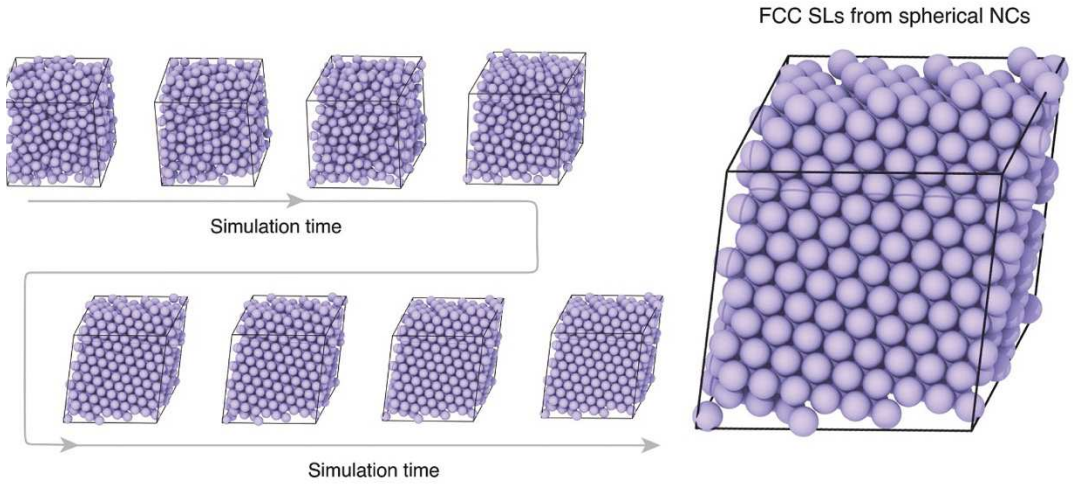


**Fig. S27. Snapshots of Movie S8.** MD Simulation trajectory for $\lambda = 1.0$ (sphere) with the total (stiff + soft) pair potential model is presented.

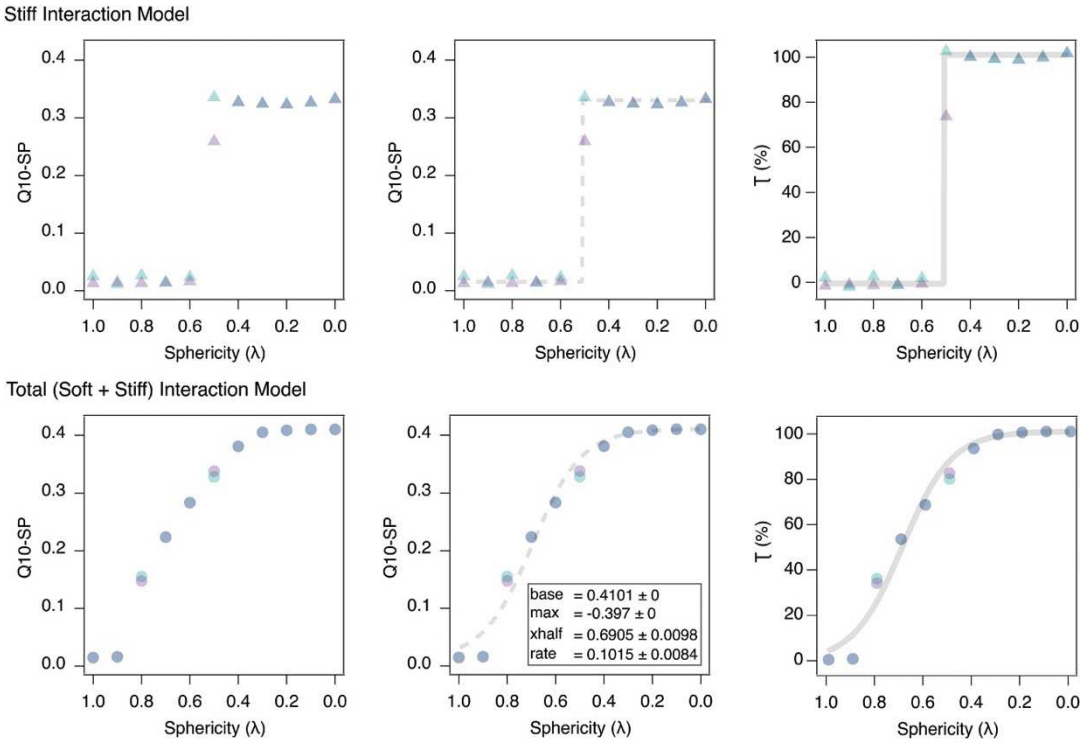


**Fig. S28. Conversion from Steinhardt parameter (Q10-SP) to Ţ values.** (top) Simulation from stiff interaction models, and (bottom) from total interaction models. In both results, the left, center, and right panels present Q10-SP plots extracted from the simulation results, fitting results using sigmoid functions and the fitting parameters, and conversions from Q10-SP to Ţ values, respectively. See also '*SL Formation Simulation* and *Orientational Order Diagrams Analyses'* section in Methods.

Note: We conducted the conversion from Q10-SP to Ţ values for quantitative comparisons between simulations and experiments. The conversion was done by normalization of the plots by taking the base and minimal values of Q10-SP as 100% and 0% in Ţ values. In this normalization process, we converted 0.327 and 0.410 of Q10-SP values to 100% Ţ values (perfect BCC) for the results from hard object models and from total interaction models, respectively. It should be noted that while Q10-SP values indicate the superstructure information in the system, structural fluctuations also affected Q10-SP values. Hard object models result in superstructures with high fluctuations, leading to lower coordination environments hence lower Q10-SP values.

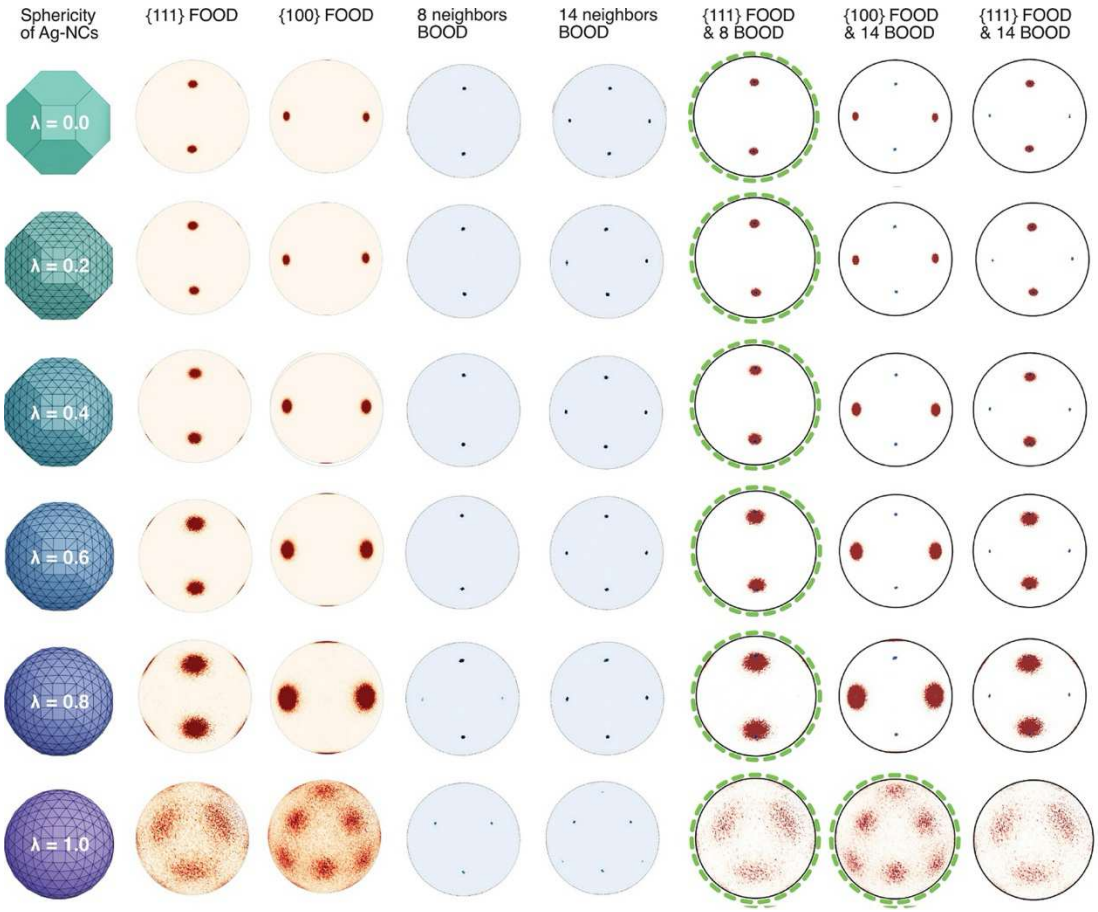


**Fig. S29. Orientational order diagrams from simulated SL models with various sphericity parameter values**. 1st column: FOODs for $(111)_{Ag\text{-}FCC}$ facets; 2nd column: FOODs for $(100)_{Ag\text{-}FCC}$ facets; 3rd column: BOODs for 8 nearest neighbors; 4th column: BOODs for 14 nearest neighbors; 5th, 6th, and 7th column: Overlay presentations of $(111)_{Ag\text{-}FCC}$ FOODs + 8 neighbor BOODs, $(100)_{Ag\text{-}FCC}$ FOODs + 14 neighbor BOODs, and $(111)_{Ag\text{-}FCC}$ FOODs + 14 neighbor BOODs, respectively. The green dashed circles indicate that the signals from the BOODs and FOODs are located in the same positions.

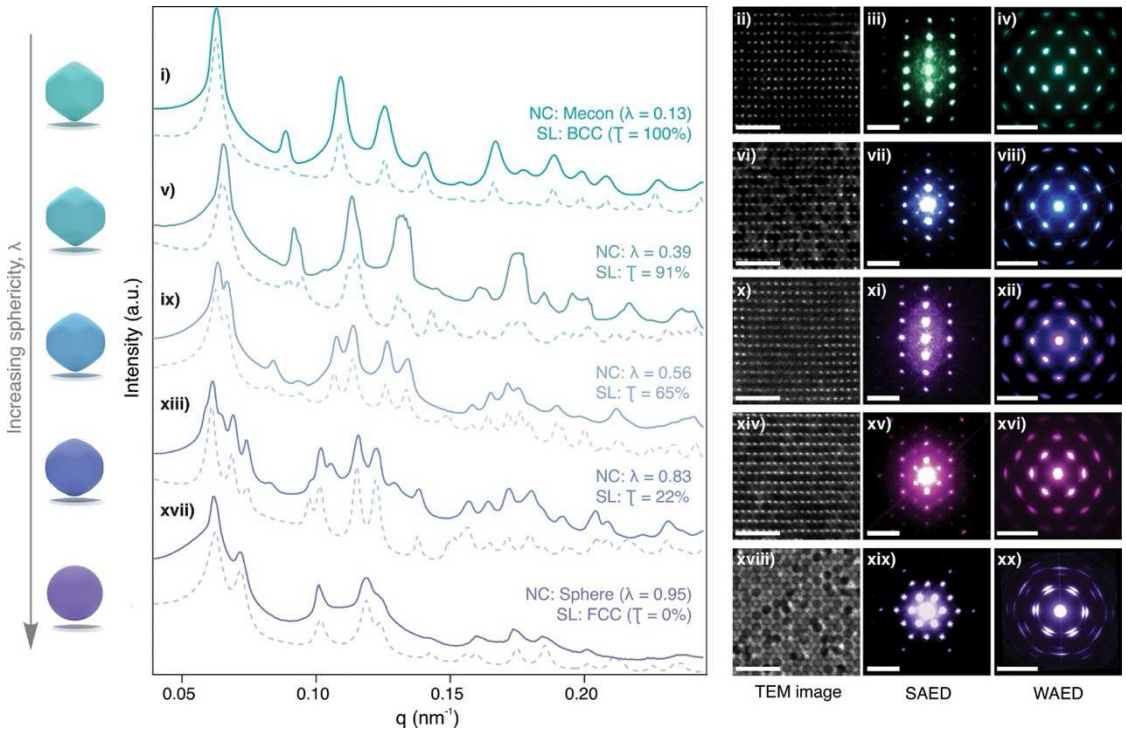


**Fig. S30. SLs from Ag-NCs with a particle volume of ca. 520 nm$^3$ and various sphericity parameters.** (i-iv) BCC SLs (Ţ = 100%) from mecon Ag-NCs (λ = 0.13); (v-viii) N-W phase-intermediate SLs with Ţ = 91% from Ag-NCs with λ = 0.39, (ix-xii) N-W phase-intermediate SLs with Ţ = 65% from Ag-NCs with λ = 0.56; (xiii-xvi) phase-intermediate SLs with Ţ = 22% from Ag-NCs with λ = 0.83; (xvii-xx) FCC SLs (Ţ = 0%) from near spherical Ag-NCs (λ = 0.95). (i, v, ix, xiii, xvii) SAXS patterns, (ii, vi, x, xiv, xviii) TEM images (scale bars, 40 nm), (iii, vii, xi, xv, xix) SAED patterns (scale bars, 0.1 nm$^{-1}$), and (iv, viii, xii, xvi, xx) WAED patterns (scale bars, 4 nm$^{-1}$).

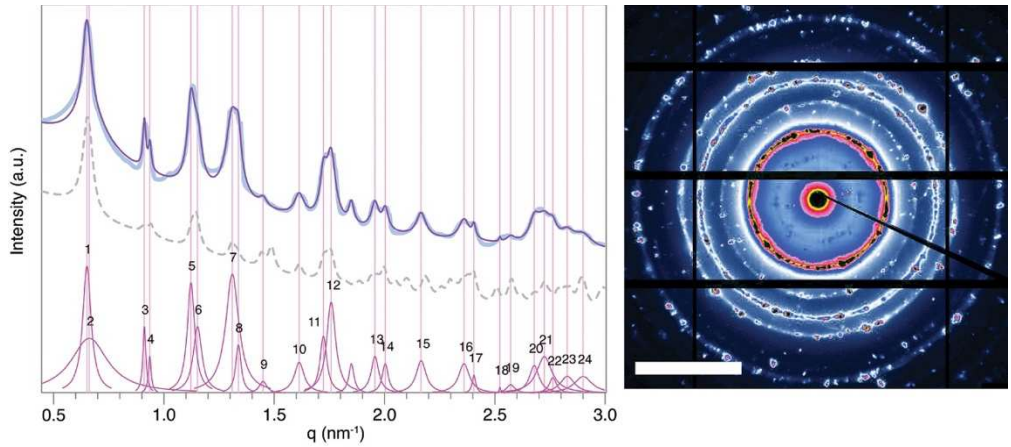


**Fig. S31. SAXS spectrum of SLs from Ag-NCs with λ of 0.39 with a particle volume of ca. 520 nm$^3$.** (left) SAXS spectrum of SLs from Ag-NCs with λ of 0.39 with the same individual particle volume as spherical and mecon Ag-NCs. The thick blue line, thin purple line, grey dashed line, and purple-red peaks represent the experimentally-obtained SAXS spectrum, the fitted spectrum, the simulated spectrum, and the constituent peaks used for fitting, respectively. (right) 2D SAXS pattern. The scale bar is 0.5 nm$^{-1}$.

**Table S19. Detailed results of the SAXS spectrum presented in Fig. S31.**

| Peak number | **1** | **2** | **3** | **4** | **5** | **6** | **7** | **8** | **9** | **10** |
|---|---|---|---|---|---|---|---|---|---|---|
| Peak position (q/Å) | 0.0654 | 0.0665 | 0.0914 | 0.0939 | 0.1125 | 0.1155 | 0.1312 | 0.1340 | 0.1452 | 0.1615 |
| d-spacing (Å) | 96.09 | 94.48 | 68.73 | 66.92 | 55.84 | 54.40 | 47.88 | 46.89 | 43.28 | 38.90 |
| Peak number | **11** | **12** | **13** | **14** | **15** | **16** | **17** | **18** | **19** | **20** |
| Peak position (q/Å) | 0.1725 | 0.1760 | 0.1958 | 0.2005 | 0.2167 | 0.2362 | 0.2407 | 0.2525 | 0.2573 | 0.2680 |
| d-spacing (Å) | 36.42 | 35.70 | 32.08 | 31.34 | 28.99 | 26.61 | 26.11 | 24.89 | 24.42 | 23.45 |
| Peak number | **21** | **22** | **23** | **24** | | | | | | |
| Peak position (q/Å) | 0.2725 | 0.2764 | 0.2829 | 0.2901 | | | | | | |
| d-spacing (Å) | 23.06 | 22.73 | 22.21 | 21.66 | | | | | | |

The assigned unit cell is a base-centered monoclinic with lattice constants of ***a*** = 19.18 nm, ***b, c*** = 13.32 nm, **α, γ** = 90°, and **β** = 134.10°. The **ϒ** and ***ucc*** values are 90.8% and 11.68 nm, respectively. Volume per one NC in the SL is 1222.0 nm$^3$.

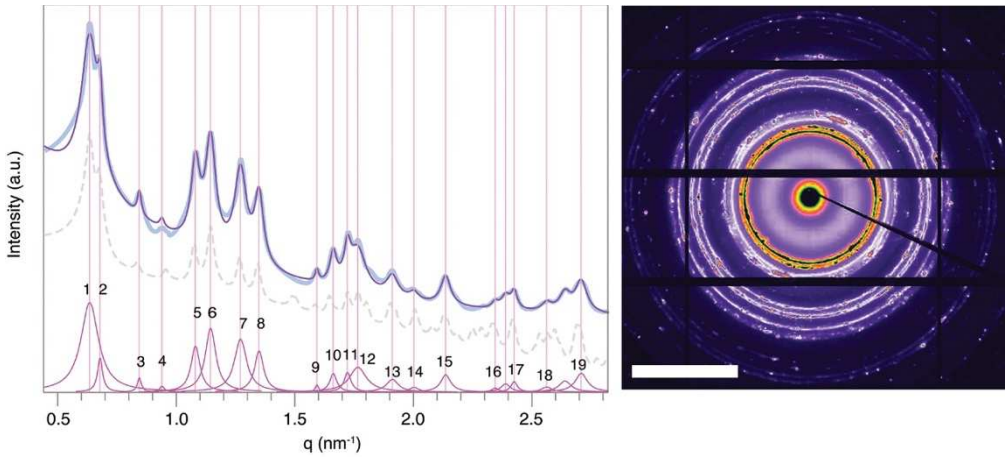


**Fig. S32. SAXS spectrum of SLs from Ag-NCs with λ of 0.56 with a particle volume of ca. 520 nm$^3$.** (left) SAXS spectrum of SLs from Ag-NCs with λ of 0.56 with the same individual particle volume as spherical and mecon Ag-NCs. The thick blue line, thin purple line, grey dashed line, and purple-red peaks represent the experimentally-obtained SAXS spectrum, the fitted spectrum, the simulated spectrum, and the constituent peaks used for fitting, respectively. (right) 2D SAXS pattern. The scale bar is 0.5 nm$^{-1}$.

**Table S20. Detailed results of the SAXS spectrum presented in Fig. S32.**

| Peak number | 1 | 2 | 3 | 4 | 5 | 6 | 7 | 8 | 9 | 10 |
|---|---|---|---|---|---|---|---|---|---|---|
| Peak position (q/Å) | 0.0633 | 0.0677 | 0.0843 | 0.0938 | 0.1079 | 0.1143 | 0.1269 | 0.1347 | 0.1590 | 0.1659 |
| d-spacing (Å) | 99.20 | 92.81 | 74.57 | 66.99 | 58.25 | 54.99 | 49.53 | 46.66 | 39.51 | 37.87 |
| Peak number | 11 | 12 | 13 | 14 | 15 | 16 | 17 | 18 | 19 | |
| Peak position (q/Å) | 0.1719 | 0.1763 | 0.1908 | 0.1999 | 0.2133 | 0.2341 | 0.2421 | 0.2558 | 0.2703 | |
| d-spacing (Å) | 36.55 | 35.64 | 32.93 | 31.43 | 29.46 | 26.84 | 25.95 | 24.56 | 23.24 | |

The assigned unit cell is a base-centered monoclinic with lattice constants of ***a*** = 20.02 nm, ***b, c*** = 13.21 nm, **α, γ** = 90°, and **β** = 131.60°. The **ϒ** and ***ucc*** values are 65.1% and 12.01 nm, respectively. Volume per one NC in the SL is 1307.27 nm$^3$.

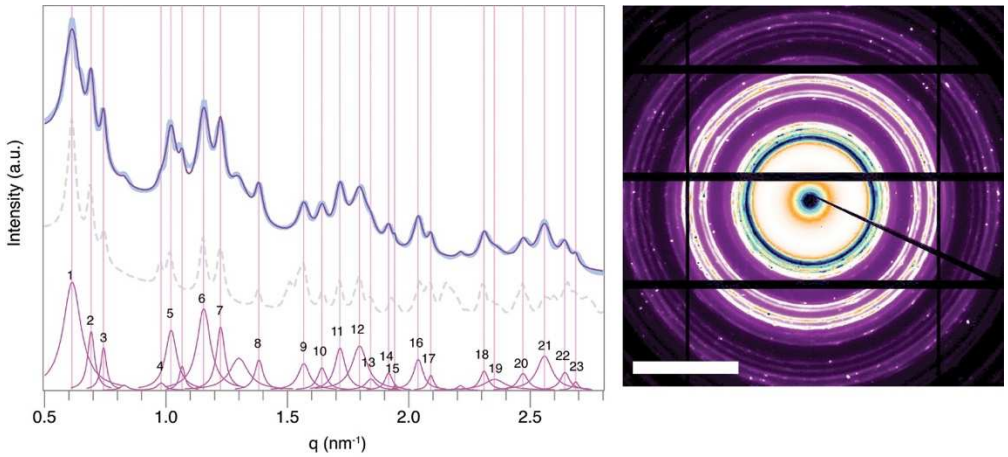


**Fig. S33. SAXS spectrum of SLs from Ag-NCs with λ of 0.83 with a particle volume of ca. 520 nm$^3$.** (left) SAXS spectrum of SLs from Ag-NCs with λ of 0.83 with a same individual particle volume as spherical and mecon Ag-NCs. The thick blue line, thin purple line, grey dashed line, and purple-red peaks represent the experimentally-obtained SAXS spectrum, the fitted spectrum, the simulated spectrum, and the constituent peaks used for fitting, respectively. (right) 2D SAXS pattern. The scale bar is 0.5 nm$^{-1}$.

**Table S21. Detailed results of the SAXS spectrum presented in Fig. S33.**

| Peak number | **1** | **2** | **3** | **4** | **5** | **6** | **7** | **8** | **9** | **10** |
|---|---|---|---|---|---|---|---|---|---|---|
| Peak position (q/Å) | 0.0614 | 0.0692 | 0.0743 | 0.0980 | 0.1021 | 0.1156 | 0.1225 | 0.1383 | 0.1568 | 0.1642 |
| d-spacing (Å) | 102.40 | 90.82 | 84.56 | 64.11 | 61.53 | 54.38 | 51.29 | 45.44 | 40.08 | 38.26 |
| Peak number | **11** | **12** | **13** | **14** | **15** | **16** | **17** | **18** | **19** | **20** |
| Peak position (q/Å) | 0.1717 | 0.1797 | 0.1843 | 0.1917 | 0.1942 | 0.2039 | 0.2091 | 0.2310 | 0.2353 | 0.2470 |
| d-spacing (Å) | 36.60 | 34.96 | 34.09 | 32.78 | 32.35 | 30.82 | 30.05 | 27.20 | 26.70 | 25.43 |
| Peak number | **21** | **22** | **23** | | | | | | | |
| Peak position (q/Å) | 0.2559 | 0.2643 | 0.2687 | | | | | | | |
| d-spacing (Å) | 24.56 | 23.78 | 23.38 | | | | | | | |

The assigned unit cell is a base-centered monoclinic with lattice constants of ***a*** = 21.25 nm, ***b, c*** = 12.85 nm, **α, γ** = 90°, and **β** = 127.42°. The **ζ** and ***ucc*** values are 22.1% and 12.43 nm, respectively. Volume per one NC in the SL is 1394.11 nm$^3$.

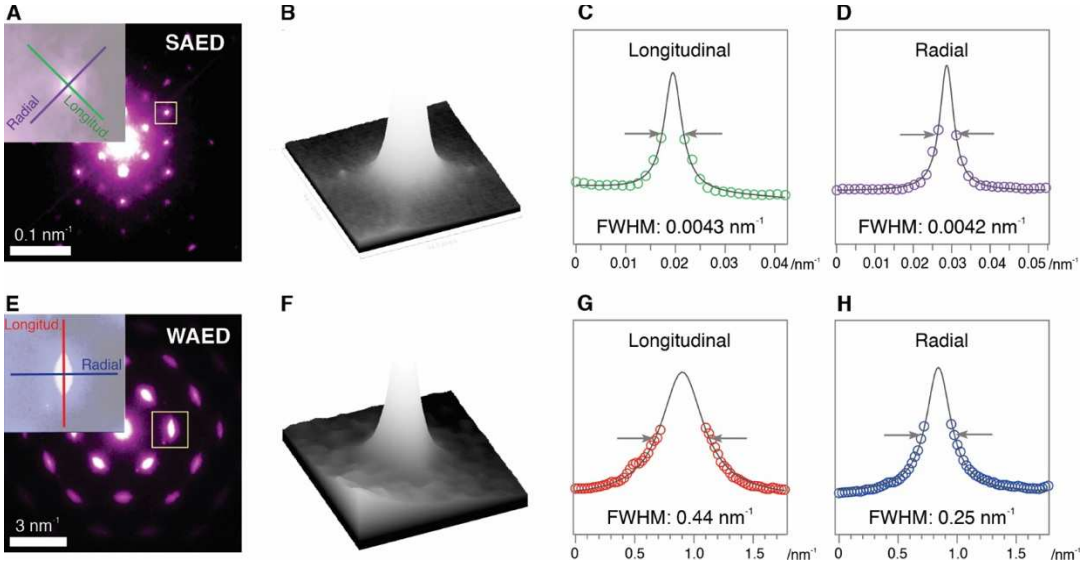


**Fig. S34. SAED and WAED peak elongation for assessing the rotational freedom of the NCs in N-W phase-intermediate SLs.** (**A-D**) SAED and (**E-H**), WAED patterns from the SLs with Ƭ of 22 % from Ag-NCs with λ of 0.83 (see panels xiii-xvi in Fig. S31). (**A, E**) ED patterns. The inset panels show a magnified signal with longitudinal and radial axes (i.e., major and minor diameters) of the oval pattern. (**B, F**) 3D contour maps of the selected ED signals. (**C, D, G, H**) Integrated intensity plots of ED patterns along the longitudinal (**C, G**) and radial (**D, H**) directions. Grey lines show the fitting results for each plot using the Gaussian curve, and the full-width half maximum (FWHM) values are presented below the peak. It is noted that plot points located at the center of the signal were omitted for the fitting purpose because of the saturated intensity signals. Graphs presented in Fig. 3G-K bottom represent the average L/R values (ratios of FWHM values along the longitudinal, L, and radial, R, directions) from multiple ED signals.

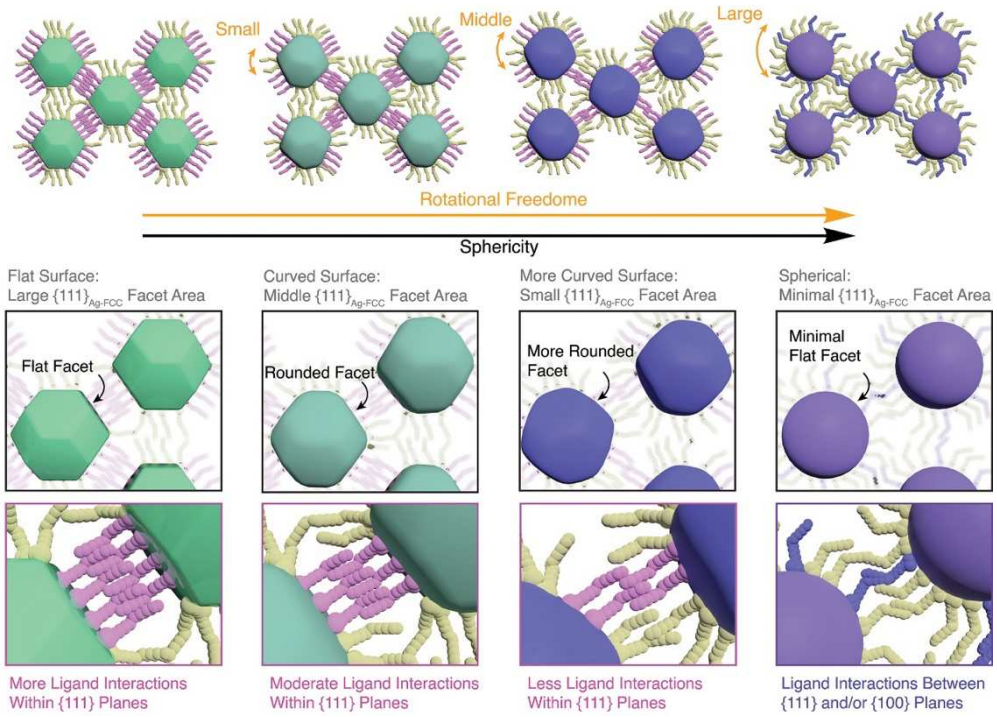


**Fig. S35. Computer models of FCC, phase-intermediate, and BCC SLs from Ag-NCs with different sphericities.** (top) The models illustrate that Ag-NCs within the SLs gain more rotational freedom as the sphericity of the building blocks increases. (middle) The models emphasize the Ag-NCs, showing that as curvature develops, the prominence of (111) facets diminishes. (bottom) The models depict ligand interactions between (111) facets of neighboring Ag-NCs. Ligands actively involved in these interactions are highlighted in purple in the image, and their involvement decreases as sphericity increases. In the spherical models, where the rotational symmetry is 6-fold, nearest-neighbor interactions extend beyond just (111) facets to include (111)-to-(100) and (100)-to-(100) facet interactions, represented by blue ligands in the model.

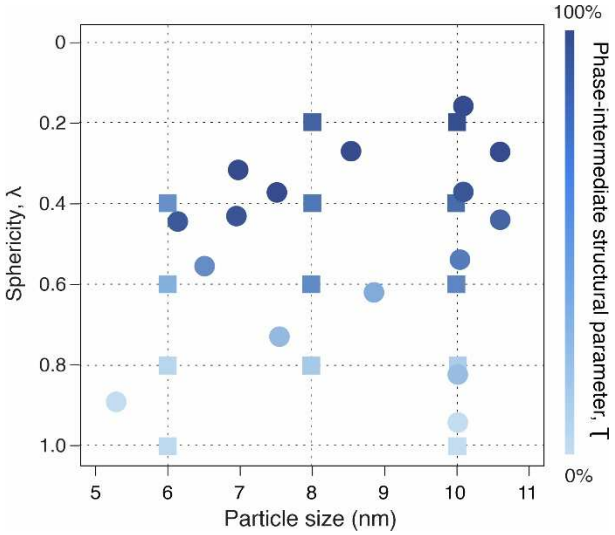


**Fig. S36. Plot of SL structure parameters as functions of sphericity and size of NC building blocks from experiments and MD simulation.** Sphere and square marks represent results from experiments and MD simulations, respectively.

Note: Across the entire studied size/shape range, the SL structures (i.e., FCC, BCC, or phase-intermediate) are primarily determined by particle sphericity, while particle size modulates the relative stability and accessibility of these structures, confirming the accessibility of the phase-intermediate regime and good agreement between experimental and simulation results.

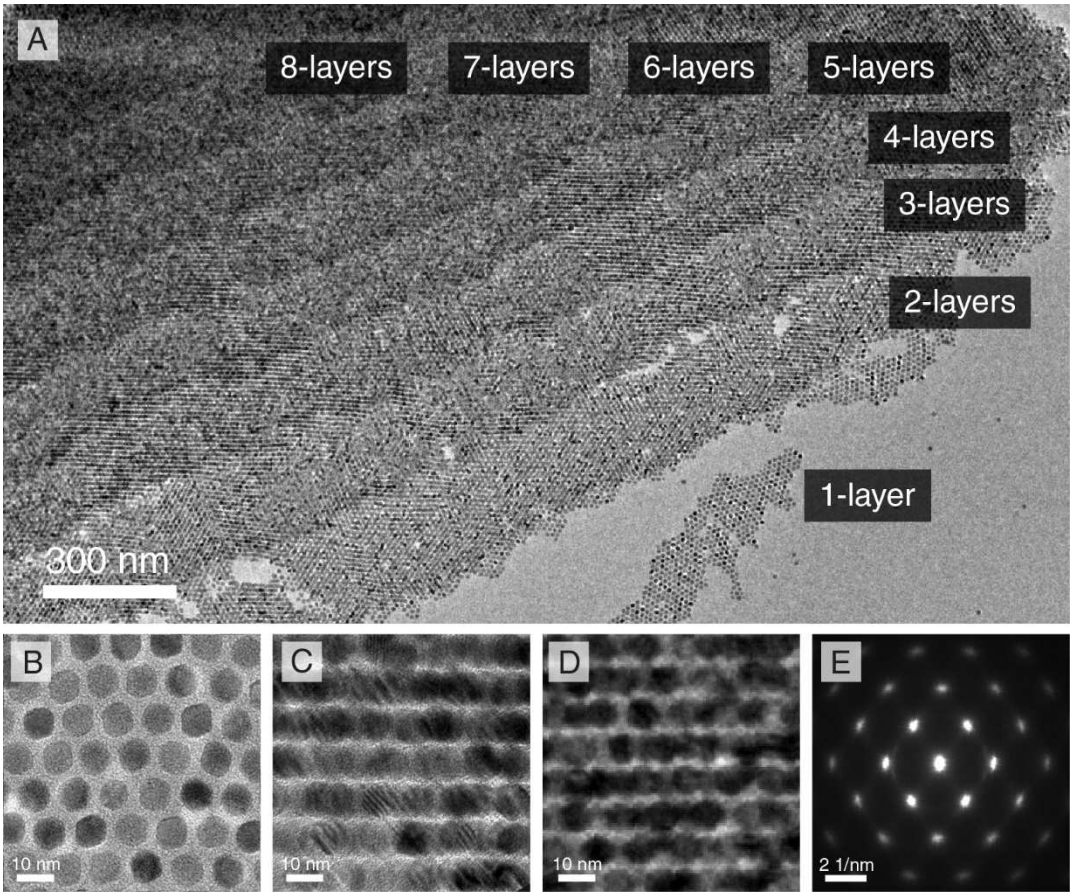


**Fig. S37. TEM analysis of BCC SLs containing various layers presented in Fig. 4B in the main text**. (**A**) A large TEM image presented in Fig. 4B. (**B-D**) Magnified TEM images of 1-layer SLs (**B**), 2-layers SLs (**C**), and 3-layers SLs (**D**). (**E**) WAED pattern from the 3 layers SLs. It is noted that the SLs thicker than 1-layer SLs consistently show similar type of WAED patterns. The assigned structure is consistent with the structural model presented in Fig. 1L and Fig. S5.

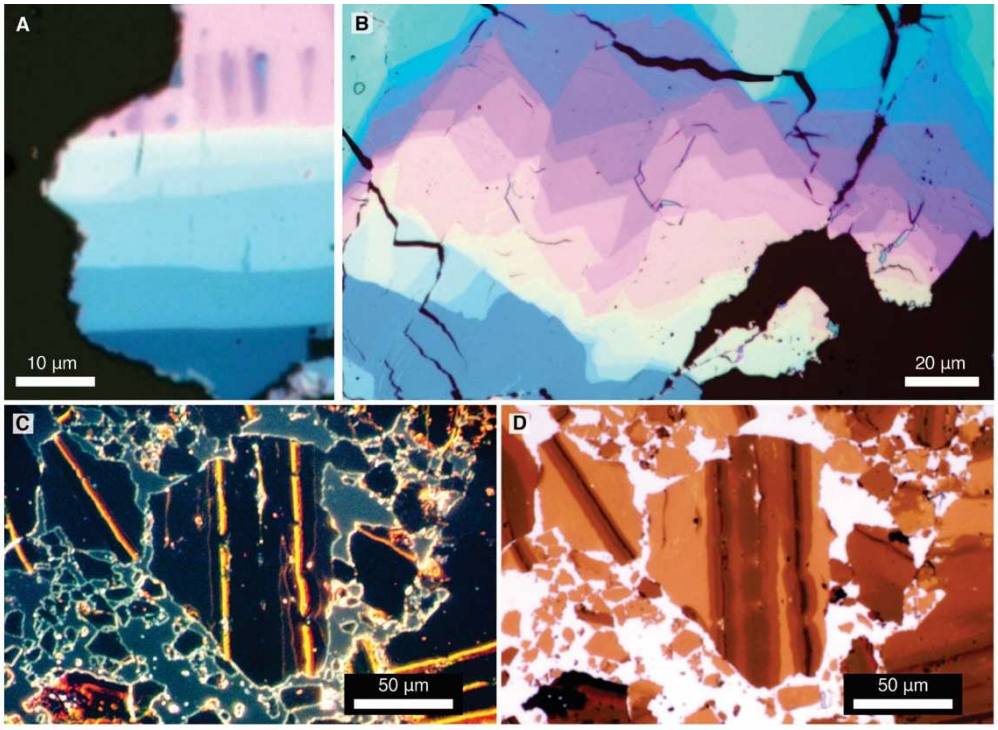


**Fig. S38. Images of Ag-NC SLs under optical microscopes.** (**A, B**) Images in reflection mode, (**C**) dark field mode, and (**D**) transmission mode.

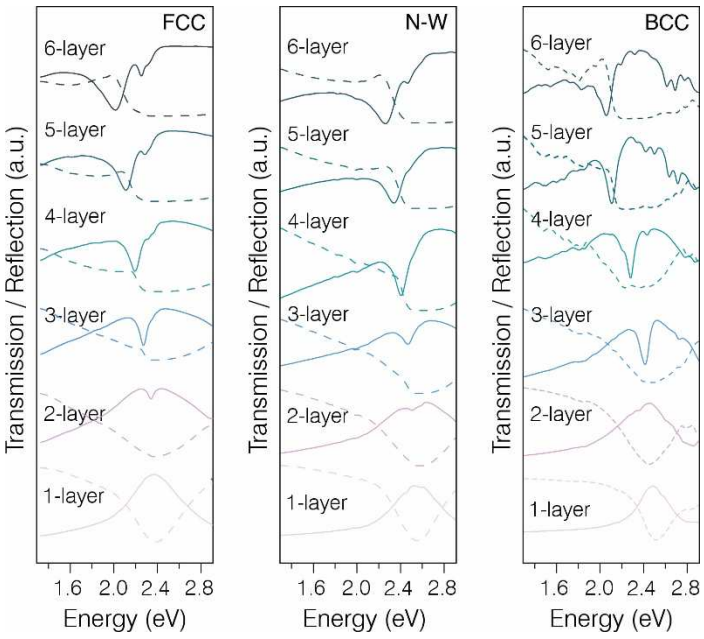


**Fig. S39. Simulated optical properties of Ag-NC SLs consisting of 1-6 layers.** (left) FCC SLs from spherical Ag-NCs, (center) N-W phase-intermediate SLs from Ag-NCs with λ of 0.56, and (right) BCC SLs from mecon Ag-NCs. Dashed and solid lines are transmission and reflection spectra, respectively. Note that the N-W phase-intermediate SL model employed in the electromagnetic simulations is a simplified model. Details are provided in *Finite-Difference Time-Domain (FDTD) simulations for plasmonics of Ag-NC SLs* in Methods

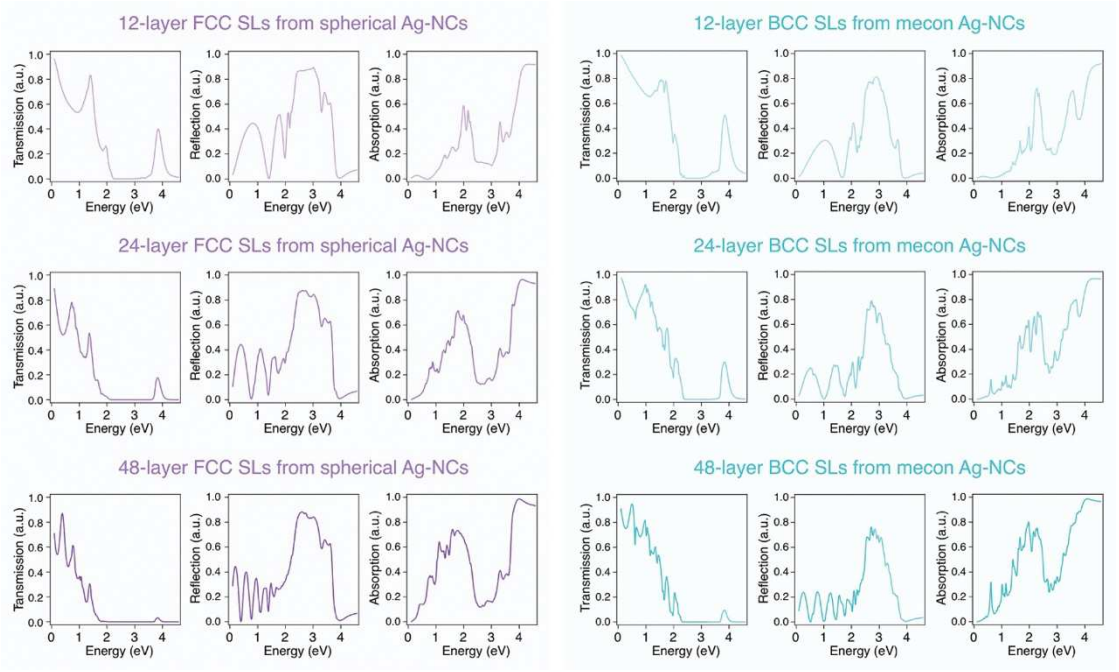


**Fig. S40. FDTD simulated optical properties of FCC and BCC Ag-NC SLs.** Simulated optical properties (transmission, reflection, and absorption) of FCC SLs from spherical Ag-NCs (left, purple lines) and BCC SLs from mecon Ag-NCs (right, blue lines) consisting of 12 layers (top), 24 layers (middle), and 48 layers (bottom).

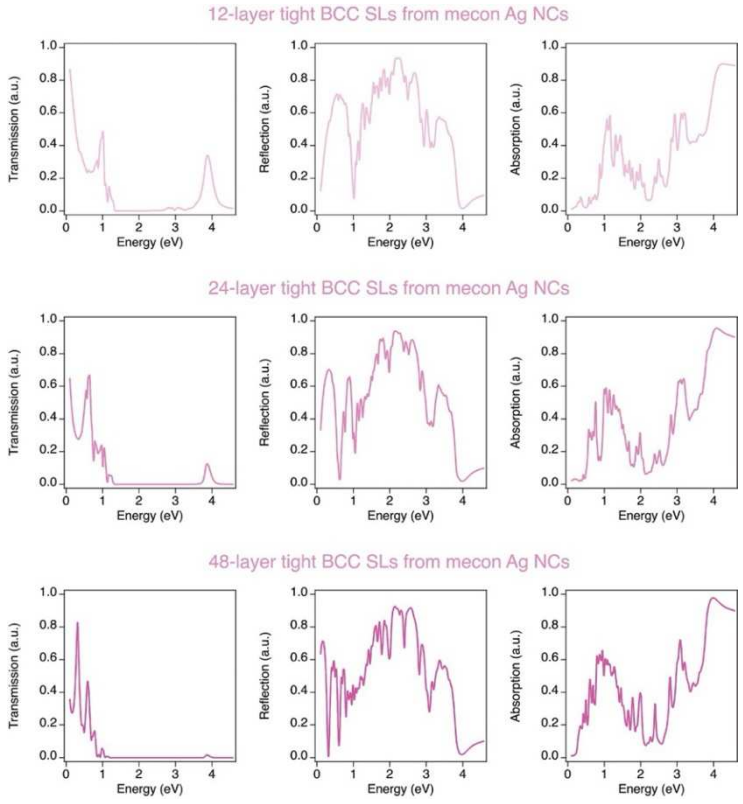


**Fig. S41. FDTD simulated optical properties of tight BCC SLs from mecon Ag-NCs with various layer numbers.** Calculated transmission (left), reflection (center), and absorption (right) spectra of BCC SLs from mecon Ag-NCs with a smaller gap distance (i.e., 0.5 nm) consisting of 12 layers (top), 24 layers (middle), and 48 layers (bottom).

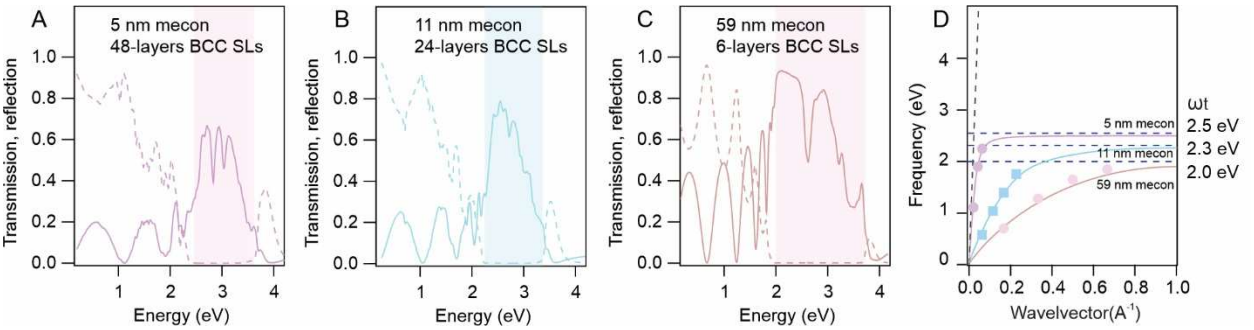


**Fig. S42. Plasmonic properties simulation for BCC SLs from different size Ag-NCs.** Simulated optical properties (transmission for dashed line and reflection for solid lines) of 48-layers BCC SLs from 5 nm mecon Ag-NCs (**A**), 24-layers BCC SLs from 11.25 nm mecon Ag-NCs (**B**), and 6-layers BCC SLs from 59 nm mecon Ag-NCs (**C**). (**D**) Dispersion of the lower plasmon-polaritons for BCC SLs. 5 nm mecon Ag-NCs (purple circle marks), 11.25 nm mecon Ag-NCs (blue square marks), and 59 nm mecon Ag-NCs (pink circle marks). The solid lines, dotted lines, and dash lines are the fitting lines with a Hopfield Hamiltonian, fitted transverse collective plasmon frequency, $\omega_t$, and free photon dispersion, respectively.

**Table S22. Results of electromagnetic simulation for light-matter coupling in various SLs**

| Materials | SL Structure | Gap Distance* | Size | Shape | Packing Fraction | $\Omega_R$ (eV) | $\omega_t$ (eV) | η |
|---|---|---|---|---|---|---|---|---|
| Ag | BCC | 1.30 nm | 5 nm | Mecon | 25.0% | 1.72 | 2.50 | 0.69 |
| Au | FCC | 1.30 nm | 11.25 nm | Sphere | 53.3% | 1.87 | 1.85 | 1.01 |
| Ag | FCC | 1.30 nm | 11.25 nm | Sphere | 53.3% | 2.25 | 2.16 | 1.04 |
| Ag | phase-intermediate** | 1.30 nm | 11.25 nm | IS*** | 55.0% | 2.49 | 2.37 | 1.05 |
| Ag | BCC | 1.30 nm | 11.25 nm | Mecon | 57.2% | 2.43 | 2.30 | 1.06 |
| Ag | BCC tight | 0.50 nm | 11.25 nm | Mecon | 84.5% | 2.77 | 1.54 | 1.80 |
| Au | FCC | 1.30 nm | 59 nm | Sphere | 70.4% | 1.74 | 1.32 | 1.32 |
| Ag | FCC | 1.30 nm | 59 nm | Sphere | 70.4% | 1.91 | 1.40 | 1.36 |
| Ag | BCC | 1.30 nm | 59 nm | Mecon | 95.1% | 5.13 | 1.98 | 2.60 |

* Gap distance. Details are provided in Supplementary Text 1: *Geometrical characteristics of mecons, spheres, and their SLs*

** The phase-intermediate SL model employed in the electromagnetic simulations is a simplified model. Details are provided in *Finite-Difference Time-Domain (FDTD) simulations for plasmonics of Ag-NC SLs* in Methods

*** IS: Intermediate shape, i.e., Ag-NCs with a sphericity parameter λ = 0.56.

## III. Video Captions

**Caption for Movie S1**
**SAXS pattern evolution during the Nishiyama-Wassermann transformation pathway.**

**Caption for Movie S2**
**MC simulation trajectory for λ = 0.4 with the stiff interaction model starting from a BCC lattice.** The particle centers were initialized on a BCC lattice. The video shows $4 \times 10^7$ HPMC steps. The system packing fraction increased from 52% to 70% during the first $2.5 \times 10^7$ HPMC steps, after which it was held constant at 70%. The shape of the simulation box (i.e., its aspect ratio and tilt factors) was allowed to fluctuate during the entire simulation to allow anisotropic stresses to relax.

**Caption for Movie S3**
**MC simulation trajectory for λ = 0.4 with the stiff interaction model. starting from an FCC lattice.** The particle centers were initialized on an FCC lattice. The video shows $4 \times 10^7$ HPMC steps. The system packing fraction increased from 52% to 70% during the first $2.5 \times 10^7$ HPMC steps, after which it was held constant at 70%. The shape of the simulation box (i.e., its aspect ratio and tilt factors) was allowed to fluctuate during the entire simulation to allow anisotropic stresses to relax.

**Caption for Movie S4**
**MC simulation trajectory for λ = 0.6 with the stiff interaction model starting from a BCC lattice.** The particle centers were initialized on a BCC lattice. The video shows $1.5 \times 10^8$ HPMC steps. The system packing fraction increased from 52% to 70% during the first $2.5 \times 10^7$ HPMC steps, after which it was held constant at 70%. The shape of the simulation box (i.e., its aspect ratio and tilt factors) was allowed to fluctuate during the entire simulation to allow anisotropic stresses to relax.

**Caption for Movie S5**
**MC simulation trajectory for λ = 0.6 with the stiff interaction model starting from an FCC lattice.** The particle centers were initialized on an FCC lattice. The video shows $1.5 \times 10^8$ HPMC steps. The system packing fraction increased from 52% to 70% during the first $2.5 \times 10^7$ HPMC steps, after which it was held constant at 70%. The shape of the simulation box (i.e., its aspect ratio and tilt factors) was allowed to fluctuate during the entire simulation to allow anisotropic stresses to relax.

**Caption for Movie S6**
**MD simulation trajectory for λ = 0.0 with the total (soft + stiff) interaction model.** The video shows $2 \times 10^7$ MD steps, and the systems' pressure setpoint increased from 0.01 to 0.1 during the first $1 \times 10^7$ steps, after which it remained constant at 0.1.

**Caption for Movie S7**
**MD simulation trajectory for λ = 0.6 with the total (soft + stiff) interaction model.** The video shows $2 \times 10^7$ MD steps, and the systems' pressure setpoint increased from 0.01 to 0.1 during the first $1 \times 10^7$ steps, after which it remained constant at 0.1.

**Caption for Movie S8**
**MD simulation trajectory for λ = 1.0 with the total (soft + stiff) interaction model.** The video shows $2 \times 10^7$ MD steps, and the systems' pressure setpoint increased from 0.01 to 0.1 during the first $1 \times 10^7$ steps, after which it remained constant at 0.1.

**References and Notes**


1. G. M. Whitesides, B. Grzybowski, Self-assembly at all scales. *Science* **295**, 2418–2421 (2002). doi:10.1126/science.1070821 Medline

2. D. Kondepudi, I. Prigogine, *Modern Thermodynamics: From Heat Engines to Dissipative Structures* (Wiley, ed. 2, 2014).

3. M. A. Boles, M. Engel, D. V. Talapin, Self-assembly of colloidal nanocrystals: From intricate structures to functional materials. *Chem. Rev.* **116**, 11220–11289 (2016). doi:10.1021/acs.chemrev.6b00196 Medline

4. S. Lee, T. Vo, S. C. Glotzer, Entropy compartmentalization stabilizes open host-guest colloidal clathrates. *Nat. Chem.* **15**, 905–912 (2023). doi:10.1038/s41557-023-01200-6 Medline

5. B. A. Grzybowski, W. T. Huck, The nanotechnology of life-inspired systems. *Nat. Nanotechnol.* **11**, 585–592 (2016). doi:10.1038/nnano.2016.116 Medline

6. Y. Nagaoka, J. Schneider, H. Zhu, O. Chen, Quasicrystalline materials from non-atom building blocks. *Matter* **6**, 30–58 (2023). doi:10.1016/j.matt.2022.09.027

7. C. L. Bassani, G. van Anders, U. Banin, D. Baranov, Q. Chen, M. Dijkstra, M. S. Dimitriyev, E. Efrati, J. Faraudo, O. Gang, N. Gaston, R. Golestanian, G. I. Guerrero-Garcia, M. Gruenwald, A. Haji-Akbari, M. Ibáñez, M. Karg, T. Kraus, B. Lee, R. C. Van Lehn, R. J. Macfarlane, B. M. Mognetti, A. Nikoubashman, S. Osat, O. V. Prezhdo, G. M. Rotskoff, L. Saiz, A.-C. Shi, S. Skrabalak, I. I. Smalyukh, M. Tagliazucchi, D. V. Talapin, A. V. Tkachenko, S. Tretiak, D. Vaknin, A. Widmer-Cooper, G. C. L. Wong, X. Ye, S. Zhou, E. Rabani, M. Engel, A. Travesset, Nanocrystal Assemblies: Current Advances and Open Problems. *ACS Nano* **18**, 14791–14840 (2024). doi:10.1021/acsnano.3c10201 Medline

8. T. Xiao, Y. Nagaoka, X. Wang, T. Jiang, D. LaMontagne, Q. Zhang, C. Cao, X. Diao, J. Qiu, Y. Lu, Z. Wang, Y. C. Cao, Nanocrystals with metastable high-pressure phases under ambient conditions. *Science* **377**, 870–874 (2022). doi:10.1126/science.abq7684 Medline

9. M. C. Weidman, D. M. Smilgies, W. A. Tisdale, Kinetics of the self-assembly of nanocrystal superlattices measured by real-time *in situ* X-ray scattering. *Nat. Mater.* **15**, 775–781 (2016). doi:10.1038/nmat4600 Medline

10. D. W. Yee, M. S. Lee, J. An, R. J. Macfarlane, Reversible diffusionless phase transitions in 3D nanoparticle superlattices. *J. Am. Chem. Soc.* **145**, 6051–6056 (2023). doi:10.1021/jacs.3c01286 Medline

11. D. A. Porter, K. E. Easterling, M. Y. Sherif, *Phase Transformations in Metals and Alloys* (CRC Press, ed. 3, 2009).

12. J. L. Greenfield, J. Wade, J. R. Brandt, X. Shi, T. J. Penfold, M. J. Fuchter, Pathways to increase the dissymmetry in the interaction of chiral light and chiral molecules. *Chem. Sci.* **12**, 8589–8602 (2021). doi:10.1039/D1SC02335G Medline

13. S. Y. Schmid, K. Lachowski, H. T. Chiang, L. Pozzo, J. De Yoreo, S. Zhang, Mechanisms of biomolecular self-assembly investigated through *in situ* observations of structures and

dynamics. *Angew. Chem. Int. Ed.* **62**, e202309725 (2023). doi:10.1002/anie.202309725 Medline

14. A. Parija, G. R. Waetzig, J. L. Andrews, S. Banerjee, Traversing energy landscapes away from equilibrium: Strategies for accessing and utilizing metastable phase space. *J. Phys. Chem. C* **122**, 25709–25728 (2018). doi:10.1021/acs.jpcc.8b04622

15. Q. Yun, Y. Ge, Z. Shi, J. Liu, X. Wang, A. Zhang, B. Huang, Y. Yao, Q. Luo, L. Zhai, J. Ge, Y. Peng, C. Gong, M. Zhao, Y. Qin, C. Ma, G. Wang, Q. Wa, X. Zhou, Z. Li, S. Li, W. Zhai, H. Yang, Y. Ren, Y. Wang, L. Li, X. Ruan, Y. Wu, B. Chen, Q. Lu, Z. Lai, Q. He, X. Huang, Y. Chen, H. Zhang, Recent progress on phase engineering of nanomaterials. *Chem. Rev.* **123**, 13489–13692 (2023). doi:10.1021/acs.chemrev.3c00459 Medline

16. Y. Han, L. Wang, K. Cao, J. Zhou, Y. Zhu, Y. Hou, Y. Lu, In situ TEM characterization and modulation for phase engineering of nanomaterials. *Chem. Rev.* **123**, 14119–14184 (2023). doi:10.1021/acs.chemrev.3c00510 Medline

17. Y. Zhang, S. Pal, B. Srinivasan, T. Vo, S. Kumar, O. Gang, Selective transformations between nanoparticle superlattices via the reprogramming of DNA-mediated interactions. *Nat. Mater.* **14**, 840–847 (2015). doi:10.1038/nmat4296 Medline

18. C. B. Williamson, D. R. Nevers, A. Nelson, I. Hadar, U. Banin, T. Hanrath, R. D. Robinson, Chemically reversible isomerization of inorganic clusters. *Science* **363**, 731–735 (2019). doi:10.1126/science.aau9464 Medline

19. Z. Cheng, M. R. Jones, Assembly of planar chiral superlattices from achiral building blocks. *Nat. Commun.* **13**, 4207 (2022). doi:10.1038/s41467-022-31868-2 Medline

20. P. Kumar, T. Vo, M. Cha, A. Visheratina, J. Y. Kim, W. Xu, J. Schwartz, A. Simon, D. Katz, V. P. Nicu, E. Marino, W. J. Choi, M. Veksler, S. Chen, C. Murray, R. Hovden, S. Glotzer, N. A. Kotov, Photonically active bowtie nanoassemblies with chirality continuum. *Nature* **615**, 418–424 (2023). doi:10.1038/s41586-023-05733-1 Medline

21. M. Yankowitz, S. Chen, H. Polshyn, Y. Zhang, K. Watanabe, T. Taniguchi, D. Graf, A. F. Young, C. R. Dean, Tuning superconductivity in twisted bilayer graphene. *Science* **363**, 1059–1064 (2019). doi:10.1126/science.aav1910 Medline

22. S. Wan, X. Xia, Y. Gao, H. Zhang, Z. Zhang, F. Wu, X. Wu, D. Yang, T. Li, J. Li, R. Ni, A. Dong, Curvature-guided depletion stabilizes Kagome superlattices of nanocrystals. *Science* **387**, 978–984 (2025). doi:10.1126/science.adu4125 Medline

23. A. F. Kockum, A. Miranowicz, S. De Liberato, S. Savasta, F. Nori, Ultrastrong coupling between light and matter. *Nat. Rev. Phys.* **1**, 19–40 (2019). doi:10.1038/s42254-018-0006-2

24. Y. Nagaoka, R. Tan, R. Li, H. Zhu, D. Eggert, Y. A. Wu, Y. Liu, Z. Wang, O. Chen, Superstructures generated from truncated tetrahedral quantum dots. *Nature* **561**, 378–382 (2018). doi:10.1038/s41586-018-0512-5 Medline

25. Y. Nagaoka, H. Zhu, D. Eggert, O. Chen, Single-component quasicrystalline nanocrystal superlattices through flexible polygon tiling rule. *Science* **362**, 1396–1400 (2018). doi:10.1126/science.aav0790 Medline

26. J. Henzie, M. Grünwald, A. Widmer-Cooper, P. L. Geissler, P. Yang, Self-assembly of uniform polyhedral silver nanocrystals into densest packings and exotic superlattices. *Nat. Mater.* **11**, 131–137 (2011). doi:10.1038/nmat3178 Medline

27. Z. Nishiyama, *Martensitic Transformation* (Academic Press, 1978).

28. H. Sowa, Sphere packings as a tool for the description of martensitic phase transformations. *Acta Crystallogr. A Found. Adv.* **73**, 39–45 (2017). doi:10.1107/S2053273316013425 Medline

29. L. H. Zhang, M. J. Cheng, X. H. Shi, J. W. Shuai, Z. Z. Zhu, Bain and Nishiyama–Wassermann transition path separation in the martensitic transitions of Fe. *RSC Adv.* **11**, 3043–3048 (2021). doi:10.1039/D0RA09332G Medline

30. H. Y. Chao, K. Venkatraman, S. Moniri, Y. Jiang, X. Tang, S. Dai, W. Gao, J. Miao, M. Chi, *In situ* and emerging transmission electron microscopy for catalysis research. *Chem. Rev.* **123**, 8347–8394 (2023). doi:10.1021/acs.chemrev.2c00880 Medline

31. G. Rainò, H. Utzat, M. G. Bawendi, M. V. Kovalenko, Superradiant emission from self-assembled light emitters: From molecules to quantum dots. *MRS Bull.* **45**, 841–849 (2020). doi:10.1557/mrs.2020.250

32. K. Bian, H. Schunk, D. Ye, A. Hwang, T. S. Luk, R. Li, Z. Wang, H. Fan, Formation of self-assembled gold nanoparticle supercrystals with facet-dependent surface plasmonic coupling. *Nat. Commun.* **9**, 2365 (2018). doi:10.1038/s41467-018-04801-9 Medline

33. N. S. Mueller, Y. Okamura, B. G. M. Vieira, S. Juergensen, H. Lange, E. B. Barros, F. Schulz, S. Reich, Deep strong light-matter coupling in plasmonic nanoparticle crystals. *Nature* **583**, 780–784 (2020). doi:10.1038/s41586-020-2508-1 Medline

34. M. Cargnello, A. C. Johnston-Peck, B. T. Diroll, E. Wong, B. Datta, D. Damodhar, V. V. T. Doan-Nguyen, A. A. Herzing, C. R. Kagan, C. B. Murray, Substitutional doping in nanocrystal superlattices. *Nature* **524**, 450–453 (2015). doi:10.1038/nature14872 Medline

35. W. Zhou, Y. Li, K. Je, T. Vo, H. Lin, B. E. Partridge, Z. Huang, S. C. Glotzer, C. A. Mirkin, Space-tiled colloidal crystals from DNA-forced shape-complementary polyhedra pairing. *Science* **383**, 312–319 (2024). doi:10.1126/science.adj1021 Medline

36. H. Pan, J. Dshemuchadse, Kinetic pathways of solid-solid phase transitions dictated by short-range interactions. *Proc. Natl. Acad. Sci. U.S.A.* **122**, e2507403122 (2025). doi:10.1073/pnas.2507403122 Medline

37. R. B. Fuller, E. J. Applewhite, A. L. Loeb, *Synergetics: Explorations in the Geometry of Thinking* (Macmillan, 1975).

38. B. J. Wiley, S. H. Im, Z. Y. Li, J. McLellan, A. Siekkinen, Y. Xia, Maneuvering the surface plasmon resonance of silver nanostructures through shape-controlled synthesis. *J. Phys. Chem. B* **110**, 15666–15675 (2006). doi:10.1021/jp0608628 Medline

39. S. Peng, J. M. McMahon, G. C. Schatz, S. K. Gray, Y. Sun, Reversing the size-dependence of surface plasmon resonances. *Proc. Natl. Acad. Sci. U.S.A.* **107**, 14530–14534 (2010). doi:10.1073/pnas.1007524107 Medline

40. Y. Nagaoka, J. Schneider, N. Jin, T. Cai, Y. Liu, Z. Wang, R. Li, K. S. Kim, O. Chen, Dynamic transformation of high-architectural nanocrystal superlattices upon solvent molecule exposure. *J. Am. Chem. Soc.* **146**, 13093–13104 (2024). doi:10.1021/jacs.3c14603 Medline

41. Z. Quan, J. Y. Fang, Superlattices with non-spherical building blocks. *Nano Today* **5**, 390–411 (2010). doi:10.1016/j.nantod.2010.08.011

42. J. Gong, R. S. Newman, M. Engel, M. Zhao, F. Bian, S. C. Glotzer, Z. Tang, Shape-dependent ordering of gold nanocrystals into large-scale superlattices. *Nat. Commun.* **8**, 14038 (2017). doi:10.1038/ncomms14038 Medline

43. C. X. Du, G. van Anders, R. S. Newman, S. C. Glotzer, Shape-driven solid-solid transitions in colloids. *Proc. Natl. Acad. Sci. U.S.A.* **114**, E3892–E3899 (2017). doi:10.1073/pnas.1621348114 Medline

44. G. van Anders, N. K. Ahmed, R. Smith, M. Engel, S. C. Glotzer, Entropically patchy particles: Engineering valence through shape entropy. *ACS Nano* **8**, 931–940 (2014). doi:10.1021/nn4057353 Medline

45. M. Herran, S. Juergensen, M. Kessens, D. Hoeing, A. Köppen, A. Sousa-Castillo, W. J. Parak, H. Lange, S. Reich, F. Schulz, E. Cortés, Plasmonic bimetallic two-dimensional supercrystals for $H_2$ generation. *Nat. Catal.* **6**, 1205–1214 (2023). doi:10.1038/s41929-023-01053-9

46. Z. Zhu, H. Meng, W. Liu, X. Liu, J. Gong, X. Qiu, L. Jiang, D. Wang, Z. Tang, Superstructures and SERS properties of gold nanocrystals with different shapes. *Angew. Chem. Int. Ed.* **50**, 1593–1596 (2011). doi:10.1002/anie.201005493 Medline

47. E. B. Barros, B. G. Vieira, N. S. Mueller, S. Reich, Plasmon polaritons in nanoparticle supercrystals: Microscopic quantum theory beyond the dipole approximation. *Phys. Rev. B* **104**, 035403 (2021). doi:10.1103/PhysRevB.104.035403

48. T. Paul, A. M. Green, D. J. Milliron, T. M. Truskett, Plasmon polaritons in disordered nanoparticle assemblies. *ACS Photonics* **12**, 5682–5696 (2025). doi:10.1021/acsphotonics.5c01447

49. S. De Liberato, Virtual photons in the ground state of a dissipative system. *Nat. Commun.* **8**, 1465 (2017). doi:10.1038/s41467-017-01504-5 Medline

50. F. Schulz, O. Pavelka, F. Lehmkühler, F. Westermeier, Y. Okamura, N. S. Mueller, S. Reich, H. Lange, Structural order in plasmonic superlattices. *Nat. Commun.* **11**, 3821 (2020). doi:10.1038/s41467-020-17632-4 Medline

51. K. Bhattacharya, S. Conti, G. Zanzotto, J. Zimmer, Crystal symmetry and the reversibility of martensitic transformations. *Nature* **428**, 55–59 (2004). doi:10.1038/nature02378 Medline

52. S. Förster, A. Timmann, M. Konrad, C. Schellbach, A. Meyer, S. S. Funari, P. Mulvaney, R. Knott, Scattering curves of ordered mesoscopic materials. *J. Phys. Chem. B* **109**, 1347–1360 (2005). doi:10.1021/jp0467494 Medline

53. S. Förster, A. Timmann, C. Schellbach, A. Frömsdorf, A. Kornowski, H. Weller, S. V. Roth, P. Lindner, Order causes secondary Bragg peaks in soft materials. *Nat. Mater.* **6**, 888–893 (2007). doi:10.1038/nmat1995 Medline

54. B. D. Cullity, S. R. Stock, *Elements of X-Ray Diffraction* (Pearson, ed. 3, 2014).

55. B. T. Draine, The discrete-dipole approximation and its application to interstellar graphite grains. *Astrophys. J.* **333**, 848–872 (1988). doi:10.1086/166795

56. P. B. Johnson, R. W. Christy, Optical constants of noble metals. *Phys. Rev. B* **6**, 4370–4379 (1972). doi:10.1103/PhysRevB.6.4370

57. J. A. Anderson, J. Glaser, S. C. Glotzer, HOOMD-blue: A Python package for high-performance molecular dynamics and hard particle Monte Carlo simulations. *Comput. Mater. Sci.* **173**, 109363 (2020). doi:10.1016/j.commatsci.2019.109363

58. J. A. Anderson, M. E. Irrgang, S. C. Glotzer, Scalable metropolis Monte Carlo for simulation of hard shapes. *Comput. Phys. Commun.* **204**, 21–30 (2016). doi:10.1016/j.cpc.2016.02.024

59. V. Ramasubramani, B. D. Dice, E. S. Harper, M. P. Spellings, J. A. Anderson, S. C. Glotzer, freud: A software suite for high throughput analysis of particle simulation data. *Comput. Phys. Commun.* **254**, 107275 (2020). doi:10.1016/j.cpc.2020.107275

60. S. J. Khan, F. Pierce, C. M. Sorensen, A. Chakrabarti, Self-assembly of ligated gold nanoparticles: Phenomenological modeling and computer simulations. *Langmuir* **25**, 13861–13868 (2009). doi:10.1021/la9008202 Medline

61. T. Kister, D. Monego, P. Mulvaney, A. Widmer-Cooper, T. Kraus, Colloidal stability of apolar nanoparticles: The role of particle size and ligand shell structure. *ACS Nano* **12**, 5969–5977 (2018). doi:10.1021/acsnano.8b02202 Medline

62. T. D. Nguyen, C. L. Phillips, J. A. Anderson, S. C. Glotzer, Rigid body constraints realized in massively-parallel molecular dynamics on graphics processing units. *Comput. Phys. Commun.* **182**, 2307–2313 (2011). doi:10.1016/j.cpc.2011.06.005

63. G. J. Martyna, D. J. Tobias, M. L. Klein, Constant-pressure molecular-dynamics algorithms. *J. Chem. Phys.* **101**, 4177–4189 (1994). doi:10.1063/1.467468

64. P. J. Steinhardt, S. Ostlund, *The Physics of Quasicrystals* (World Scientific, 1987).

65. A. Taflove, S. C. Hagness, *Computational Electrodynamics: The Finite-Difference Time-Domain Method* (Artech House, ed. 3, 2005).

66. H. U. Yang, J. D'Archangel, M. L. Sundheimer, E. Tucker, G. D. Boreman, M. B. Raschke, Optical dielectric function of silver. *Phys. Rev. B* **91**, 235137 (2015). doi:10.1103/PhysRevB.91.235137